DESIGN, FABRICATION AND CHARACTERIZATION OF SUB-THZ COMPONENTS IN GLASS INTERPOSER SUBSTRATES

A Dissertation
Presented to
The Academic Faculty

by

Mutee ur Rehman

In Partial Fulfillment
of the Requirements for the Degree of
Doctor of Philosophy in the School of Electrical and Computer Engineering

Georgia Institute of Technology
May 2023

DESIGN, FABRICATION AND CHARACTERIZATION OF SUB-THZ COMPONENTS IN GLASS INTERPOSER SUBSTRATES

Approved by:

Dr. Madhavan Swaminathan, Advisor
School of Electrical and Computer Engineering
Georgia Institute of Technology

Dr. Andrew F. Peterson
School of Electrical and Computer Engineering
Georgia Institute of Technology

Dr. Nima Ghalichechian
School of Electrical and Computer Engineering
Georgia Institute of Technology

Dr. Gregory David Durgin
School of Electrical and Computer Engineering
Georgia Institute of Technology

Dr. Suresh K. Sitaraman
School of Mechanical Engineering
Georgia Institute of Technology

Date Approved: March 14, 2023

To my beloved wife, Maida, and parents, Nighat and Waseem for their constant love and support.

ACKNOWLEDGEMENTS

It is an undisputed fact that path towards earning a PhD is challenging and requires a lot of determination, resilience, and perseverance. I consider myself quite fortunate that during my doctoral studies, I came across many remarkable individuals which made my journey easy, memorable, and joyful. I am deeply indebted to all of them for their support, advice, and helpful contributions.

First, I would like to thank my advisor Prof. Madhavan Swaminathan for believing in me and giving me an opportunity to purse PhD in his research group at Georgia Tech. All along my PhD, he mentored me by sharing his invaluable experience, helpful technical knowledge, and useful practical suggestions. He gave me the freedom to work independently which really helped me evolve as a researcher. I still remember my first meeting with him when he explained me the need to explore the frequency region above 100 GHz and as a new first year PhD student, I was just wondering how I will be able to work in such challenging area, but Prof. Swaminathan equipped me with all the necessary guidance and facilities and due to his unparalleled support, I was complete all the work related to this thesis. I hope that I could be as dedicated in my professional life as Prof. Swaminathan is and one day, I will be able to make fantastic technical presentations as he does. I would like to thank him again and I will always be grateful to him for giving me once-in-a-lifetime opportunity to study at Georgia Tech.

I would like to express my special appreciation to Prof. Andrew F. Peterson, Prof. Gregory Durgin, Prof. Nima Ghalichechian and Prof. Sureh K. Sitaraman for taking out time to

serve on my PhD dissertation committee and give useful suggestions to improve the quality of this research.

I would like to say thanks the sponsors of my research for funding this project. This work was supported in part by ASCENT, one of the six centers in JUMP, a Semiconductor Research Corporation (SRC) program sponsored by DARPA and in part by the Georgia Tech Packaging Research Center (PRC).

I am grateful to Dr. Fuhan Liu for teaching me the basics of process development. During my PhD, we had numerous in person and online meetings to discuss the results and next steps for fabrication, and he always gave helpful suggestions. I hope the incoming students will continue to benefit from his expertise and knowledge. I wish him all the best in life.

I would like to thank Dr. Ali Hassan and Dr. Usman Younis for mentoring and guiding me during my undergraduate program at National University of Sciences and Technology (NUST). I am extremely grateful to Dr. Wasif Tanveer Khan for giving me an opportunity to work under his supervision at EM Lab in Lahore University of Management Sciences (LUMS). Dr. Wasif Tanveer introduced me to the interesting areas of research in RF and microwave engineering and he equipped me with necessary design and fabrication tools to do independent research which piqued my interest to go further and pursue a PhD degree.

I would like to acknowledge the efforts of our research staff for managing all the tools, dealing with all the vendors and maintaining the supply chain which kept me on track to complete my work in the cleanroom. Many thanks to Dr. Mohan Kathaperumal, Dr. Jack Moon, Mr. Chris White, Mr. Richard Shafer and Mr. Lila Dahal.

I would like to thank my seniors from the lab who helped me in various aspects of my research and without their support many of the results in this dissertation would not have

been possible. I am grateful to Dr. Atom Watanabe, Dr. Siddharth Ravichandran, Dr. Muhammad Ali, Dr. Hakki Torrun and Dr. Sridhar Sivapurapu for their guidance during the first year of my PhD which helped me to get started with cleanroom fabrication and RF design tools.

I owe special thanks and gratitude to all my friends and colleagues from my lab, Georgia Tech Packaging Research Center. I had a great time with everyone. Thanks a lot to Dr. Osama Waqar, Serhat Erdogan, Lakshmi Narasimha, Kai Qi Huang, Xiaofan Jia, Xingchen Li, Nahid Aslani, Venkatesh Avula, Pragna Bhaskar, Christopher Blancher, Oluwaseyi Akiwande, Seunghyup Han, Joon Kim, Pavritha Kuppakone, Prahlad Murali, Eric Huang, Mercy Daniel Aguebor, Yiliang Guo, Dr. Claudio Alvarez, Dr. Majid Ahadi and Dr. Huan Yu. I have developed great friendship with all of you and I will cherish that for the rest of my life.

I would like to say thanks to my friends in Atlanta: Ahsan, Saad, Wajahat, Zulfiqar, Nazar, Ahmad, Ammar, Ahmed Usman, Dr. Aqeel Anwar, Dr. Muhammad Ali, Ahmal Jawad Zafar, Shehzaan Farooqui, Dr. Muhammad Ali Murtaza, Dr. Talha Mubeen, Dr. Arslan Shehzad, Dr. Zainad Arshad, Dr. Ismail, Shaarif Sajid, Bilal Mufti, Dr. Saad Javaid and Ahmad Waseem. Their company made Atlanta fun and full of joy.

Finally, I would like to express my deepest gratitude to my family. Thanks a lot, to my spouse Maida for all the love and continuous encouragement which kept me going and really helped me during the stressful times of my PhD. Thanks to her for happily coping up with my busy and unusual working routines. I want to thank my mother (Nighat) and father (Waseem) for always believing in me, giving me the freedom to follow my dreams, and constantly loving and supporting me in every phase of my life. I also want to thank my

brother (Faiz) and sister (Mahnoor) for their support and taking care of our home and parents while I was away and busy in my graduate studies. I wish them success in their lives. I would also like to thank my in-laws (uncle Umar Farooq, aunty Alia Farooq, sister Maryam and brother Maaz) for their love, prayers, and support.

Without the contribution of everyone mentioned above, none of my work and success was possible. I enjoyed every bit of my PhD and my stay at Georgia Tech. I wish everyone all the best for their lives.

This work was supported in part by ASCENT, one of the six centers in JUMP, a Semiconductor Research Corporation (SRC) program sponsored by DARPA and in part by the Georgia Tech Packaging Research Center (PRC).

TABLE OF CONTENTS

LIST OF TABLES

LIST OF FIGURES

LIST OF SYMBOLS AND ABBREVIATIONS

ABF	Ajinomoto Build Up Film
ADS	Advance Design System
AGC	Asahi Glass Company
CBCPW	Conductor Backed Coplanar Waveguide
CPW	Coplanar Waveguide
HFSS	High Frequency Structure Simulation
Hi R	High Resistivity
LCP	Liquid Crystal Polymer
LRRM	Line-Reflect-Reflect-Match
LTCC	Low Temperature Co-Fired Ceramics
mmWave	Millimeter Wave
MS	Microstrip
PR	Photoresist
RF	Radio Frequency
SIW	Substrate Integrated Waveguide
TRL	Thru-Reflect-Line
VNA	Vector Network Analyzer

SUMMARY

The aim of this thesis is to develop glass interposer technology for sub-THz frequency region for supporting 6G wireless networks. Next generation systems will require carrier frequencies above 100 GHz to provide multi-GHz bandwidth necessary to support data rates in the order of 10 Gbps. Glass interposer technology is gaining attention for supporting these sub-THz modules because of its unique ability to support fine features sizes at low cost with superior electrical performance. This work contributes to the development of glass interposer technology for the sub-THz frequency region by providing the first electrical characterization results (dielectric constant and loss tangent) for glass interposers for a broad frequency range of 20 GHz to 170 GHz. The extracted results can be used to accurately design RF components in glass interposer technology for sub-THz frequency region. This thesis also presents the design, fabrication, and measurements for interconnects (microstrip lines, CPWs and SIWs) on glass interposers up to 170 GHz and compares the performance with other state of the art alternatives.

This work also presents of a new class of filters in SIW technology called Blind Via Filters, which are designed by using blind vias in SIW. The performance and size of Blind Via Filters have been compared with traditional SIW cavity-based filters. Blind Via Filters are only a third of the size of their traditional counterparts for similar passband performance which implies that class of filters is promising for designing miniaturized filters in SIW technology.

This thesis also presents the design, fabrication and characterization of ultra-low loss Air Filled SIWs in multi-layer laminate stack up. The performance of the Air Filled SIWs has been compared with solid SIWs fabricated in the same material stack up. Air Filled SIWs show 50% less insertion loss compared to the solid counterparts. The performance has also been compared with other SIWs operating in D-band.

CHAPTER 1. INTRODUCTION

1.1 Wireless Communication and Role of mm-Wave Frequency Region

Wireless networks have seen tremendous proliferation in the past few decades. Five generations of cellular communication systems have been deployed in the span of last fifty years. In 1980s, first generation was introduced which used analog FM technology to enable basic voice communication. In 1992, second generation (2G) used digital modulations and multiple access technologies to improve the spectral efficiency and bring low data rate internet to consumers. Third (3G) and fourth generations (4G) were emerged in 2001 and 2011 respectively. 3G enabled high-definition video calling and streaming while 4G brought data rate speeds up to 1 Gbps. Currently, we are in fifth generation (5G) of these cellular networks. The main difference between 4G and 5G was the use of much wider spectrum allocations in 5G from the unutilized mm-Wave frequency region to support bandwidths in the order of 1 GHz [1].

Data rate is the most important parameter which drives all the wireless applications and with every generation we see approximately 10x increase in data rates. The typical data rates for different generations are given in Figure 1. Consistent with the trend, 5G networks can achieve data rates up to 10 Gbps. This data rate will continue to support the current wireless applications for this decade but in coming years, new applications in the areas of wireless cognition [2, 3], remote sensing[4-6] , high resolution imaging [7-9], multi-gigabit communication [10-12] and centimeter level positioning[7, 13] will emerge, and they will require data rates in the order of 100 Gbps [14].

To achieve such high data rates, use of wide multi-gigabit physical bandwidth (~8 GHz to 10 GHz) is essential which implies that the next generation communication systems will use carrier frequencies above 100 GHz (like 140 GHz, 220 GHz, 330 GHz) [15]. These frequencies will be referred as sub-THz frequencies in this thesis.

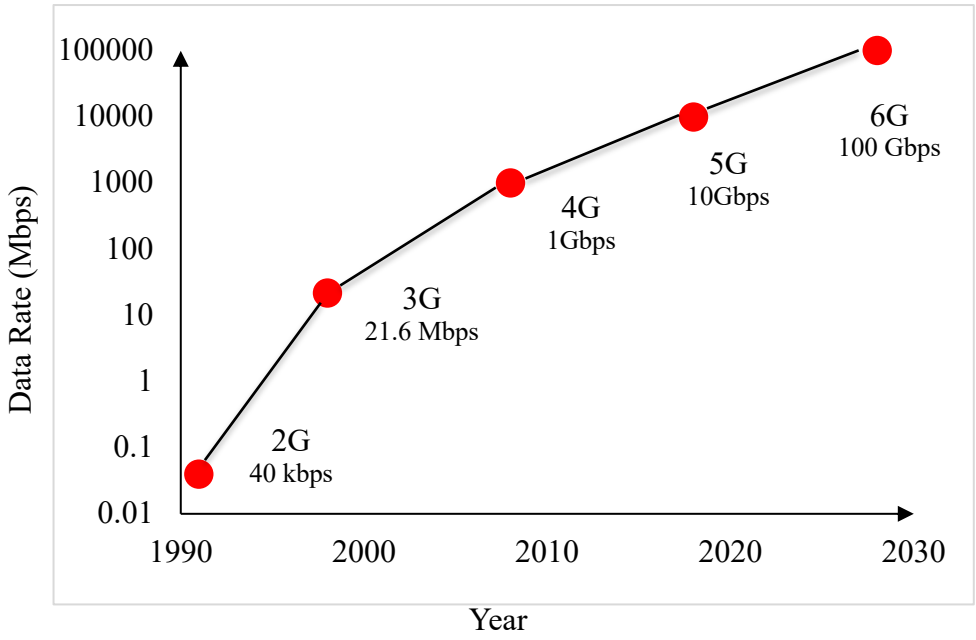

Figure 1 Data rates for different generations

1.2 Challenges and Opportunities for sub-THz Radio Frequency Design

A typical radio architecture is given in Figure 2 [16]. It consists of transmitter, wireless channel, and receiver. The power received at the receiver ($P_{r,in}$) is given by equation (1). The receiver sensitivity ($P_{r,sen}$) is minimum measure of signal power that a receiver can detect to achieve a target bit error rate. It is determined by bandwidth (Δf), noise figure of receiver *(NF)* and minimum signal-to-noise *($SNR_{out,min}$)* ratio required for the specific modulation scheme. The use of wider bandwidth results in higher receiver sensitivity which

implies that more power is required at the receiver to establish a given link margin. To maximize the link margin for a given transmitted power, the sub-THz receivers need to support low loss interconnects (insertion loss 0.1 dB/mm to 0.5 dB/mm) and passives, high gain antenna arrays, low loss switches, and low noise amplifiers (LNA) are required. The parameters required to support a 5 dB link margin at 140 GHz are given in Table 1.

To meet the stringent performance requirements for sub-THz radios, this work focuses on the development of low loss interconnects and passives for frequencies above 100 GHz which is critical for supporting sub-THz radios.

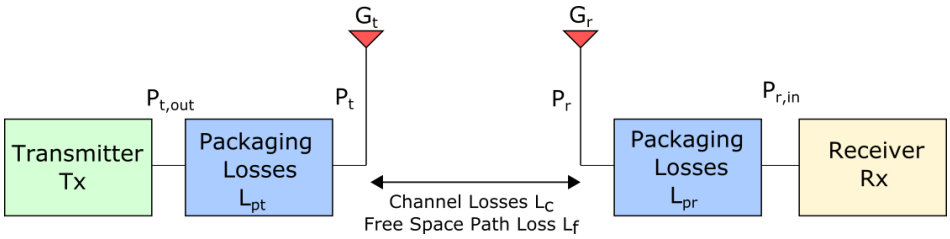

Figure 2 Typical radio architecture with losses

$$P_{r,in}(dBm) = P_{t,out} - L_{pt} + G_t - L_c - L_f + G_r - L_{pr} \qquad (1)$$

$$P_{r,sen}(dBm) = -174\,dBm/Hz + 10\log(\Delta f) + NF + SNR_{out,min} \qquad (2)$$

$$Link\ Margin\ (dB) = P_{r,in}(dBm) - P_{r,sen}(dBm) \qquad (3)$$

Table 1 Link Margin Calculations

Parameter	Value
Transmitted Power $\boldsymbol{P_{t,out}}$	37.5 dBm
Transmitter Antenna Gain $\boldsymbol{G_t}$	36 dB
Loss in Transmitter $\boldsymbol{L_t}$	3 dB
Free Space Path Loss (for 100 m distance at 140 GHz) $\boldsymbol{L_f}$	115.4 dB
Receiver Antenna Gain $\boldsymbol{G_r}$	24 dB
Losses in Receiver $\boldsymbol{L_r}$	3 dB
Miscellaneous losses (beam aiming loss, hardware life degradation loss, design margin, shadowing, atmospheric loss) $\boldsymbol{L_c}$	18 dB
Power Received $\boldsymbol{P_{r,in}}$	-41.9 dBm
Signal to Noise Ratio for QAM 256 $\boldsymbol{SNR_{out,min}}$	25 dB
Bandwidth Dependent Term **10log** ($\Delta \boldsymbol{f}$)	99.03 dB
Noise Figure **NF**	3 dB
Receiver Sensitivity $\boldsymbol{P_{r,sen}}$	-46.97 dBm
Link Margin	5 dB

In addition to the requirement of low insertion loss, form factor and cost also drive consumer industry. At sub-THz frequencies, material selection is critical because material properties determine the electrical, mechanical, and thermal performance of an RF component. Low permittivity and loss tangent are primary requirements but in addition, other parameters also determine the performance and suitability of a material for sub-THz applications. At these frequencies, surface roughness is extremely important because of sub-micron skin depth. Another important parameter is the Co-efficient of Thermal Expansion (CTE) which determines the assembly process and thermal reliability for the modules. Similarly thermal conductivity of the material is important because due to high heat fluxes (~100 W/cm^2) in sub-THz active components, thermal management is a major challenge. Cost of materials and fabrication processes also play key role in determining viability of solutions for the consumer applications. To meet all the stringent performance and cost requirements of sub-THz modules, use of new materials, processes and integration approaches is required which makes the role of packaging crucial [16]. To develop sub-THz modules a low-cost packaging platform is required which can support ultra-fine dimensions, has low insertion loss, good thermal properties and can integrate other components.

1.3 Brief Overview of Available Packaging Technologies

Over the last few decades, different platforms have been used for Radio Frequency (RF) integration which include epoxy material based printed circuits boards (PCB), Low Temperature Co-Fired Ceramics (LTCC), silicon wafer level packaging, low laminates like Liquid Crystal Polymer (LCP) [17]. LTCC is a good candidate for RF applications due to its low loss (loss tangent = 0.0007) electrical performance [18, 19]. LTCC packages can integrate 3D multi-layer conductor patterns and achieve dense integration by embedding

passives. In addition, LTCC packages are very robust against thermal stress due to their low co-efficient of thermal expansion (CTE) and high thermal conductivity. Due to the robustness and thermal reliability, LTCC packages are very popular for military applications. However, consumer industry is driven by cost, miniaturization, and functionality, and in these aspects, LTCC has limitations. Due to the use of screen-printing and co-firing processes, LTCC packages have large feature sizes (~ 100 μm), which results in low signal routing density. The use of thick materials often makes LTCC packages bulky. The use of higher processing temperatures and inability to support large sized panels result in the high cost which makes LTCC a less desirable solution for consumer applications.

Due to the limitations of LTCC technology, low loss laminate materials like Polytetrafluoroethylene (PTFE), PTFE composites, Rogers experimental polymers (RXPs) and Liquid Crystal Polymer (LCP) gained popularity as these polymers had low loss properties and they supported panel level processes to keep the cost low. Due to these reasons, they became a promising alternative to LTCC for mmWave applications. PTFE (also known as Teflon) was popular due to its very low loss tangent and low moisture intake, but high cost associated with fabrication of thin films and the need of additional bonding adhesives for multi-layer stack ups limited its use. In recent years, LCP emerged as an alternative to Teflon due to its excellent electrical properties (dielectric constant ε_r =3.17 and loss tangent tanδ =0.0055 to 0.009 from 100 GHz to 170 GHz) [20] . LCP was suitable for use in multilayer stack ups due to its availability in 25 μm thin films. It also supported cavity-based processes for chip embedding to achieve compact device integration with low footprint. Due to these merits, LCP was utilized in millimeter wave applications. Low loss LCP based transmission lines were demonstrated for W- [21] (75 GHz to 110 GHz) and D-

band [22] (110 GHz to 170 GHz). LCP based W-band integrated module with flip chip interconnect has been presented in [23]. Despite having good electrical properties and low cost, LCP is not well suited for the development of sub-THz modules because due to the large surface roughness, the minimum feature size on LCP is limited to 10 μm which is 10x more than desired (1 μm) minimum feature size for the development of sub-THz modules. In addition, CTE of LCP is relatively high in z-direction (200 ppm/K) which causes major reliability concerns for assembling chips on the substrates. Another major concern due to micron level surface roughness is significant increase in conductor losses at higher frequencies. It has been reported in [24] that surface roughness adds ~0.35dB/mm insertion loss for D-band substrate integrated waveguides (SIWs).

Silicon Wafer Level Packaging (WLP) enables near monolithic integration for RF modules. It was first proposed by Infineon as eWLB (embedded Wafer Level Ball Grid Array) and later modified by TSMC as Fan-Out Wafer Level Packaging (FOWLP) through the Integrated Fan-Out (InFO) process [25]. WLP reduces parasitics by eliminating the need for the chip assembly by directly routing the redistribution layers (RDL) from the chip pads. The InFO process supports very fine feature sizes (2 μm) which enables dense signal routing. However, the use of compression molding to form RDL can use result in large die-shifts [26]. In addition, due to high loss tangent of silicon (0.015), Through Silicon Via (TSVs) have large parasitics which makes WLP based solutions single sided, as the antenna and other high performance RF structures are integrated only on the top side of the module. The CTE mismatch between the silicon (3ppm/C) and PCB (15 ppm/C) can create reliability problems. In addition, inability to support large panel-based process results in high cost which can limit the application of FOWLP based solutions in consumer industry.

1.4 Glass Interposer Technology for mmWave Applications

Limitations of existing packaging technologies motivate the development of new solutions to support sub-THz modules. Glass interposer technology [27] is promising for developing sub-THz modules due to its unique ability to form silicon-like fine features (~1 µm) at low cost. Low loss of Thru Glass Vias (TGVs) enable double sided RDL in glass interposers which results in high density component integration. Glass interposers can support multiple metal layers depending upon the thickness glass core used. Current fabrication processes at Georgia Tech Packaging Research Center can support up to eight metal layers with a 200 µm thick glass core.

Glass substrates have tailorable CTE (between 3-11 ppm/K) and high dimensional stability (Young's modulus >60 GPa). These traits enable superior thermo-mechanical reliability as compared to organic packages. A traditional glass-based package is given in Figure 3.

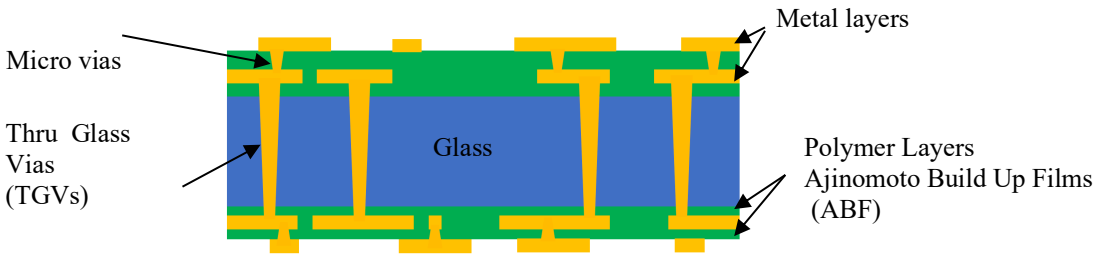

Figure 3 Structure of a glass-based package

In a glass-based package, glass core is laminated with thin dry films on both sides. The use of dry film makes the fabrication of glass interposers compatible with laminate-friendly manufacturing lines. In addition to the process compatibility using laminated glass also has

several other benefits. Copper has better adhesion with dry film polymers compared to the bare glass. Polymer layer also serves as a stress buffer which prevents crack generation and propagation in glass panels during fabrication. Laminating glass panels enable via-in-vias for metallizing Through-Glass-Via (TGV) thus improving the thermal-cycling reliability in both TGVs and redistribution layers (RDL). Ajinomoto Build-up Film (ABF) is a dry film used to laminate the glass because of its excellent compatibility with current panel-scale substrate manufacturing. It is available in various thicknesses such as 5µm, 15µm and 72.5 µm. ABF dry film is compatible with high-throughput vacuum lamination process and conventional wet processes for electroless copper deposition. ABF also has suitable chemical, mechanical, and thermo-mechanical properties to support large-body sized packages necessary for such applications [28].

A summary of the key parameters of the packaging platforms is given in Table 2. Based on them, glass-based packaging platform looks attractive for supporting sub-THz modules as it has capability of supporting ultra-fine features at a moderate cost with good reliability. To date, glass interposer technology has been extensively used to support millimeter-wave components for 5G applications for frequencies below 50 GHz.

Table 2 Key Parameters for Different Packaging Platforms

Key Parameter	LTCC	Organic Laminate (LCP)	FOWLP (EMC)	Silicon Interposer	Glass
Dielectric Constant	9.8	3.17	3.68	11.7	5-7
Loss Tangent	0.0007	0.006@140GHz	0.008	0.004 @35GHz	0.008 @100GHz
Surface Roughness (nm)	120	350	1000	1 - 60	<1
CTE (ppm/K)	6.7	18(x and y) 200 (z)	30	2.6 - 3.3	3-9
Young's Modulus (Gpa)	90-150	3.4 -4.0	22	168.9	50-90
Large Panel Processing	No	Yes	No	No	Yes
Cost	Very high	Low	High	High	Moderate
Min. Feature Size	100 μm	10 μm	2 μm	1 μm	1 μm
Component Density	Low	Medium	High	High	High
Thickness	High	medium	Fine RDL	Fine RDL	Ultra-Fine RDL

Good	Acceptable	Bad

1.5 Contributions of this work

Glass interposer technology is gaining attention for supporting sub-THz modules due to its ability to form silicon-like fine pitch lines and spaces at low cost. So far, the work done for glass interposers was limited to 50 GHz. The goal of this thesis is to contribute towards the development of glass interposer technology for frequencies above 100 GHz by designing, fabricating, and characterizing RF interconnects and filters in glass interposer technology. This thesis also contributed to the development of SIW technology by presenting miniaturized SIW filters and ultra-low loss SIW interconnects. More specifically the salient contributions of this thesis are summarized below:

- First results for electrical characterization results (dielectric constant and loss tangent) for glass interposers using microstrip ring resonator method for a very broad frequency range of 20 GHz to 170 GHz. The extracted dielectric constant and loss tangent values can be used to accurately design RF components in glass interposers.
- First demonstration of planar interconnects (microstrip lines, CPWs) on glass substrates up to 170 GHz. The performance has been compared with other state of the art published work.
- First demonstration of D-band (110 GHz to 170 GHz) SIW interconnects embedded in glass interposers. The performance has been compared with SIWs fabricated in other interposer technologies.

- First demonstration of D-band (110 GHz to 170 GHz) SIW cavity filters in glass interposers. Two different shapes of SIW cavity namely square and rectangle were used to design the filters and the response was compared.

  Other important novel contributions include:

- Design, fabrication, and measurements of Novel Blind Via SIW Filters which are only 30% of the size compared traditional SIW cavity filters fabricated in the same material stack up. Blind via filter technology is promising for making miniaturized SIW filters for supporting mmWave modules.
- Design, fabrication, and measurements of Novel ultra-low loss Air Filled SIW technology using multi-layer laminate stack up which achieves 0.16 dB/mm measured insertion loss in D-band. The insertion loss has been compared with other low loss SIWs published in literature.

1.6 Organization of Dissertation

Rest of the thesis is organized as follows: Chapter 2 provides the results for electrical characterization of ABF/glass/ABF substrates and benchmarks the performance of glass based microstrip lines and CPWs up to 170 GHz, Chapter 3 presents the first demonstration of SIWs embedded in glass interposers and compares the performance with SIWs in other interposer technologies, Chapter 4 presents SIW cavity based filters in glass interposers and compares the performance with other state of the art published filters, Chapter 5 presents the design method for blind via filters, discusses the challenges in fabrication and limitation of a 2-metal layer stack up for designing blind via filters, introduces a new material stack up with 3 metal layers and provides the first demonstration of Novel Blind Via Filters and then compares the size and performance to traditional SIW cavity filters

designed and fabricated in the same material stack up, Chapter 6 presents the demonstration of microstrip lines and SIWs on the new material stack-up and compares the performance with other state of the art published work and microstrip lines and SIWs reported in Chapter 2 and Chapter 3 respectively, Chapter 7 presents Ultra-low loss Air Filled SIWs using multi-layer laminate based stack-up and compares the performance with other low loss SIWs and Chapter 8 provides summary and future work.

CHAPTER 2. ELECTRICAL CHARACTERIZATION OF ABF/GLASS/ABF SUBSTRATES

Designing RF and microwave components require a good quantitative measure of the electrical properties of the materials used. ABF/glass/ABF stack up is the basic structural block of glass-based packages and its high frequency characterization is necessary for the development of glass-based packaging in the mmWave and sub-THz frequency region.

2.1 Brief Overview of the Material Characterization Methods

Material characterization methods can be largely divided into two categories namely resonant and non-resonant methods. Resonant methods are used to extract electrical properties (dielectric constant and loss tangent) at a single or multiple discrete frequencies whereas non-resonant methods are used to obtain material properties for a broad range of frequencies [29]. Free space method is a popular non-resonant material characterization method. In this method a sample is placed between two horn antennas and its electrical properties are extracted by measuring the scattering parameters. For characterization in the THz range, methods like Fourier Transform Infrared Spectroscopy and Time Domain Spectroscopy [30] are used but the use of these methods is limited because of due to the requirement of sophisticated equipment.

Resonant methods are generally better for the characterization of low loss materials. Resonant cavities have very high Q and resonant modes can be determined as functions of the relative permittivity and dimensions of the cavity. Split cavity resonator method [31] is an accurate technique used to extract electrical properties of a material at a resonant

frequency. This method is often used but in mmWave region where often material properties vary and hence electrical properties at multiple frequencies is required, the use of split cavity method is limited for since it requires an elaborate test setup, and one test setup provides material properties at only one frequency. Microstrip Ring Resonator (MRR) [32] method provides reliable characterization results at multiple frequencies with minimal test setup. It has been reported in [21] that, the results of MRR method falls well within the error tolerance range of cavity resonator method. Due to this reason, MRR method has been chosen to extract the electrical properties of ABF/glass/ABF stack up for a broad frequency range of 20 GHz to 170 GHz [28].

2.2 Material Characterization Test Vehicle Design

The material stack-up consisted of 100-µm Asahi Glass Company (AGC) ENA1 glass core. ENA1 is an alkali-free boro-aluminosilicate glass that serves as a good interposer substrate due to its good chemical resistance and ability to support precise control over the dimensions of laser drilled vias due to its unique refractive properties. The glass core is laminated with a 15-µm polymer film (ABF GL102) on both sides. The test vehicle consisted of three structures namely Microstrip Ring Resonator (MRR), microstrip lines and Coplanar Waveguides (CPWs). The electrical properties were extracted using MRRs. Microstrip lines and CPWs were designed to measure the performance of interconnects on ABF/glass/ABF stack up till 170 GHz and validate the extracted electrical properties by performing model to hardware correlation.

The designed structures were measured by using ground-signal-ground (GSG) RF probes. This test vehicle was designed to extract material properties from 20 GHz to 170 GHz. To

cover the desired frequency range, two different sets of probes were used. Cascade ACP110 (200-μm pitch) probes were used to measure the structures below 110 GHz and Cascade infinity probes I170 probes (75-μm pitch) were used for the *D*-band (110–170 GHz). Since the pitch was different, separate structures with different RF probe pads were designed to be consistent with the RF probes. The design procedure for each structure is described below.

2.2.1 Microstrip Ring Resonator

Microstrip ring resonator is a closed-loop ring which is fed by two microstrip lines. There is a coupling gap between the ring and the feed lines. The radius of the microstrip ring is inversely related with the resonant frequency. The S_{21} response of MRR has resonant periodic peaks. The effective permittivity of a material is a function of the location of these resonant peaks whereas the loss tangent is a function of quality factor of the peaks. The design equation used to design MRRs is given below:

$$f_n = \frac{nc}{2\pi r_m \sqrt{\varepsilon_{eff}}} \qquad (4)$$

where f_n corresponds to the nth resonance, r_m is the mean radius of the ring, and c is speed of light. To calculate the mean radius of the ring, n is set to 1.

MRR resonates at discrete frequency points which are multiple of the fundamental resonant frequency. To capture material properties at multiple frequencies, MRRs with three different radii were designed. The fundamental frequencies for MRRs were at 5 GHz, 10 GHz and 15 GHz. Since the designed MRRs were to be measured using GSG RF probes, conductor backed CPW (CBCPW) to MS transitions were designed. The designed MRR

with CBCPW to MS transitions is given in Figure 4b. To keep the fabrication process simple, via-less CBCPW probe pads were designed according to the guidelines presented in [33] . Total width of the probe pads should be less than than $\lambda_g/2$ to avoid the parasitic parallel plate waveguide mode [34]. The designed CBCPW to MS transition is given in Figure 4d.

Initially, two sets of MRRs were designed to be measured with different probes (200 µm and 75 µm) to cover entire frequency range from 20 GHz to 170 GHz. After initial measurements it was observed that via-less CBCPW to microstrip transitions were showing high insertion loss below 40 GHz. Due to this reason, resonant peaks were not captured for frequencies below 40 GHz. This can be attributed to the weak coupling between the ground pads of CBCPW probe pads and the ground plane. To capture resonant peaks below 40 GHz, a third set of MRRs was designed with vias on the ground pads of CBCPW to connect them to the ground plane. As a result, three sets of MRRs were used to cover the entire frequency range. The name of the sets along with the pitch size and frequency range is described in Table 3 below.

Table 3 Properties of sets of MRRs used for material characterization

Name	Pitch (µm)	Vias	Fundamental Frequency (GHz)	Frequency Range (GHz)
Set 1	200	Yes	5,10	20 to 60
Set 2	200	No	10,15	75 to 110
Set 3	75	No	10,15	110 to 170

Since the designed MRRs were fed using CBCPW to MS transitions, the measurements after LRRM calibration had the effects of these probe pads and transitions. To de-embed the response of the MRRs, Thru-Reflect-Line (TRL) structures were designed to shift the reference plane. The reference plane after TRL calibration [35] is shown in Figure 4b.

2.2.2 Coplanar Waveguide (CPW) transmission lines

CPW is a commonly used electrical planar transmission line. It consists of a signal trace which is surrounded by two ground planes placed on either side of the signal trace. Since all the conductors lie in the same plane, only one metal layer is required to design CPWs. To investigate the high frequency performance of ABF/glass/ABF based interconnects, CPWs were designed. LineCalc utility in Keysight Advance Design System (ADS) [36] was used to calculate the dimensions for CPWs. Like case of CBCPW probe pads, two sets were designed to be consistent with the GSG RF probes. To relax the fabrication requirements, 70 Ω impedance was chosen. Ansys High Frequency Structure Simulation (HFSS) [37] was used to simulate the designed CPWs. Since ground plane was not required for CPWs, only the top side of the stack up was metallized during fabrication. The designed CPW is given in Figure 4e.

2.2.3 Microstrip Lines

To investigate the performance of ABF/glass/ABF stack up based interconnects, microstrip lines were designed. As described in [38], characteristic impedance and dispersion in a microstrip line are inversely related. To have lower dispersion, microstrip lines with 70 Ω

impedance were designed. The physical dimensions were calculated using LineCalc and then models were simulated in Ansys HFSS. CBCPW to microstrip transitions were added to probe the designed microstrip lines. To de-embed the response of the microstrip line, TRL calibration was used. The length of the feed line was kept same as in MRRs so the same set of TRLs can be used for both measurements. The reference plane after TRL calibration is shown in Figure 4c.

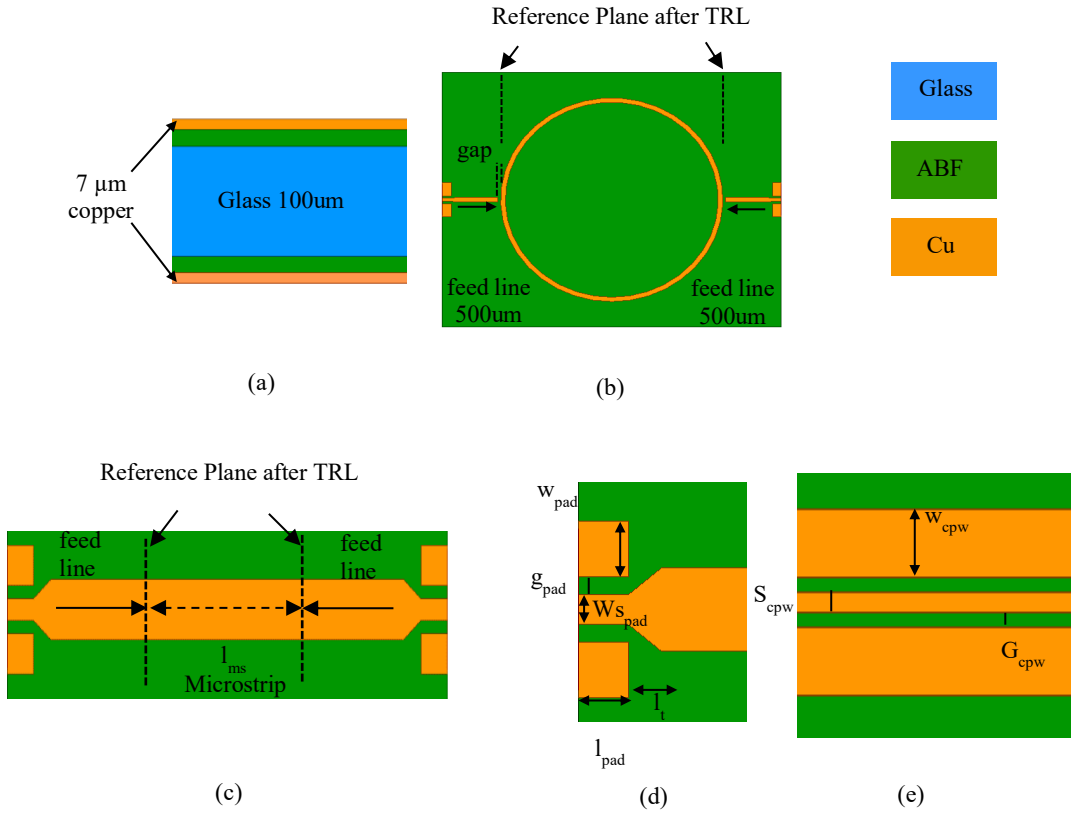

Figure 4 Material characterization test vehicle (a) material stack up (b) MRR (c) microstrip line (d) CBCPW probe pad (e) CPW

The dimensions of the structures (MRRs, CPWs, microstrip lines) are given in Table 4.

Table 4 Dimensions of the Test Vehicle Fabrication of the Characterization Test Vehicle

Structure	Parameter	200 µm Pitch Probe	75 µm Pitch Probe
CPW	S_{cpw}	80	50
	g_{cpw}	38	23
	W_{cpw}	180	100
CBCPW Probe Pads	Ws_{pad}	90	45
	g_{pad}	50	27
	l_{pad}	150	75
	l_t	70	50
	w_{pad}	250	85
Microstrip	w_{ms}	127	127
	l_{ms}	3200	3500
MRR 5GHz	r_m	5400	N/A
MRR10GHz	r_m	2700	2700
MRR15GHz	r_m	N/A	1800
	gap	30	30
TRLs	feed line	500	750
	line1	400 (Set1)	425 (Set 3)
	line2	500 (Set 2)	N/A

2.3 Fabrication

The designed structures were fabricated on two panels namely microstrip panel and CPW panel. Since CPW lines did not require conductor backing, only top side of the material stack up was metallized. For microstrip panel, both sides of the stack up were metallized because MRRs and microstrip lines required ground plane. The process flow is described in Figure 5. In the first step, bare glass panels were treated with Oxygen Plasma for 5 minutes. Then these panels were treated with silane for 20 minutes at 70º C. In the next step, 15 μm thick dry film polymer (ABF GL102) was vacuum laminated onto glass panels using Meiki Laminator. Copper was patterned using Semi-Additive Process (SAP) [39]. Then copper seed layer was deposited using an electroless Cu deposition. The targeted thickness for Cu seed layer was ~300 μm. 7 μm-thick dry-film positive photoresist (Hitachi RY5107) was then vacuum laminated on the seed layer and exposed using a mask-less aligner. Copper was electroplated to 7 μm in height after which, the Cu seed etched using differential etcher.

The dimensions of the fabricated samples were measured using Zeta Optical Profiler. The fabricated widths varied by 2 μm to 4 μm at various samples. This can be attributed to various parameters in fabrication which are difficult to precisely control. This discrepancy represents 1.5-3% variation with respect to the designed width of the microstrip line (127 μm). This resulted between 1 to 3Ω impedance change in microstrip and CPW lines, respectively. Copper surface roughness was measured on various samples using Zeta Optical Profilometer. The rms value for the measured surface roughness varied between 180 nm to 275 nm on different samples with majority of the readings around 200nm. The fabricated samples are shown in Figure 6.

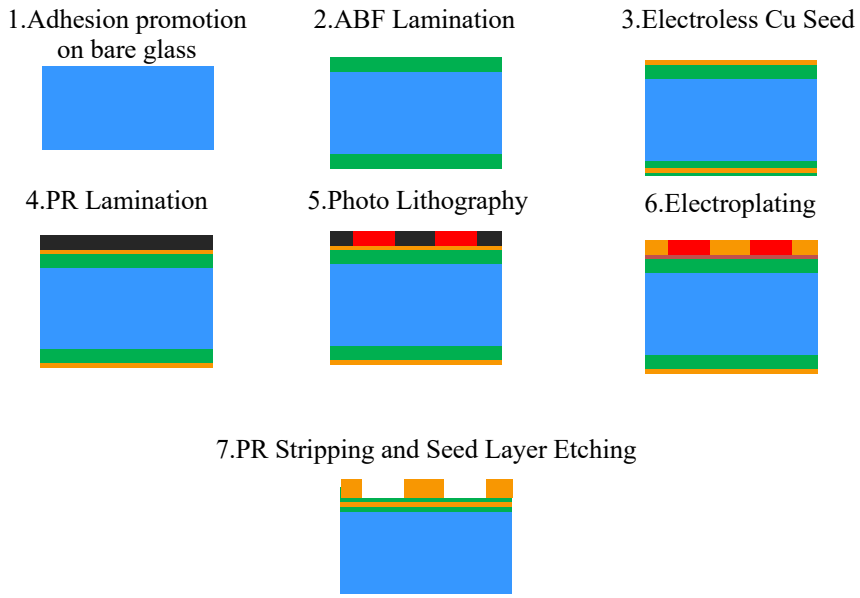

Figure 5 Process flow for fabrication

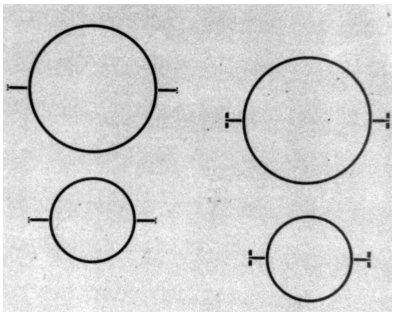

(a)

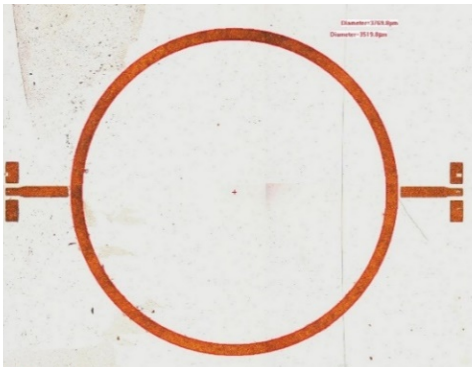

(b)

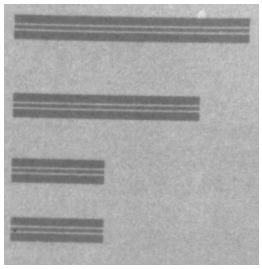

(c)

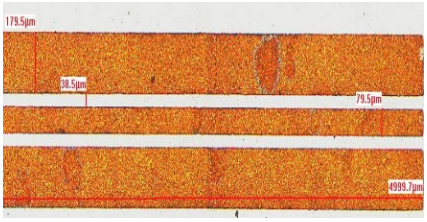

(d)

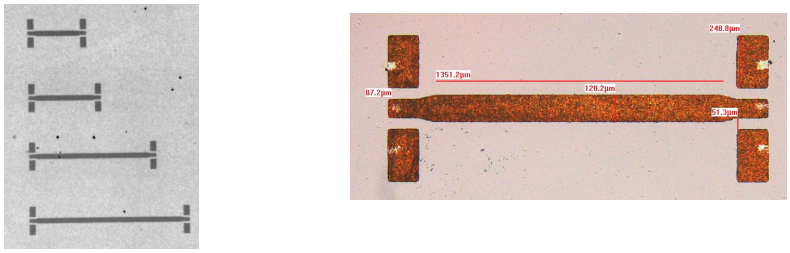

(e) (f)

Figure 6 Fabricated Samples(a) MRRs coupon (b) MRR with CBCPW to microstrip transitions (c) CPWs coupon (d) CPW line (e) microstrip lines coupon (c) microstrip line with CBCPW to microstrip transitions

2.4 Electrical Measurements

The designed samples were measured in the frequency range of 20 GHz to 170 GHz. The measurement equipment and results test structures are described in the sub-sections below:

2.4.1 Measurement Equipment

Two different measurement set ups were used to cover the frequency range from 20 GHz to 170 GHz. For 20 GHz to 110 GHz, Anritsu VNA (ME7808) and frequency extenders 3742A-EW were used. Cascade ACP-110-GSG-200 probes were used to probe these samples. For 110 GHz to 170 GHz, Agilent E8361C vector network analyzer, millimeter wave controller and frequency extenders (V06VNA2) were used. Both measurement set-ups are given in Figure 7. Cascade infinity probes 170-S-GSG-75-BT were used to probe these samples. LRRM calibration was performed using calibration substrates and Wincal software.

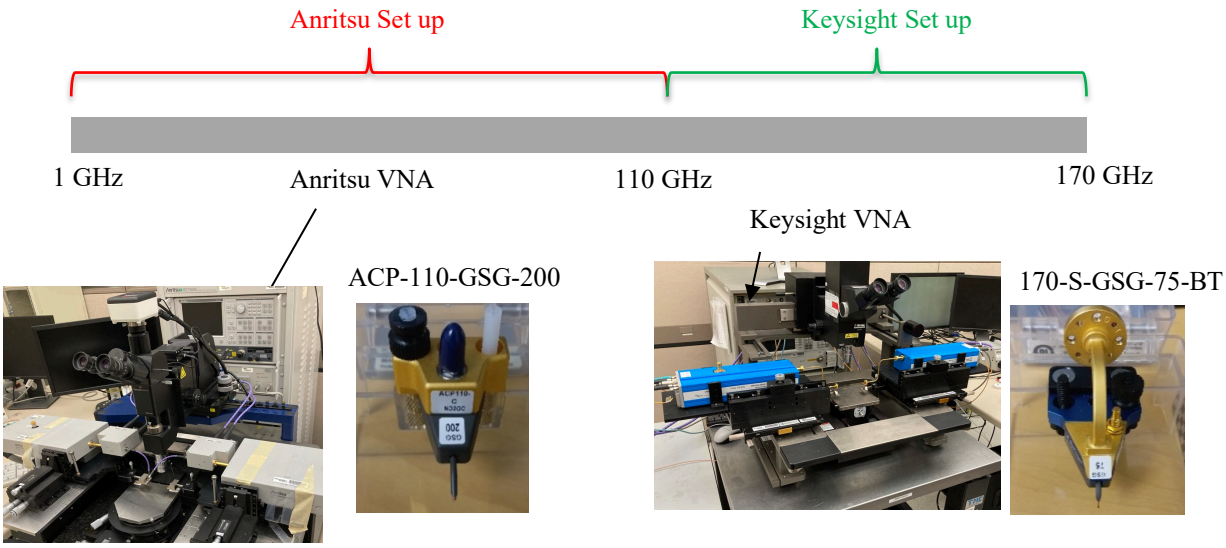

Figure 7 Measurement set up from 20 GHz to 170 GHz

2.4.2 Initial Measurements

This sub-section will describe the initial measurement results in which poor electrical performance of via-less CBCPW probe pads was observed at frequencies below 40 GHz. Scattering parameters S21 (dB) for MRR and thru structure are given in Figure 8. In the response of MRR, resonances below 40 GHz are not clearly captured. It can be seen in the response of the thru structure which consists of back-to-back CBCPW to MS transitions that the insertion loss is very high below 40 GHz. As described before, this can be attributed to the weak coupling between the ground pads of CBCPW and ground plane and can be mitigated using vias on CBCPW ground pads to connect them to the ground plane. After observing these measurements, CBCPW to MS transitions with vias were used for designs operating below 60 GHz.

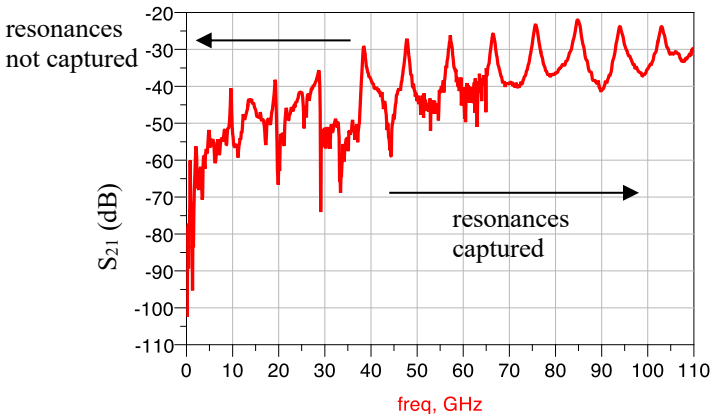

(a)

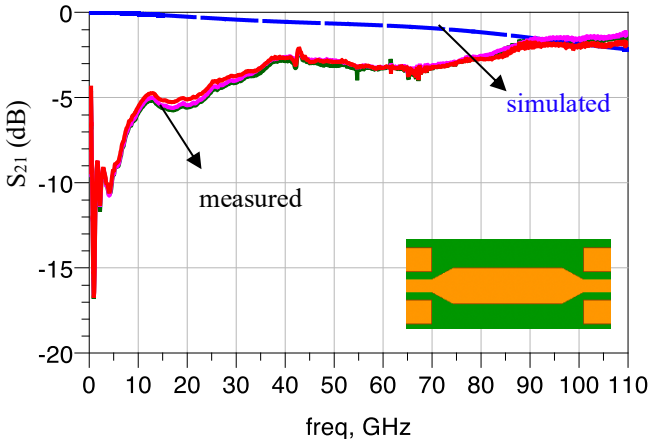

(b)

Figure 8 Initial measurements with via-less CBCPW probe pads (a) MRR (b) thru structure

2.4.3 Important consideration for probing of D-band samples

Landing probes on D-band samples is challenging because of the fine pitch of D-band probes. In this test vehicle while probing on a few samples the traces were getting buckled off or the scratch marks of the probes were uneven as shown in Figure 9and Figure 9b respectively. Often this problem can be attributed to non-planarity of the RF probe. When

a probe is tilted, it makes an uneven contact with the probe pads which can cause such issues. The probes were planarized carefully on a scratch substrate to get even probe scratch marks but still some traces got buckled off. To find the reason for this, the fabricated samples were carefully examine using Zeta Optical Profilometer. It was observed that D-band CPW probe pads were greatly affected by non-uniformity of electroplating. The planarity tolerance of D-band probes is less than a micron as reported by Cascade but in some of the samples, the variation was above 2 µm. This non-uniformity at the CPW probe pads was causing issues with D-band probing in this test vehicle. Due to this reason, in this test vehicle the probe pads were checked and the samples with accepted level of non-uniformity were used. To avoid this problem in future, fine dummy structures (25 µm by 25 µm) were included in the mask design to improve the uniformity at the probe pads.

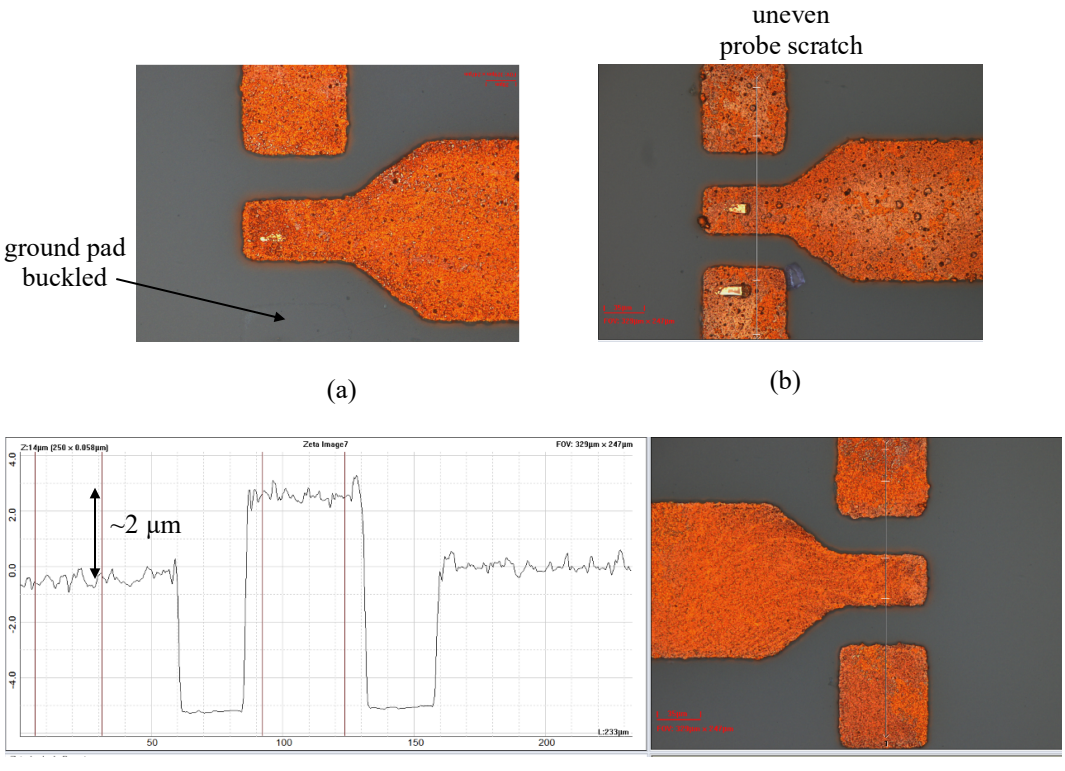

(a) (b)

(c)

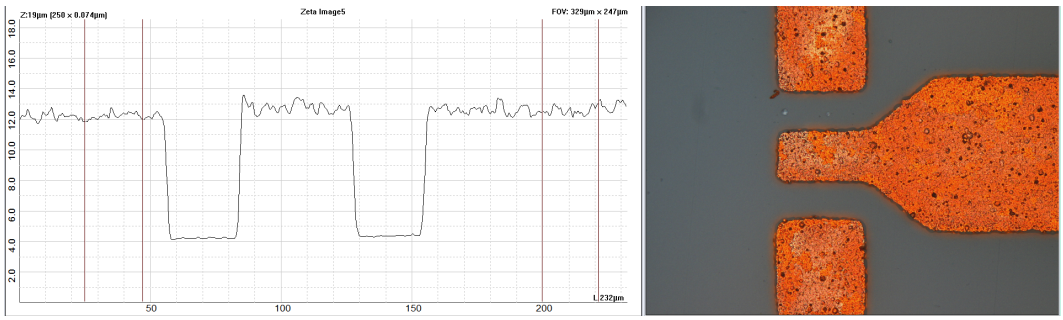

(d)

Figure 9 Probe pads in D-band samples (a) buckled pad (b) uneven probe scratch (c) sample with ~2 µm height variation in GSG (d) good sample with ~0.5 um variation

2.4.4 Microstrip Ring Resonators

MRRs and TRLs were first measured under LRRM calibration. Then TRL calibration was performed to de-embed the response of rings. Multiple samples were fabricated and measured to account for any process and statistical variations. Different measurements had good correlation with one another indicating the robustness of the fabrication and measurement process. Measured scattering parameters S_{21}(dB) for multiple samples are given in Figure 10.

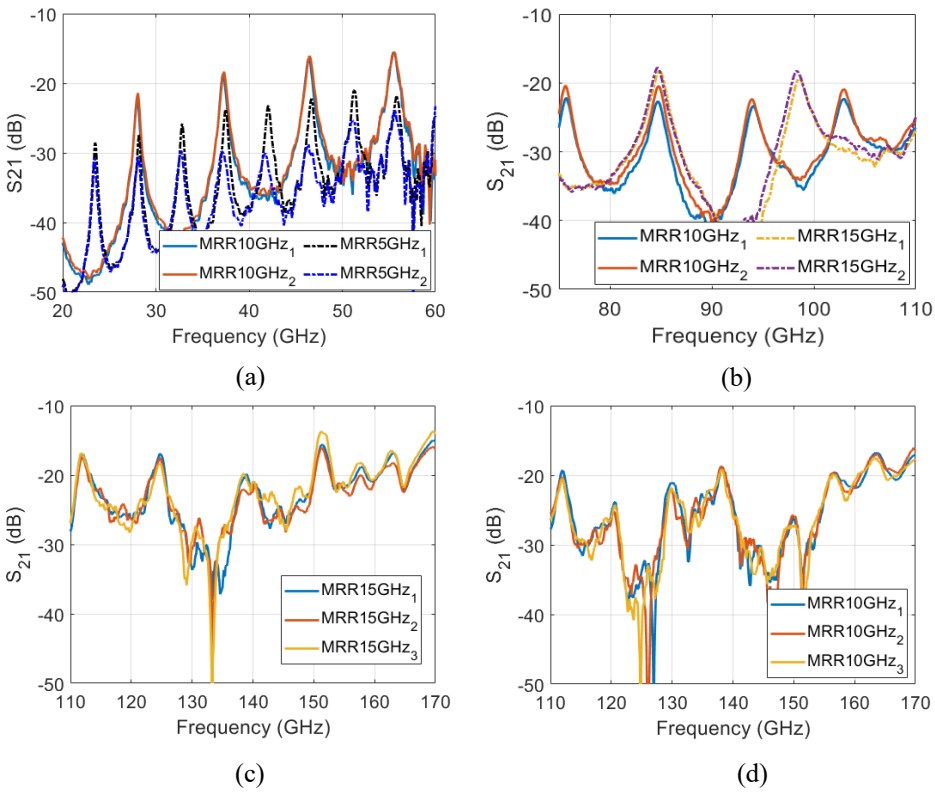

Figure 10 Extracted S21 (dB) of MRRs after TRL calibration (a) Set 1 20 GHz to 60 GHz (b) Set 2 75 GHz 110 GHz (c) Set 3 10 GHz MRRs 110 GHz to 170 GHz (d) Set 3 15 GHz MRRs 110 GHz to 170 GHz

Sharp resonances can be seen in the measured response of MRRs across the entire frequency region. In Set 1 and Set 2 all the resonances were captured however in Set 3 some resonant peaks were not clearly captured. This can be attributed to the sensitivity of samples in Set 3 (due to high frequency 110 GHz to 170 GHz) to variations in geometry, manufacturing tolerances and measurement uncertainties. As described in [21], only clearly captured peaks were used to extract electrical properties. It can also be observed in the measurements that quality factor of the peaks is decreasing with the increase in frequency. This indicates an increase in total loss (dielectric and conductor losses) with increasing frequency.

There are two models which are generally used to extract dielectric constant from the response MRR. The first model is Quasi-Static Model [40] which provides a good estimate but at high frequencies the accuracy of this model decreases because it doesn't include dispersion. The second model is dispersive model [41] which is described through equations below:

$$\varepsilon_{eff(f)} = \varepsilon_{rel(f)} - \frac{\varepsilon_{rel(f)} - \varepsilon_{eff(0)}}{1+P(f)} \quad (5)$$

$$P(f) = P_1 P_2 [(0.1844 + P_3 P_4) 10fh]^{1.5763} \quad (6)$$

$$P_1 = 0.27488 + \left[0.6315 + \frac{0.525}{(1+0.157fh)^{20}}\right] u - 0.065683 e^{-8.7513u} \quad (7)$$

$$P_2 = 0.33622\{1 - e[-0.03442\varepsilon_{rel(f)}]\} \quad (8)$$

$$P_3 = 0.0363(-4.6u)\left\{1 - e\left[-\frac{fh}{3.87}\right]^{4.97}\right\} \quad (9)$$

$$P_4 = 1 + 2.751\left\{1 - e\left[-\frac{\varepsilon_{rel(f)}}{(15.916)^8}\right]\right\} \quad (10)$$

where u=w/h

The values of effective permittivity ε_{eff} were calculated at each resonant frequency from the frequency response (S_{21}) of MRRs using eq (4). Next, relative permittivity (ε_{rel}) was calculated from effective permittivity using eq (5). Eq (5) involves a term P(f) which is defined by eq (6). P(f) includes terms P2 and P4 defined by eq (8) and eq (10) respectively. These terms involve the unknown term ε_{rel}. Therefore, a numerical technique, Secant Method was used to solve the eq (5). The extracted dielectric constant for ABF/glass/ABF stack-up is given in Figure 11. The vertical bars represent a confidence interval of 95%.

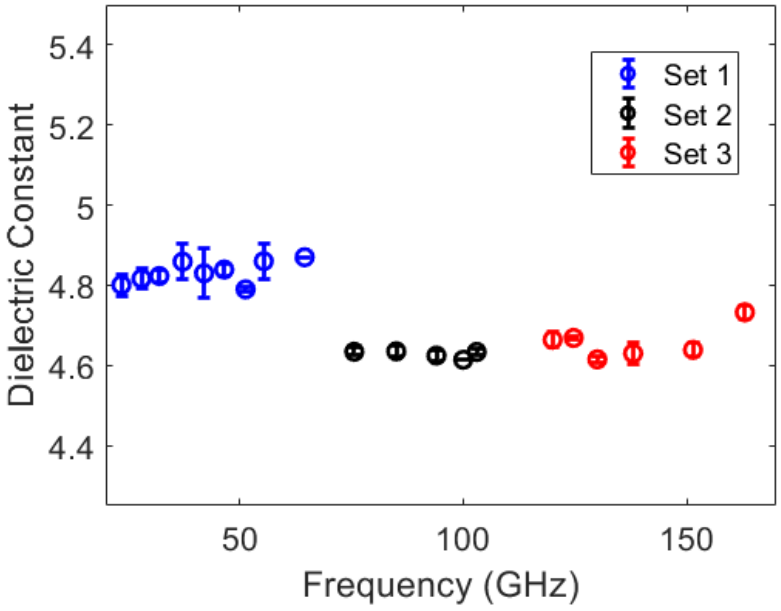

Figure 11 Extracted dielectric constant of ABF/glass/ABF stack-up

The extracted dielectric constant varied from 4.79 to 4.87 for the frequency range of 20 to 60 GHz. These values were extracted using MRRs in Set 1. For the frequency range of 75 GHz to 170 GHz, MRRs from Set 2 and Set 3 were used. For this frequency region, the average extracted dielectric constant was 4.72 with a variance of $\pm$0.1($\pm$2.1%). There was ~4% difference in the average dielectric constant between Set 1 and Set 2 and 3. This can be due to slighty high permittivity of glass at lower frequencies [42] . It is also important to note that Set 1 was fabricated later (after the initial measurements) on a different panel so this variation can also be due to discrepancies in dielectric thickness and slight changes in ring radii on different panels. A 10 µm change in substrate thickness and 50 µm change in MRR ring radius can change the extracted dielectric constant by 1% and 2% respectively. This dependency on the preciseness of fabricated structures and substrate thickness is a limitation of MRR method. However, in general 4% variation in dielectric

constant over such a broad frequency range is acceptable and can be attributed to several factors that are difficult to control precisely.

The loaded quality factors (Q_L) and unloaded quality factors (Q_U) at resonant frequencies were calculated using eq (11) and eq (12) respectively. Then, total loss (α_{total}) was calculated using eq (13). This total loss (α_{total}) has three components namely conductor loss (α_c), dielectric loss (α_d) and radiation loss. When the ratio of line width (wms) to mean radius (r_m) is much less than 0.2, MRR has no radiation losses. The only source of radiation is the open ended microstrip feed lines, and this effect has been removed by TRL calibration. Due to these reasons, it can be assumed that the total loss is a combination of only dielectric loss and conductor loss. To extract loss tangent of the dielectric material, conductor was theoretically calculated and subtracted from the total loss as described by eq (14). To theoretically calculate the conductor loss, a loss model presented in [43] was used. The loss model uses surface correction factor which depends on the surface roughness of copper. The copper surface roughness was measured on different samples using Zeta Optical Profilometer. The rms value for the measured surface roughness varied between 180 nm to 275 nm on different samples with majority of the readings around 200 nm. Hence 200 nm rms value was used in calculations. The loss tangent (tan(δ)) was calculated from dielectric loss by using eq (15). The extracted loss tangent is given in Figure 12. The vertical bars indicate confidence interval of 95%. The loss tangent varies from 0.004 to 0.015 in the frequency range of 20 GHz to 170 GHz.

$$Q_L = f_{nth}/BW_{3dB} \qquad (11)$$

$$Q_u = Q_L/(1 - 10^{\frac{s21}{20}}) \qquad (12)$$

$$\alpha_{total} = \pi/Q_u\lambda_g \qquad (13)$$

$$\alpha_d = \alpha_{total} - \alpha_c \quad (14)$$

$$\tan(\delta) = \frac{\alpha_d \lambda_0 \sqrt{\varepsilon_{eff}}(\varepsilon_r - 1)}{\pi \varepsilon_r (\varepsilon_{eff} - 1)} \quad (15)$$

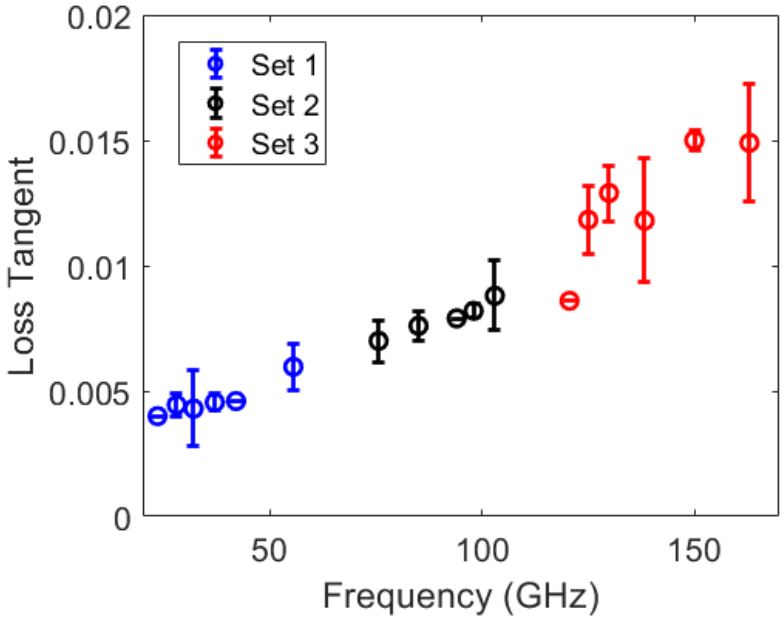

Figure 12 Extract loss tangent for ABF/glass/ABF stack-up

2.4.5 CPW lines

To measure the samples, CPW panel was placed on a metal chuck. Since CPW panel had no ground plane on the back sides, it was important to ensure that field lines did not interact with the metal chuck. Simulations were performed in Ansys HFSS to confirm the isolation of panel from the metal chuck. The measured scattering parameters (dB) of different samples CPW lines are given in Figure 13. Measurements on different samples are consistent with one another. The per unit insertion loss varies from 0.055 dB/mm to 0.5 dB/mm from 20 GHz to 170 GHz.

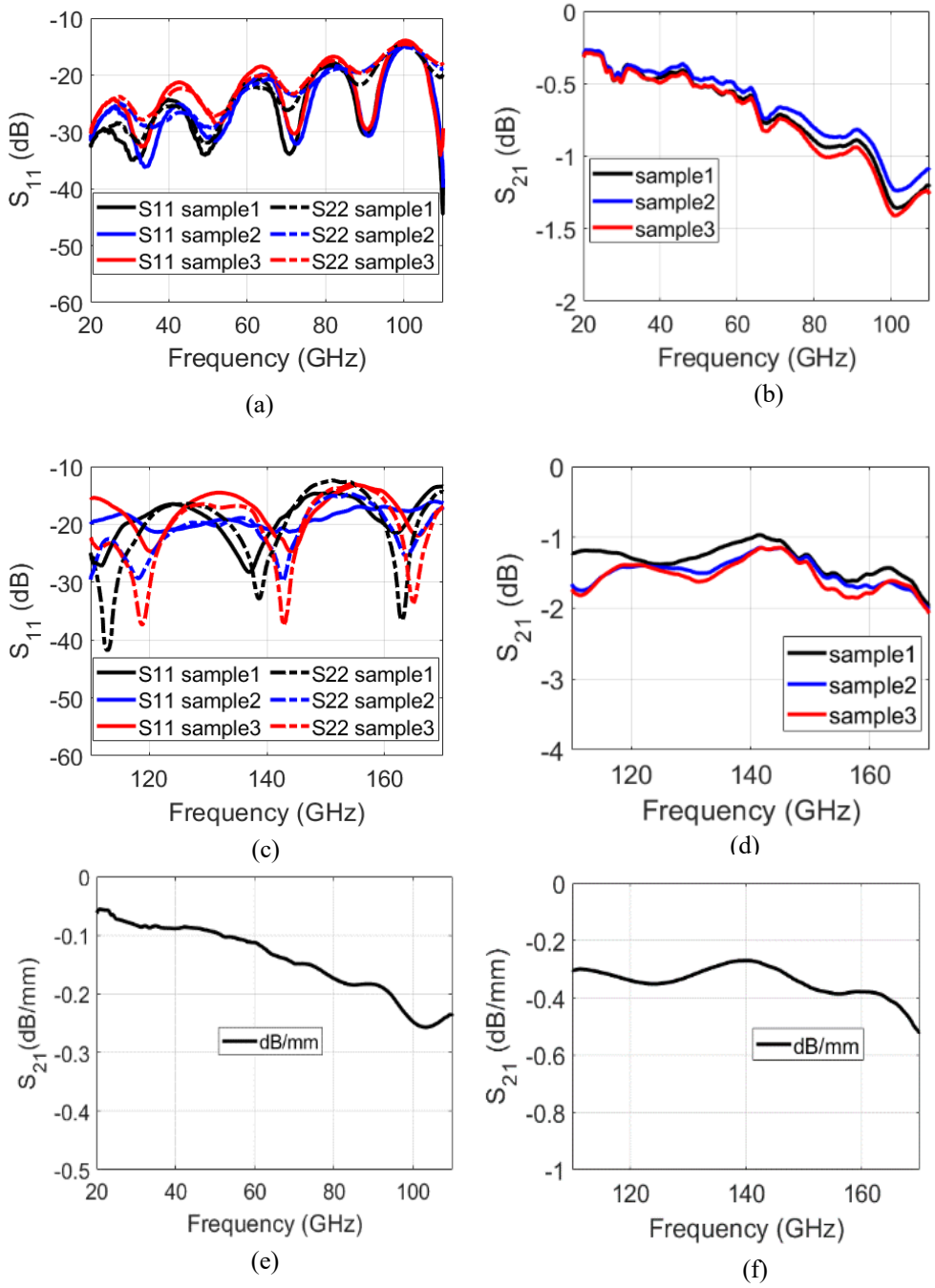

Figure 13 Measured Scattering Parameters of CPW Lines (a) S11 (dB) vs Freq(GHz) of 5 mm long CPW Lines (b) S21(dB) vs Freq(GHz) of 5 mm long CPW Lines (c) S11(dB) vs Freq(GHz) of 4 mm long CPW Lines (d) S21(dB) vs Freq(GHz) of 4 mm long CPW Lines (e) dB/mm for 20 GHz to 110 GHz (f) dB/mm for 110 GHz to 170 GHz

2.4.6 Microstrip lines

Like MRRs, microstrip lines were also fed by CBCPW to MS transitions therefore, TRL calibration was required to extract the insertion loss of microstrip lines. The initial measurements were taken under LRRM calibration. These measurements had the effects of CBCPW probe pads and CBCPW to MS transitions. The measured scattering parameters (dB) for thru and microstrip line are given in **Figure 14.**

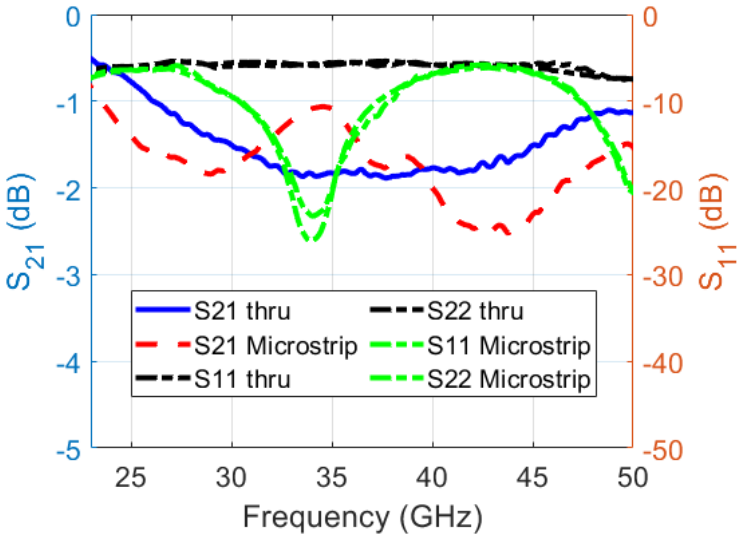

(a)

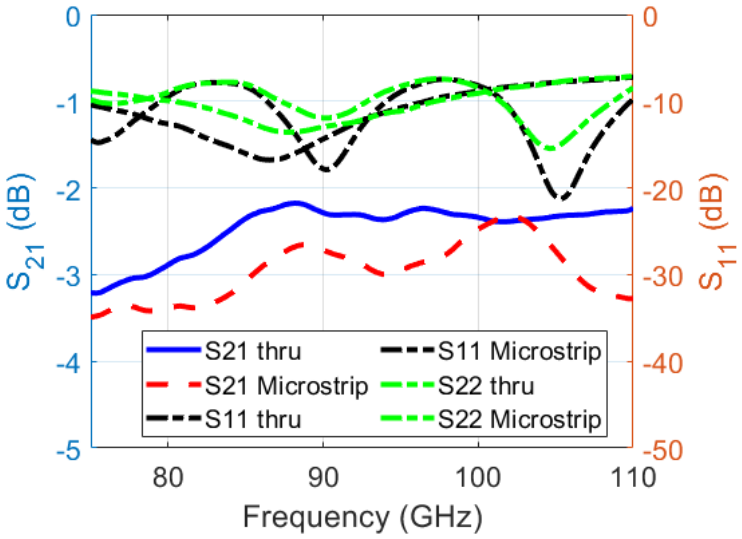

(b)

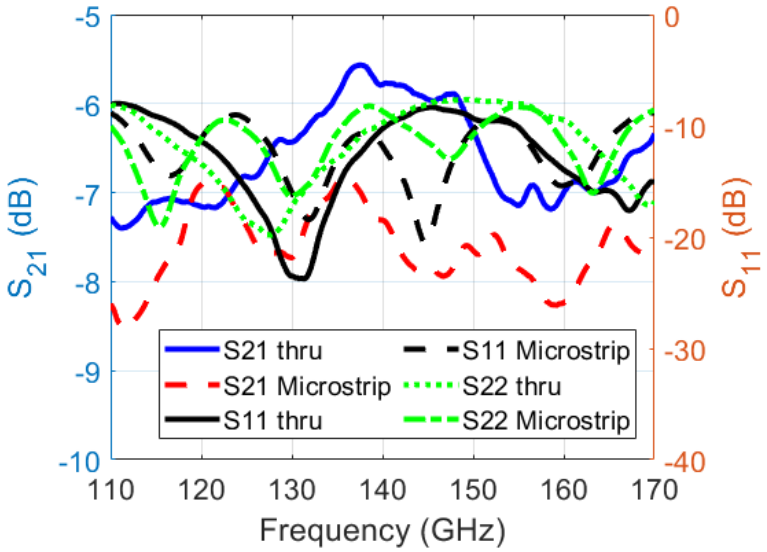

(c)

Figure 14 Scattering parameters of thru and microstrip line measured under LRRM calibration (a) 20 GHz to 50 GHz (b) 75 GHz to 110 GHz (c) 110 GHz to 170 GHz

The insertion loss of microstrip line after TRL calibration is given in Figure 15. Thru standard was very close to 0 dB after TRL calibration which implies that the effects of probe pads, transitions and feed lines have been removed and TRL calibration is accurate. The insertion loss of thru (after TRL calibration) exceeds 0.05 at the edge of D-band around 165 GHz. This is most likely because the length of the line standard is very close to 180 degrees around that frequency. Due to this slightly higher error at the edge of D-band (~165 GHz), the extracted insertion loss for microstrip line is reported up to 165 GHz (instead of 170 GHz).

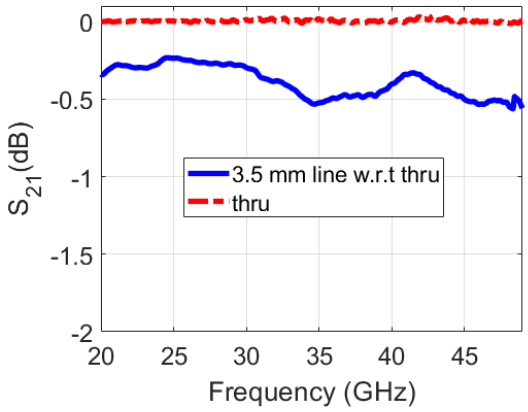

(a)

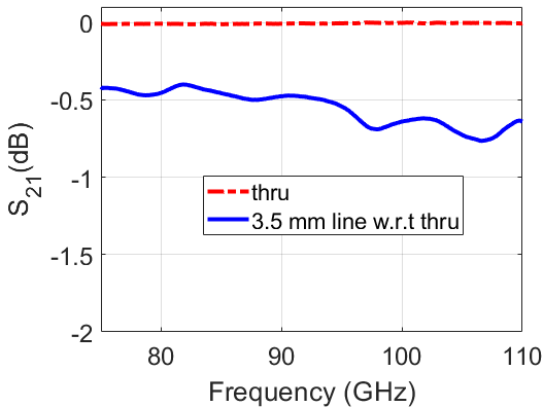

(b)

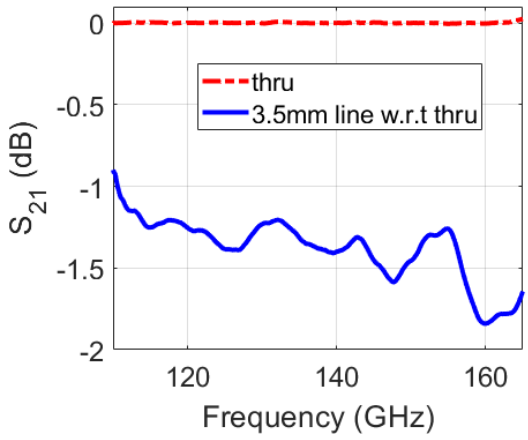

(c)

Figure 15 Extracted Insertion Loss of Microstrip Line after TRL Calibration and comparison with (a) Microstrip line from 20 GHz to 50 GHz (b) Microstrip line from 75 GHz to 110 GHz (c) Microstrip Line from 110 GHz to 165 GHz

2.5 Model to Hardware Correlation

The extracted dielectric constant and loss tangent data points were used to make frequency dependent substrate model in Ansys HFSS and models of CPW and microstrip lines were simulated. The goal of this task was to validate the extracted material properties by comparing the frequency dependent model-based simulations with the measurements. The magnitude (dB/mm) and phase (degree) for CPW and microstrip lines are given in Figure 16. The simulated models show a decent agreement with the measurements over a broad range of frequency from 20 GHz to 170 GHz.

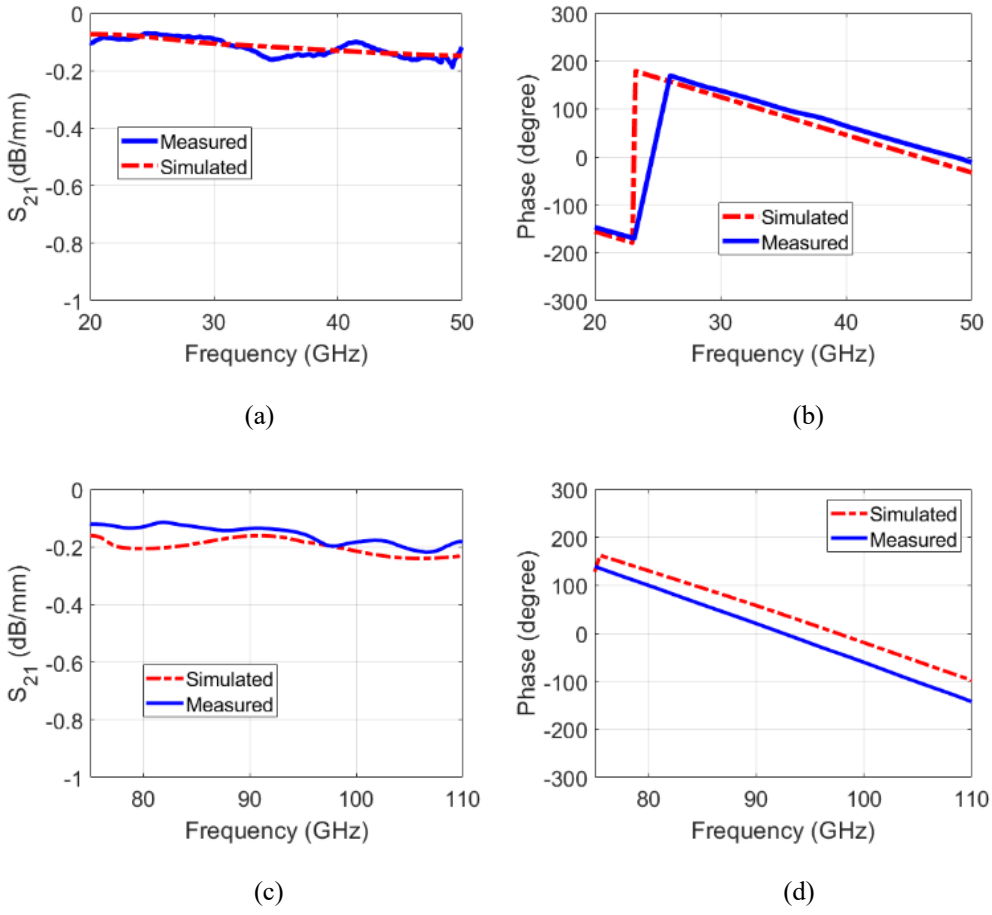

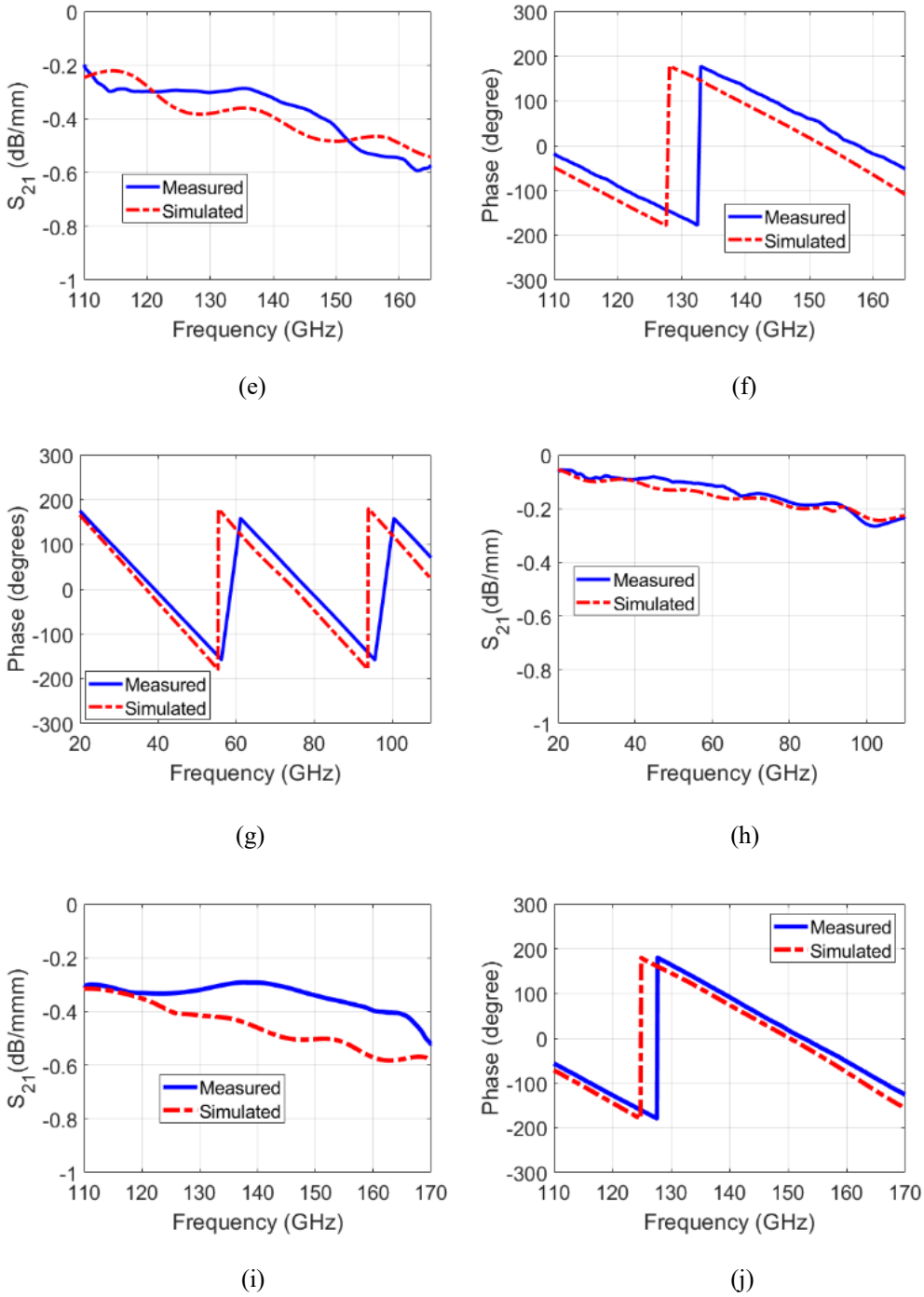

Figure 16 Model to Hardware Correlation of S21 (a) S21 (dB/mm) Microstrip Line 20 GHz to 50 GHz (b) Phase Microstrip Line 20 GHz to 50 GHz (c) S21 (dB/mm) Microstrip Line 75 GHz to 110 GHz (d) Phase Microstrip Line 75 GHz to 110 GHz (e)) S21 (dB/mm) Microstrip

2.6 Performance Comparison

The average insertion loss (dB/mm) of the interconnects designed on ABF/glass/ABF stack up was compared with other state of the art materials like Liquid Crystal Polymer (LCP) [22, 44], Astra, Teflon, and Rogers RF Duriod 6002 [45]. These materials have low loss properties and therefore are widely used for high frequency applications. The average insertion loss comparison is given in Figure 17. Glass based interconnects show very comparable performance as compared to the other candidates which shows that glass interposer technology is promising for supporting sub-THz modules.

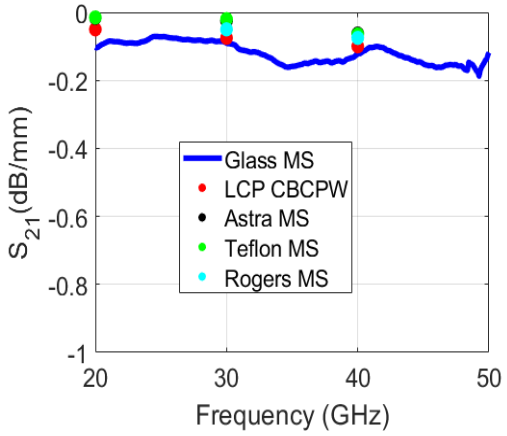

(a)

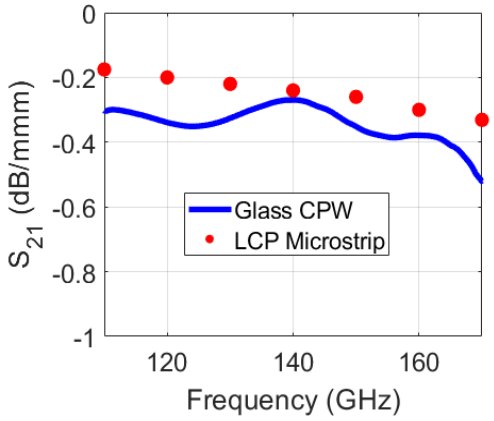

(b)

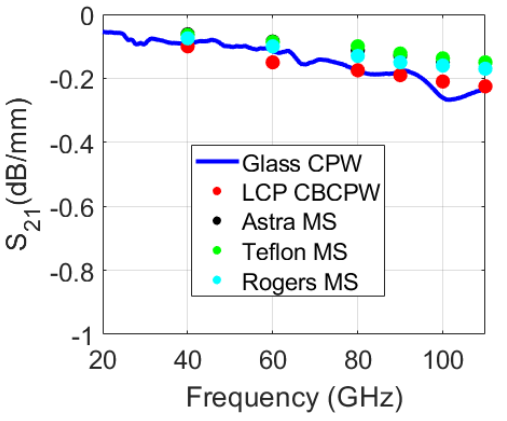

(c)

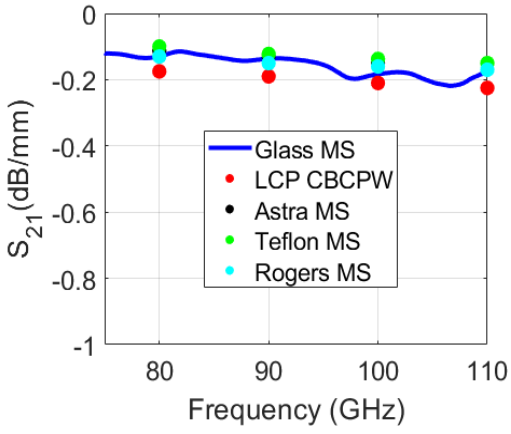

(b)

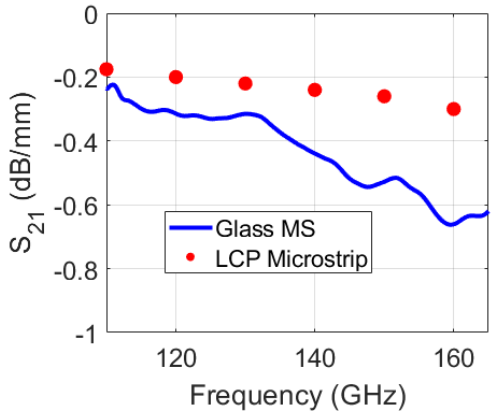

(e)

Figure 17 S_{21} Per Unit (dB/mm) of Glass based interconnects and comparison with the state-of-the-art materials (a)CPWs 20 to 110 GHz (b) CPWs 110 to 170 GHz (c) Microstrip Lines 20 to 50 GHz (d) Microstrip Lines 75 to 110 GHz (e) Microstrip Line 110 to 170 GHz

The insertion loss values at different frequencies with applications like 5G, WiGig, vehicular radar and 6G [46] are given in Table 5. Till 110 GHz, the glass-based interconnects have comparable performance as compared to the other materials. In D-band (110 GHz to 170 GHz), LCP provides a lower insertion loss for microstrip lines due to its low loss tangent, but glass interposers can support large packages with high I/O density because it can support fine dimensions (~1 µm). Glass based packages have superior dimensional stability and thermal reliability.

2.7 Industrial Utilization and Time to Market

The results show confidence that ABF/glass/ABF stack up while having good electrical performance like other low loss materials, can provide other module-level and system level benefits which are not possible otherwise [28]. However, since glass interposer technology is relatively new compared to the other candidates namely LTCC, organic substrates and

Silicon interposers therefore the adoption in industry is still in early stages. The adoption will significantly increase once the supply chain for glass and other required materials is set up to meet the market demand, necessary tools and manufacturing lines are readily available and manufacturing processes are standardized.

Table 5
Comparison of the performance (dB/mm) of glass-based transmission lines with other high frequency materials

	5G 28-40 GHz	WiGig 60 GHz	Vehicular Radar 77 GHz	Radar 94 GHz	6G 140 GHz
LCP	.05- 0.10	0.15	0.175	0.20	0.24
Astra	.016 - 0.06	0.085	0.1125	0.1375	NA
Teflon	0.015-0.06	0.0865	0.1	0.13	NA
Rogers	0.075 (40 GHz)	0.1	0.13	0.15	NA
Glass (this work)	0.075-0.095 (CPW) 0.1-0.1225 (microstrip)	0.12 (CPW)	0.17 (CPW) 0.13 (microstrip)	0.22 (CPW) 0.15 (microstrip)	0.25 (CPW) 0.45 (microstrip)

CHAPTER 3. SUBSTRATE INTEGRATED WAVEGUIDES

The use of carrier frequency mmWave frequency region poses unprecedented challenged for RF design. Interconnects with low loss, zero cross talk, high power handling capability and good broadband performance are required to support these mmWave modules. Traditional metallic waveguides can be used as ultra-low loss interconnects because they use air as a dielectric. They carry waveguides which can carry higher power as compared to TEM and quasi-TEM modes and due to their closed nature, they achieve zero cross talk. However, for consumer industry where form factor and cost are main drivers, metallic waveguides have limitations because they are bulky 3D structures which are costly to machine and difficult to integrate with other planar technologies like microstrip and CPW. Microstrips and CPWs are low profile but they have low Q mainly due to the radiation losses as these structures are not closed. Substrate Integrated Waveguide (SIW) technology [47] bridges the gap between the traditional waveguides and planar technologies like CPWs and microstrip lines as it preserves the advantages of bulky waveguides in a low-profile form factor that is easy to integrate.

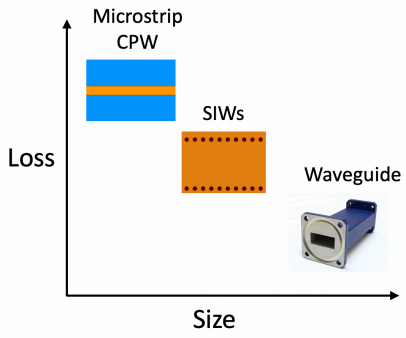

Figure 18 Loss-size for different interconnects

On the loss-size graph, SIWs are in between the traditional waveguides and planar structures as shown in Figure 18. Due to closed transmission, SIWs have significantly lower coupling if the vias are closely placed in the side walls obeying the design rules presented in [48]. Microstrip lines are typically smaller in width but unlike SIWs microstrip lines have a greater coupling and hence to get decent isolation, they need to be separated by a large distance. This makes SIWs promising for to achieve low cross talk in a compact manner even though they are wider in size. For example, in 3mm width, SIWs have 2X less cross talk as compared to microstrip line pair. This makes a case for SIWs for dense signal routing with low cross talk.

Since SIWs emulate a rectangular waveguide, they have high power handling capability. The frequency-dependent average high power handling capability (AHPC) of SIWs was studied in detail in [49]. AHPC of an SIW depends on various factors like ohmic attenuation, dielectric attenuation, cross section of the waveguide, ambient temperature and glass transition temperature of the materials used. AHPC of SIWs can be computed by using a set of heat transfer analysis-based equations presented in [49].

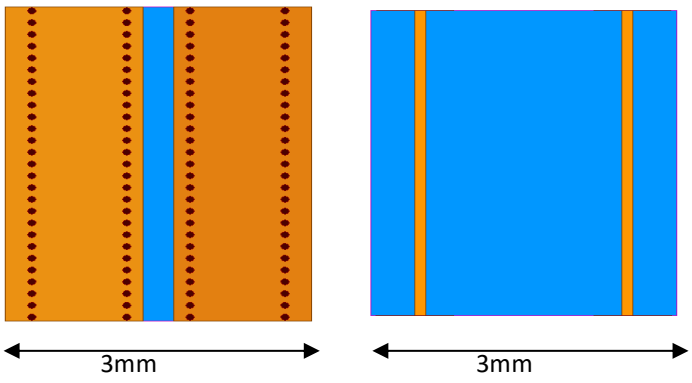

(a)

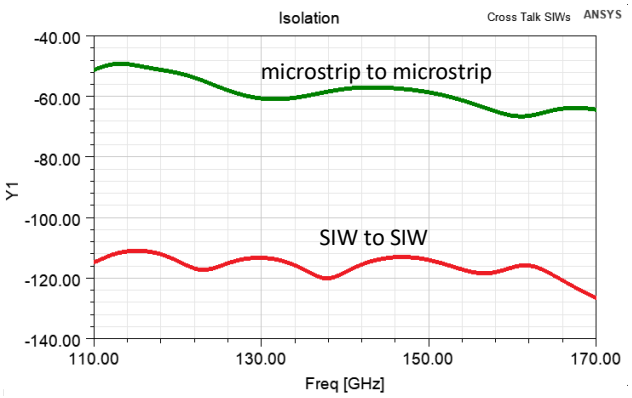

(b)

Figure 19 Cross talk study (a) structures (b) isolation (dB)

3.1 Brief literature review of SIWs above 100 GHz

Owing to the merits of SIW technology, SIWs have been demonstrated using different substrate and fabrication technologies for frequencies above 100 GHz. Organic substrates like LCP were used to develop SIWs up to 170 GHz. It was observed that despite the low loss tangent of LCP, LCP based SIWs shows insertion loss up to 0.85 dB/mm due to large surface roughness of the material. It has been reported in [24] that insertion loss can be improved by using an additional surface polishing process. High resistivity Silicon-based SIWs have been presented in [50]. This material is attractive for the development of SIWs because of its compatibility with the CMOS process and its use in Silicon Interposers but its cost due to the use of expensive materials and wafer scale processes make it less desirable. High resistivity Silicon-based SIWs show insertion loss of 0.55 dB/mm to 0.7 dB/mm in D-band. Recently, Silicon Carbide (SiC) has also been used to develop low loss SIWs above 100 GHz [51]. SiC based SIWs show an excellent insertion of 0.22 dB/mm in D-band but high cost and extremely challenging fabrication process owing to the hardness of the materials makes the application of this solution very limited.

To overcome the limitations of the existing packaging technologies, glass interposers have gained a lot of attention because of their unique ability to support ultra-fine pitches at low cost with decent electrical performance. The potential of glass interposer technology to support mmWave modules and the merits of SIW technology motivate the development of SIWs in D-band using glass interposer technology. The design, fabrication and measurements for glass based SIWs [52] will be presented in the proceeding sub-section.

3.2 SIWs in Glass Interposer Technology

SIWs were designed, fabricated, and measured using ABF/glass/ABF material stack up.

The design details are described below:

3.2.1 Design Details

SIW emulates a rectangular waveguide by enclosing substrate between two metal layers connected by two rows of via side walls. This geometry can support transverse electric (TE) modes. For the cut off frequency (f_c) for the fundamental mode (TE_{10}), the width of the SIW is equal to one half of the guided wavelength corresponding to the cut off frequency. The bandwidth of operation for the fundamental mode is from $1.25f_c$ to $1.89f_c$.. Ansys HFSS was used to design the SIWs. The material stack up was modelled by using the frequency dependent electric properties extracted in the previous chapter.

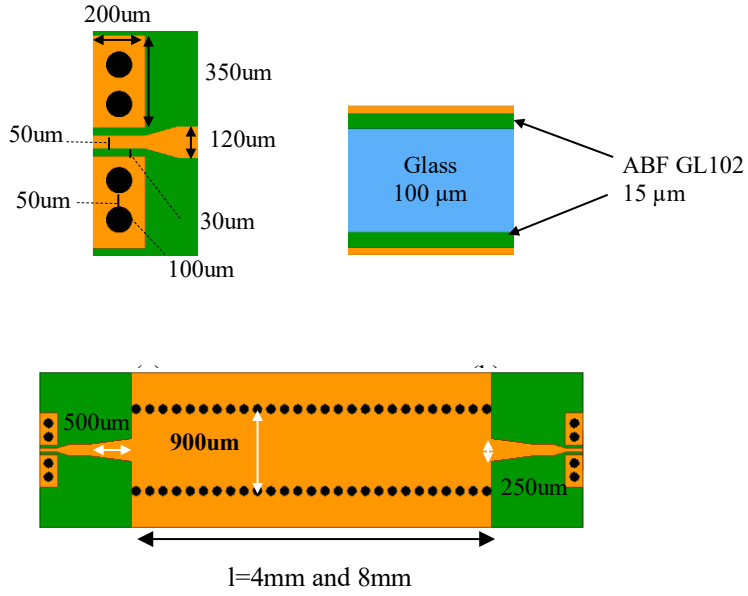

(c)

Figure 20 Design of glass based SIWs (a) CBCPW to microstrip transition (b) material stack up (c) SIW with microstrip taper transitions and CBPW probe pads

The width of the SIWs was designed to be 900 µm to keep the cut off frequency at 80 GHz. The diameter and pitch were 100 µm and 150 µm respectively. These values obey the design rules presented in [48] to have negligible radiation loss through the via sidewall of the SIW. Since the designed SIWs were to be probed used RF GSG cables, CBCPW to microstrip transitions were added. SIWs with two different lengths (4mm and 8mm) were designed so that insertion of the SIW section can be extracted by eliminating the effects of CBCPW probe pads, CBCPW to microstrip transition, microstrip feed lines and microstrip taper. The material stack-up and design are given in Figure 20.

3.3 Fabrication

Since this test vehicle had Thru Glass Vias (TGVs), the designs of panels with TGVs were sent to Asahi Glass Company (AGC) and TGVs were drilled by AGC. Bare glass panels were treated with Oxygen Plasma for 5 mins, followed by Silane treatment for 20 mins at 70º C. Then 15 µm thick ABF GL 102 dry film was vacuum laminated on both sides of the glass substrate using Meiki Laminator. Then the laminated panel was cured at high temperatures (30 mins at 130˚C and 30 mins at 170˚C). During the curing stage, the polymer flows, and TGVs get filled with the polymer. Then via-in-via were drilled using Cornerstone Laser Tool. The copper was patterned using Semi-Additive Process (SAP). 0.3 µm thick Cu seed layer was deposited using electroless copper deposition. Next, 15 µm thick dry film photoresist (Hitachi RY5115) was vacuum laminated and exposed using mask aligner. Then Cu was plated up to 7 µm and at last, the seed layer was etched using differential etcher. The process flow is given in Figure 21.

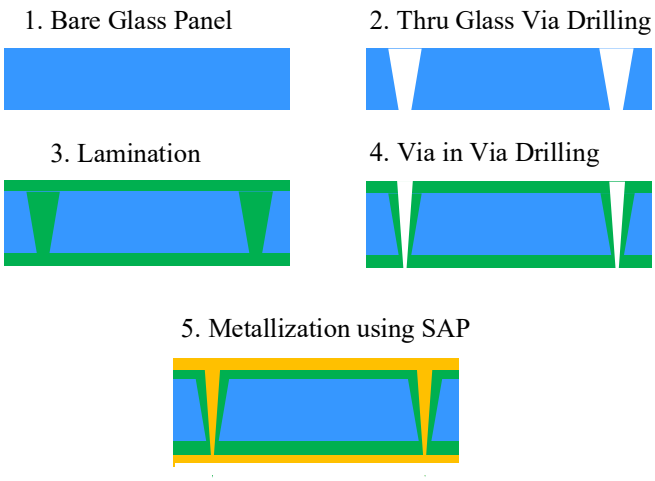

Figure 21 Process flow for fabrication

The fabricated samples were examined under Zeta Optical Profilometer. There was ~4 to 5 µm difference in designed and fabricated structures. This can be attributed to various factors like exposure time in lithography, photoresist development rate and time in differential etcher which are difficult to precisely control. In this test vehicle, the structure of interest was SIW section, and it was not affected by this slight change in fabricated lines and spaces. The fabricated dimensions were used in simulation models to account for any changes caused. The fabricated samples are shown in Figure 22.

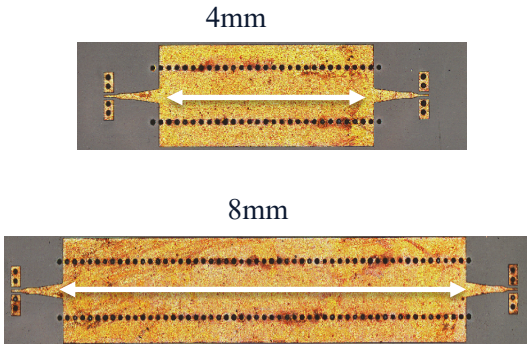

Figure 22 Fabricated SIW samples

3.4 Measurements

The scattering parameters of the fabricated SIWs were measured in D-band using Keysight VNA (E8361C) along with millimeter wave controller and frequency extenders (V06VNA2). Cascade Infinity probes 170-S-GSG-75-BT (75µm pitch) were used to probe the samples. LRRM calibration was performed using Cascade Wincal software and calibration substrate to move the reference plane to the edge of the probe tips. The simulated and measured scattering parameters for 4mm and 8mm long SIWs with transitions and feed lines are given in Figure 23a and Figure 23b. The simulated and measured results have decent agreement.

To extract the loss of SIW section, the measurements of 8mm and 4mm long structures were subtracted. The extracted loss of SIW section (dB/mm) is given in Figure 23c. The performance (dB/mm) of the glass interposer based SIW was compared with SIWs fabricated in LCP and Silicon interposers (high resistivity Silicon). The performance comparison is given in Figure 23c.

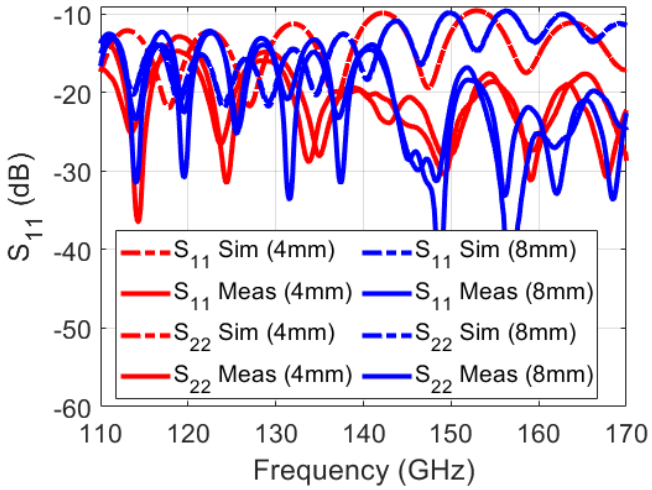

(a)

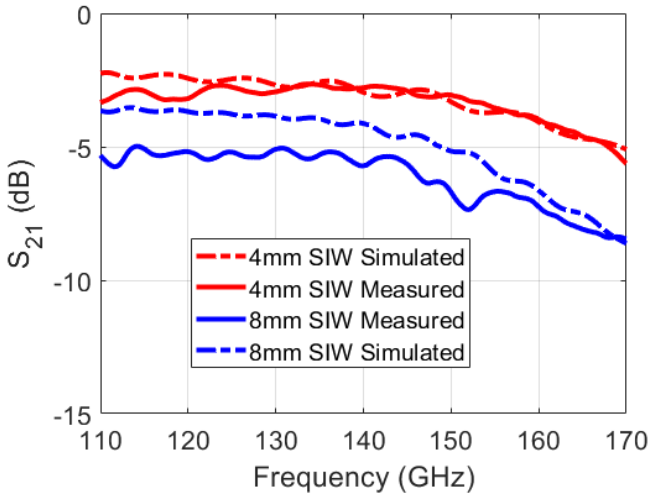

(b)

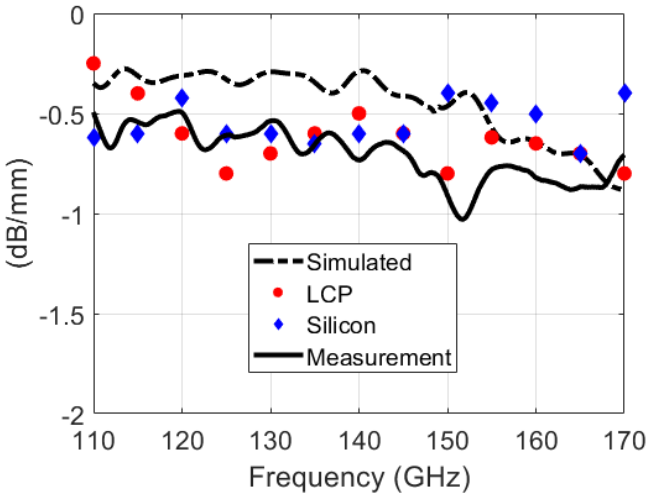

(c)

Figure 23 Measured and Simulated Results of the Glass Based SIWs (a) S11(dB) (b) S21 (dB) (c) S21 (dB/mm) with performance of SIWs on other substrates

The measured insertion loss of glass based SIW varies from 0.5 dB/mm to 1.0 dB/mm in entire D-band. The insertion loss values are 0.5 dB/mm and 0.72 dB/mm at 110 GHz and 170 GHz respectively. The average insertion loss in D-band is 0.7 dB/mm. For most of the frequencies in D-band, the insertion loss varies from 0.5 dB/mm to 0.8 dB/mm except for a narrow band around 150 GHz. Simulated and measured insertion loss follow a similar trend. There is a 0.25dB/mm difference between the simulated and measured response. In the simulations, the effect of surface roughness was not included. The surface roughness was measured using Zeta Optical Profilometer. On different samples, the measured rms surface roughness value ranged between 180 nm to 250 nm. The correlation can be improved including surface roughness in simulations. The results show that glass interposer based SIWs show good electrical performance which gives confidence that glass interposer technology is a suitable candidate to support mmWave modules.

CHAPTER 4. SUBSTRATE INTEGRATED WAVEGUIDE FILTERS

5G utilized carrier frequencies from untapped mmWave region (28 GHz and 39 GHz) to solve the capacity issues of previous generation networks by using wide physical bandwidth. Following this trend, in future numerous wireless applications like 6G, automotive radars, WiGig etc will use carrier frequencies from mmWave region which will crowd the spectrum. This will pose a challenge for the development of mmWave filters to enable channel selection and out of band rejection. As discussed in the previous chapter, SIW technology will play a crucial role in the development of sub-THz modules due to its ability to support low loss interconnects with zero cross talk, high power handling capability and compatibility with other planar technologies and fabrication processes. A detailed review of SIW based filters is described in [53-55] The electrical performance of D-band SIWs in glass interposer technology was described in the previous chapter. The merits of SIW technology and its good performance in glass interposers motivate the development of other SIW based passive devices ABF/glass/ABF stack up. In this chapter, design, fabrication, and measurements for glass based SIW cavity filters will be presented [56].

4.1 Design Details

ABF/glass/ABF material stack up was used to design SIW filters. Glass and ABF was modelled by using frequency dependent substrate model as described in Chapter 2.

Bandpass filters were designed by directly coupling resonant cavities by inductive iris. The frequency response of a resonant cavity is function of its geometry. To demonstrate different frequency responses, two different shapes of resonant cavities were designed namely square and rectangle. The difference in the frequency response will be discussed later with the measurement results. The initial dimensions of the cavity can be calculated by using the equation below

$$f_{101} = \frac{c}{2\pi\sqrt{\varepsilon_r}}\sqrt{\left(\frac{\pi}{w_{eff}}\right)^2 + \left(\frac{\pi}{l_{eff}}\right)^2} \quad (16)$$

where ε_r is the dielectric constant of the material stack up, f_{101} is the resonant frequency for the dominant mode TE_{101} and w_{eff} and l_{eff} are the effective width and length of the SIW cavity respectively. The relationship between physical and effective dimensions of an SIW (length and width) is described in [57].

For this test vehicle, the target resonant frequency was set to 130 GHz. For square shaped cavity, length and width were kept equal. For rectangular cavity, effective width was put 1mm and effective length was calculated. The diameter and pitch were designed to be 70 μm and 170 μm respectively. These values obey the design guidelines given in [48] for negligible loss radiation loss. After calculating initial dimensions, simulation models were built in HFSS, and dimensions were tuned to set the resonant frequency at 130 GHz. The cavities were fed using center coupled microstrip lines.

The width and the length of the coupling slot were designed using Ansys HFSS. The simulated s-parameters for different coupling slots are given in Figure 24. First, the effect of coupling width (ws) was investigated by simulating three different models with 25 μm, 50 μm and 75 μm wide coupling slot. Decreasing the coupling width increases the

rejections in stop band at the expense of slightly higher passband insertion loss. After observing the results, 30 µm wide coupling slot was used in this design to have a tradeoff between passband insertion loss and stop band rejection.

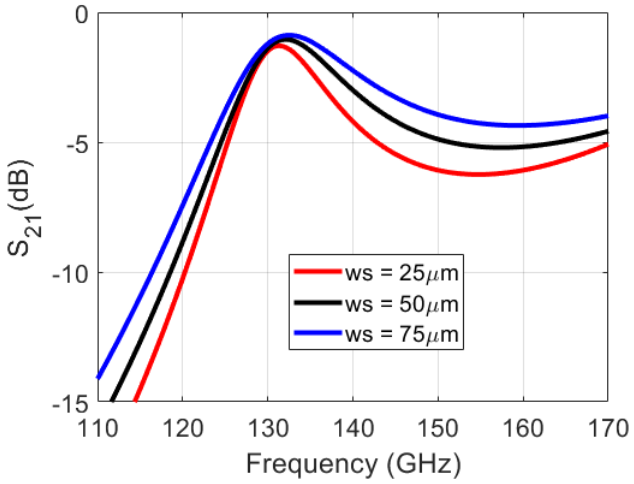

(a)

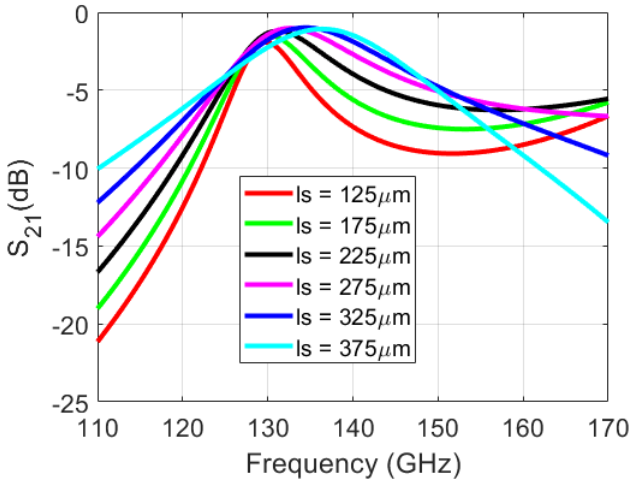

(b)

Figure 24 Coupling slot design (a) varying slot width (ws) with a fixed ls=225 µm (b) varying slot length (ls) with a fixed ws=35 µm

Then the effect of the slot length (sl) was investigated by simulating different cases with 125 µm, 175 µm, 225 µm, 275 µm, 325 µm and 375 µm long coupling slots. Increasing

the coupling slot length decreases the lower stop band rejection and pass band insertion loss. From 125 µm to 225 µm, increasing the slot length decreases the higher stop band rejection and then from 275 µm to 375 µm, increasing the slot length increases the higher stop band rejection. There is a tradeoff between lower stop band rejection, passband insertion loss and higher stop band rejection. To have a reasonable insertion loss and rejection in both stop bands, coupling slot ~250 µm can be used.

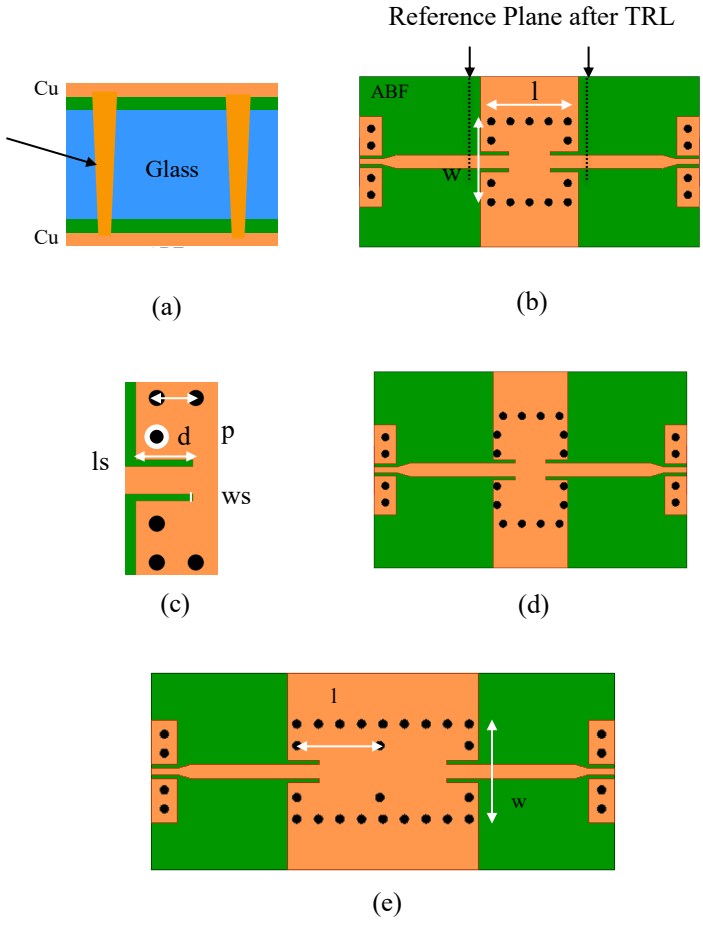

Figure 25 SIW filter test vehicle (a) material stack up (b)first order square filter (c)coupling slot (d) first order rectangular filter (e) second order square filter

4.2 Fabrication

As described in previous test vehicles, the designed filters were probed using RF GSG probes so CBCPW to microstrip transitions were added. TRLs were designed to de-embed the loss of the filter. The reference plane after TRL calibration is shown in Figure 25b. It is important to note that the measurements after TRL calibration included the effects of microstrip coupling slots. To exclude the loss from the microstrip coupling slots, reference plane can be moved after the microstrip coupling slots as described in [53].

The designed SIW filters were fabricated using the process flow described in Figure 21. However, in this fabrication due to the unavailability of the Cornerstone Laser Tool, via-in-via were drilled using Optec Femtosecond Laser Tool. Experiments were done to determine optimal process conditions for drilling vias in Femtosecond laser tool by varying different parameters like laser power, frequency, laser speed, jump speed and burst time. Initially, the target via diameter was 100 µm. A single punch drill with 0.6W power (15% on femtosecond), 12 kHz frequency and 50mm/sec laser speed resulted in a diameter of 80 µm with ~16 µm depth. This was used a starting point and multiple drills (~8) were done drill through entire 130 µm thick stack up. The measured diameter at the top side of the stack up was 95 µm which was very close to the target (100 µm) but this approach gave highly tapered vias with only 37 µm bottom diameter. This taper profile was not suitable for designing SIWs because it can cause radiation leakage. To correct this, a new approach was tried in which half of the drills were done from the top side and then the panel was flipped upside down and the remaining drills were done. This approach resulted in an additional alignment step but the via profile was corrected and the diameter at both sides was ~95 µm. Later, the target diameter was changed to 70 µm to relax the requirement for

alignment because of the offset in the panel scale mode in Femtosecond Laser tool. Once the vias were drilled, rest of the other processing steps were same as described in section 3.3.

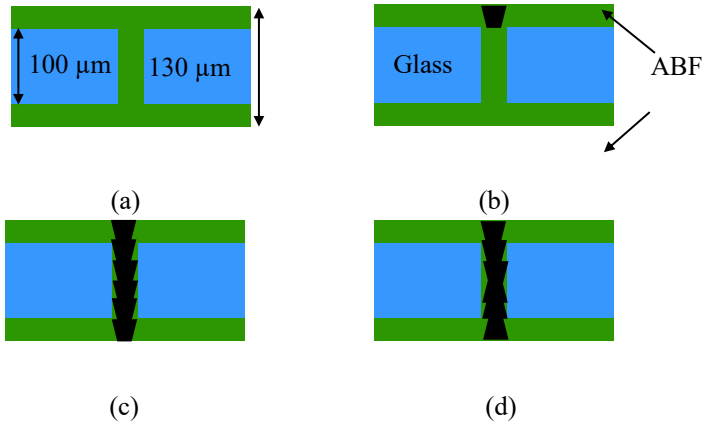

Figure 26 Via drilling process optimization (a) stack up (b) single drill (c) top side drill (d) both side drill

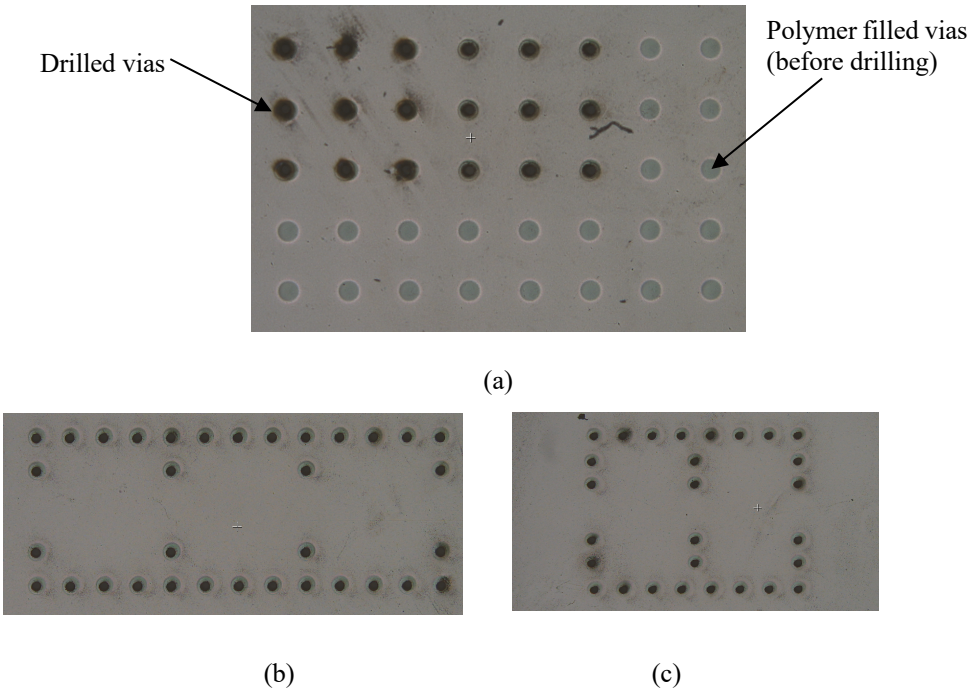

Figure 27 Samples with drilled vias (a) optimization grid (b) third order square filter (c) second order rectangular filter

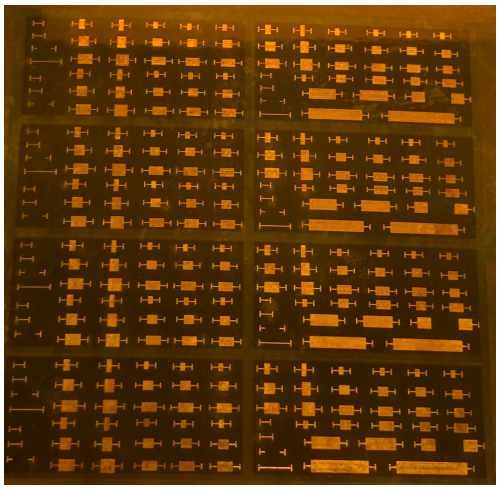

(a)

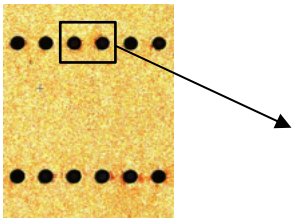

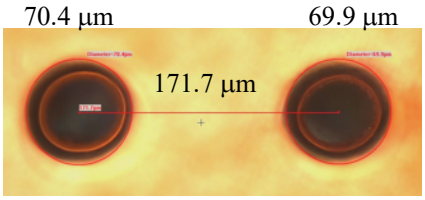

(b)

(c)

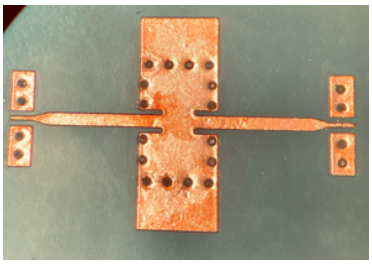

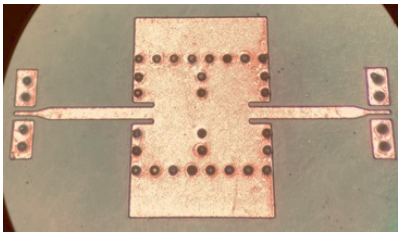

(d)

(e)

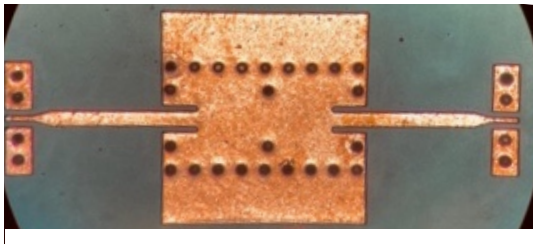

(f)

Figure 28 Fabricated samples (a) panel (b) via side wall (c) diameter pitch measurement (d) first order rectangular filter (e) second order rectangular filter (f) second order square filter

The fabricated samples are given in Figure 28. The fabricated dimensions were measured using Zeta Optical Profiler. The designed and fabricated dimensions along with the percentage change are given in the table below. There was ~7 μm change in designed and fabricated line dimensions. This can be attributed to several factors like exposure time in lithography, photoresist development rate and etching rate in differential etcher which are difficult to precisely control. The fabricated dimensions were used in the post fabrication simulation models to get better model to hardware correlation.

Table 6 Physical dimensions for SIW filters

Parameter	Symbol	Designed (μm)	Fabricated (μm)	Change (%)
Square cavity dimensions	l	700	710	1.4
	w	700	710	1.4
Rectangle cavity dimensions	l	600	608	1.3
	w	1000	1012	1.2
Via pitch	p	170	172	1.2
Via diameter	d	70	70.5	0.7
Coupling slot length	ls	225	232	3
Coupling slot width	ws	30	33.5	11.6
Microstrip line width	wms	120	113	5.8

4.3 Measurements

The scattering parameters of the designed filters were measured using Agilent vector network analyzer (E8361C). The frequency range of the VNA was extended to D-band (110 GHz to 170 GHz) by using D-band extenders (V06VNA2) and mmWave controller. Samples were probed using Cascade infinity probes 170-S-GSG-75-BT (75μm pitch). Two tier calibration was used to measure the samples. First, LRRM calibration was used to move the reference plane to the edge of the probe tips using Wincal software by Cascade and calibration substrate. Then TRL calibration was used to remove the losses due to CBCPW to microstrip transitions and feed lines. The reference plane after TRL calibration is given in Figure 25b.

The simulated and measured scattering parameters in D-band are given in Figure 29. First, second and third order square filters show insertion loss of 1.54 dB, 2.7 dB and 4.2 dB respectively. The first and second order rectangular filters show 1.65 dB and 2.85 dB insertion loss at ~130 GHz. The relative bandwidth for the designed filters is given in Table 7. The frequency response of different cavity shapes (square and rectangle) is compared in Figure 29e. Rectangle shaped filters show better rejection in the higher stop band compared to square shaped filters. This effect is due to the different shape of the cavity because for square shaped cavity, the cut off for higher order modes are relatively closer to the center frequency as compared to rectangle shaped cavity. Due to this reason, rectangular cavities perform better in rejecting higher frequencies. However, for a same order, rectangular filters are 20% larger in size compared to square filters. These results show that SIW filters provide flexibility to achieve different filter responses by changing the shape of the filter.

The insertion loss and bandwidth of the glass based SIW filters is compared with state-of-the-art mmWave SIW filters in Table 7. It is important to note that the filters in listed in Table 7 have different orders, different substrate heights and feeding mechanisms which makes direct insertion loss comparison difficult. However, results show that the glass based SIW filters have comparable electrical performance to the other candidates while providing additional module level and system level benefits like supporting ultra-fine pitch on panel scale at low cost which are not possible otherwise.

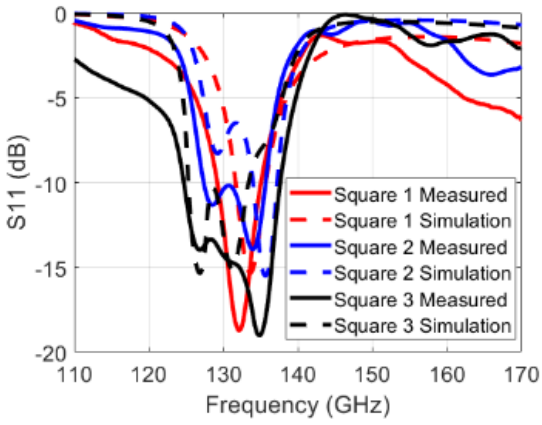

(a)

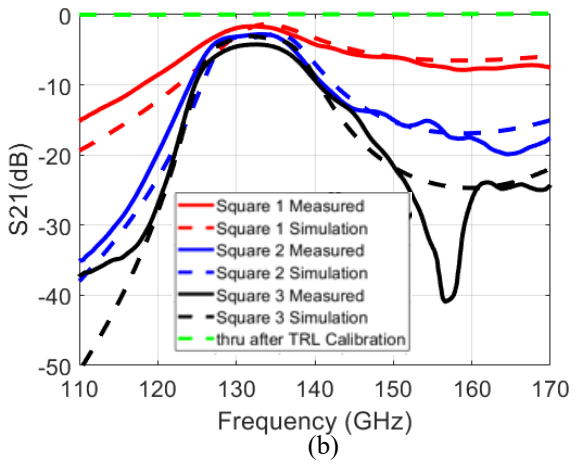

(b)

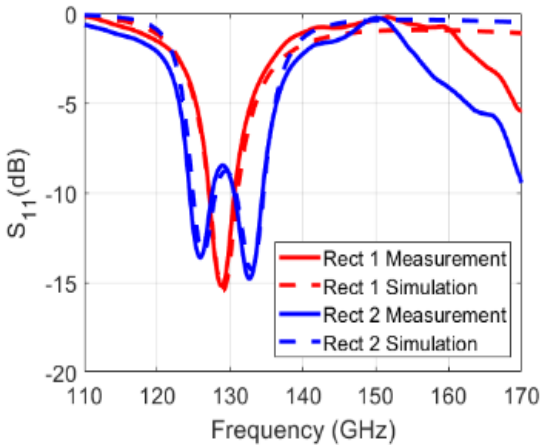

(c)

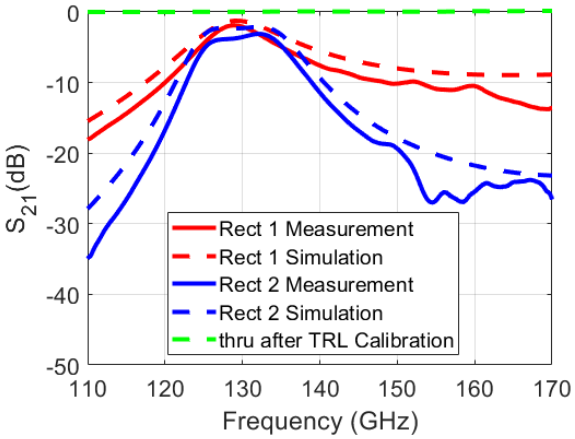

(d)

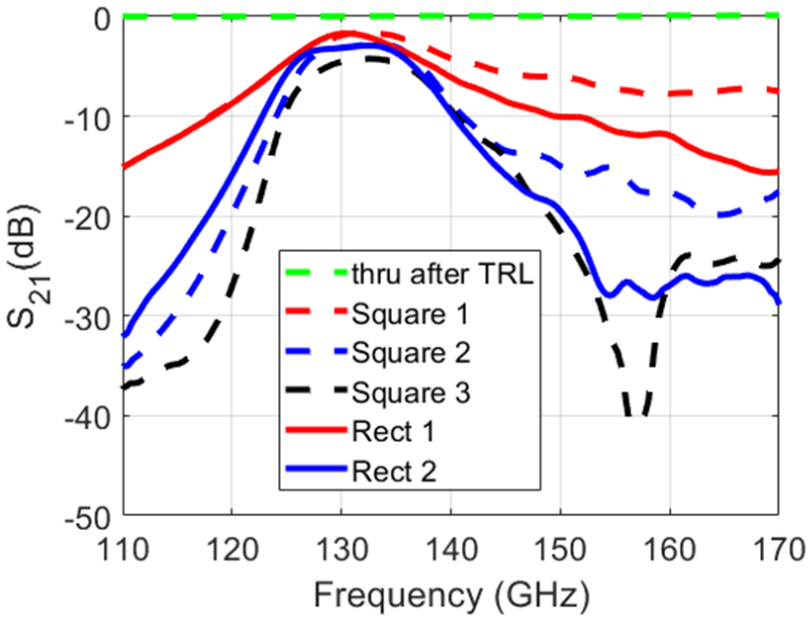

(e)

Figure 29 Measurements and simulated scattering parameters for post fabrication models of SIW filters (a) S11 for square filters (b) S21 for square filters (c) S11 for rectangular filters (d) S21 for rectangular filters (e) S21 for both square and rectangular filters

Table 7 Insertion loss and bandwidth comparison for mmWave SIW filters

Ref.	Material	Order	IL (dB)	Freq (GHz) f_0	BW (%)	size(λ_0 x λ_0) $\lambda_0=c/f_0$
[58]	LCP	2	2.6	94	8	.63 x .57
[59]	High R Si	4	3.9	140	10	NR
[60]	LTCC	3	1.913	140	13.0	.38 x .57
[61]	Thick film	4	3.33	94	7.3	.28 x .8
		4	3.86	150	8	NR
[62]	BCB (simulated)	3	1.5	159.7	12.5	.45 x 1.2
This Work	ABF/ glass/ ABF	1	1.54 Square	130.5	12.8	.31 x .31
		1	1.65 Rect	130.5	9.8	.44 x .26
		2	2.7 Square	131.2	9	.31 x .62
		2	2.85 Rect	131.2	9.5	.44 x .52
		3	4.2 Square	132.4	8.8	.31 x .93

4.4 Role of Material Properties and Via Diameter in SIW cavity filters

The SIW filter test vehicle was designed and fabricated twice. The results presented in this chapter are from the second build. This sub-section will document the results obtained and lessons learnt from the first build. The first build of SIW resonator filters were completed using the SIW fabrication process described in sub-section 4.2. After measurements, it was observed that the center frequency of the filters was shifted by a few GHz (~18 GHz). The

target design frequency was 140 GHz, but the measured filters resonated at ~122 GHz. This trend was consistent in all measurements. This can be explained based on two factors, 1) the extracted material properties of ABF/glass/ABF material stack up were not available during the design of the first test vehicle. Therefore, dielectric constant of the materials (ABF and glass) was modelled by the data sheet values which were available at low frequencies. Later, it was found that the measured values were slightly higher (~10%) than the modelled values. This contributed to shifting the resonant frequency to the lower side. In addition, as discussed in the fabrication section, the via diameter was decreased from 100 µm to 70 µm due to challenges in alignment during via drilling using the panel scale mode (IFOV) in the Femtosecond Laser Tool. This effect was not included in the simulations in the first build as the filters were designed prior to the process development for drilling vias.

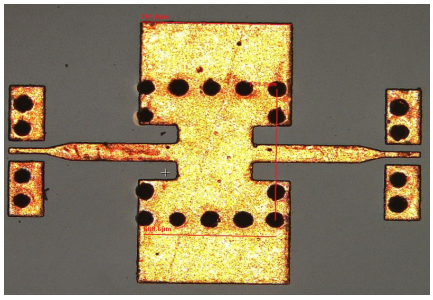

(a)

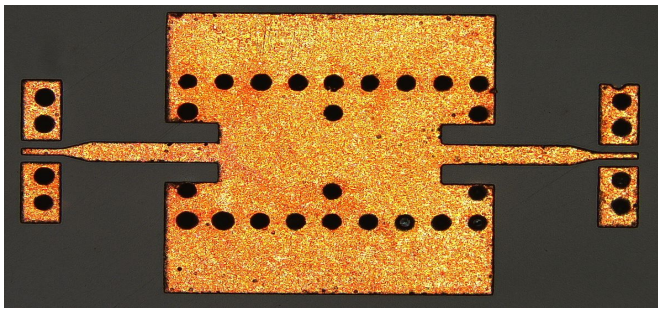

(b)

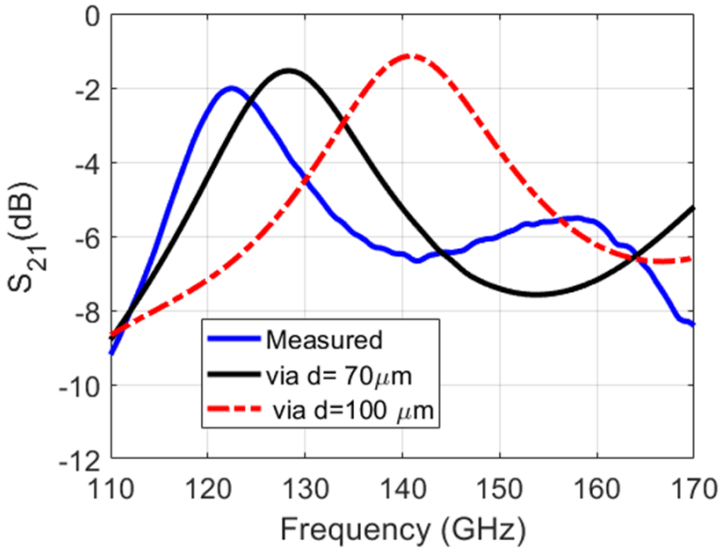

(c)

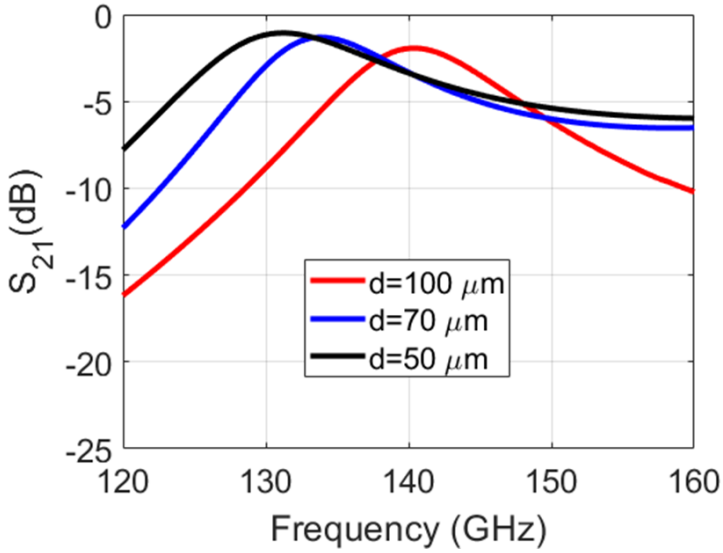

(d)

Figure 30 Results from first SIW filter TV (a) fabricated first order filter (b) fabricated second order filter (c) simulated and measured S21 (dB) (d) effect of changing via diameter from 100 µm to 50 µm

The fabricated samples and simulated and measured S_{21} (dB) for the first order SIW filter are given in Figure 30. It can be seen in Figure 30b that there is ~18 GHz difference in the

designed and measured resonant frequency for the first order SIW filter. To understand the effect of changing via diameter, simulations were performed using Ansys HFSS for different via diameters. Three cases with 100 μm, 70 μm and 50 μm diameter vias were simulated. The results are given in Figure 30d. The simulation results shown that decreasing the via diameter significantly decreases the resonant frequency of the filter. Smaller via diameter results in a larger sized cavity hence the resonant frequency shifts to the lower side. By incorporating the effect of smaller vias in the post fabrication simulation model the center frequency shift was explained and there were two key takeaways which were used in the next build to get the desired results i.e., 1) use extracted material properties for ABF/glass/ABF material stack-up in HFSS using frequency dependent substrate model 2) precisely control the diameter of the vias in fabrication to avoid large shifts in resonant frequency.

CHAPTER 5. NOVEL BLIND VIA FILTERS

The good electrical performance of SIW technology in glass interposers for frequencies up to 170 GHz demonstrates its suitability for the development of sub-THz modules. But, in consumer industry, footprint is also a key metric along with performance and cost. One well documented disadvantage of SIWs is their large size as compared to the other planar technologies which can limit their application. To address this limitation, half mode [63] and quarter mode SIW [64] topologies have been designed which take advantage of the magnetic symmetry in SIW to reduce the lateral dimensions, but the longitudinal dimensions remain unchanged.

To reduce both the physical dimensions of transmission lines, slow wave propagation was first introduced in [65]. Slow wave phenomenon was used to demonstrate miniaturized microstrip lines [66] and CPWs [67, 68] . Using the same principle, lateral and longitudinal dimensions of an SIW, several rows of blind vias can be used in a multilayer stack up to produce slow wave propagation by physically separating electric and magnetic fields. Using this principle, Slow Wave SIWs were presented in which both lateral and longitudinal dimension were reduced by 40% [69]. This technique was used to design a miniaturized SIW cavity filter at 11 GHz with 70% area reduction [70].

The low loss, zero cross talk, high power handling capability and potential for miniaturization makes SIW technology promising for making filters for mmWave frequency region. A detailed review of existing designs and techniques for making SIW filters have been discussed in detail in [53-55]. Since SIW is a planar form of rectangular waveguide, design procedures for rectangular waveguide-based components can be applied

to the SIW technology. In waveguides, filter response can be generated by using obstacles or discontinuities like irises, coupling apertures and gaps etc. [71]. Characteristics of single and multi-iris resonant structures placed in a rectangular waveguide were experimentally studied in. The behavior of different obstacles in a waveguide section has been discussed in. An obstacle that restricts the width of the waveguide behaves as a shunt inductance whereas an obstacle which restricts the height of the waveguide behaves as a shunt capacitance. The solution for a single post inductive obstacle in a rectangular waveguide is given in[72, 73]. A capacitive obstacle based waveguide filter is designed in [74]. A combination of both obstacles can be used to create a resonant obstacle in a waveguide. Detailed analysis and demonstration of an SIW filter with L-shaped resonant iris has been presented in [75].

Using resonant iris in a SIW section presents a promising opportunity to realize filters with interesting properties for mmWave frequency region. In this chapter, we present a new structure for making miniaturized SIW filters which uses a single blind via as a resonant obstacle in an SIW section to create a first order filter response.

5.1 First design

5.1.1 Material stack-up

Initially, the blind via filters were designed based on the same material stack up used to design SIW interconnects and resonator filters in Chapter 3 and Chapter 4 respectively. In addition to thru vias as used in Chapter 3 and Chapter 4 to make via side walls for SIWs, this test vehicle included blind vias to make miniaturized SIW filters. The material stack-up along with both types of vias (thru via and blind via) is shown in Figure 31.

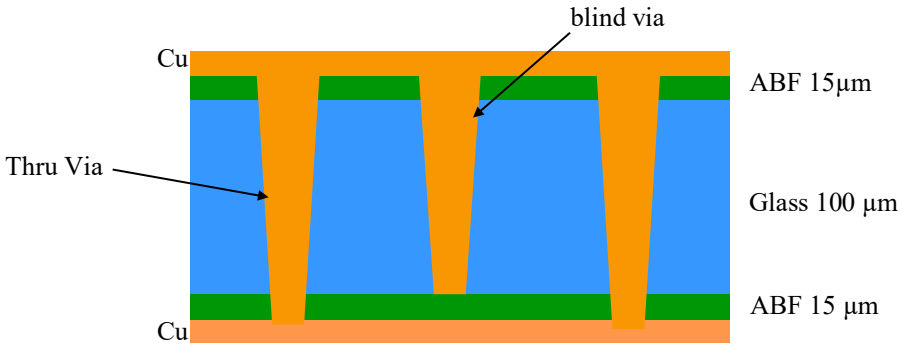

Figure 31 Material stack-up for making blind via SIW filters

5.1.2 Structure design

A filter response was designed by placing two blind vias in center of a SIW-section. The response of the filter can be tuned by using three parameters i.e the pitch of the blind vias, length (l) of the SIW section and distance (y) of the blind via from the via side wall. The structure of the filter and physical parameters are shown in Figure 32.

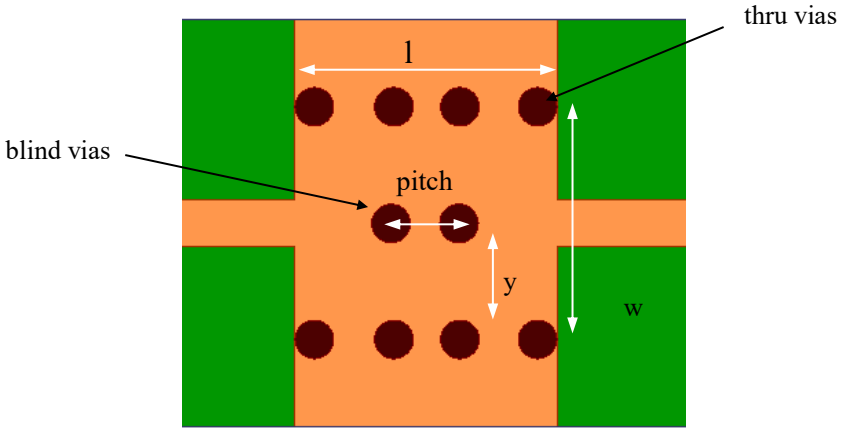

Figure 32 First order blind via filter with physical parameters

5.1.3 Response tuning

Ansys HFSS was used to simulate the filter responses for different physical parameters. The center frequency of the filter can be tuned by changing the pitch of the blind vias. The responses for first order blind via filters operating at different center frequencies are given in Figure 33a. Changing the pitch of the blind vias from 40 µm to 120µm in an SIW section with 650 µm width (w) and 675 µm length (l) changes the center frequency from ~130 GHz to ~140 GHz. This implies that the blind via filter structure is flexible for designing filters operating at different frequencies.

The E-field plots at 110 GHz, 140 GHz, and 170 GHz for the first order blind via filter with 140 GHz center frequency are given in Figure 33b.

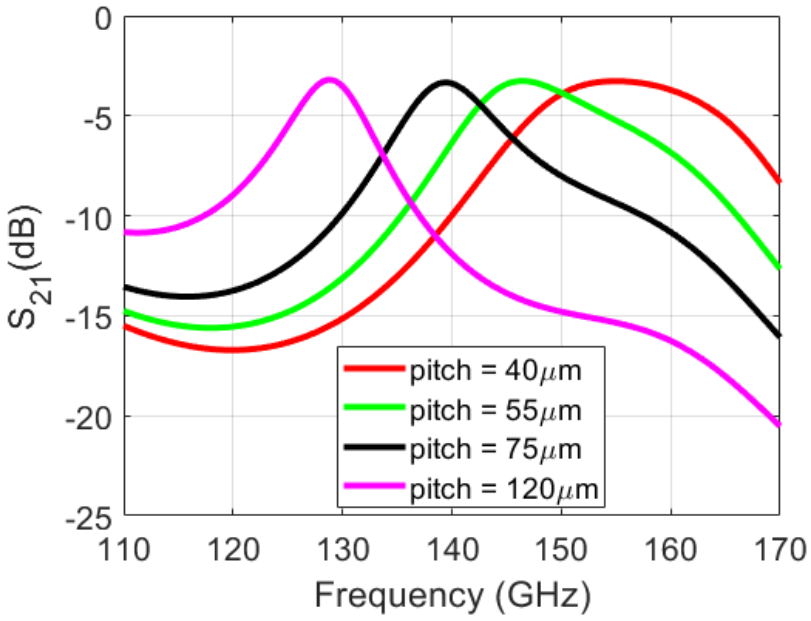

(a)

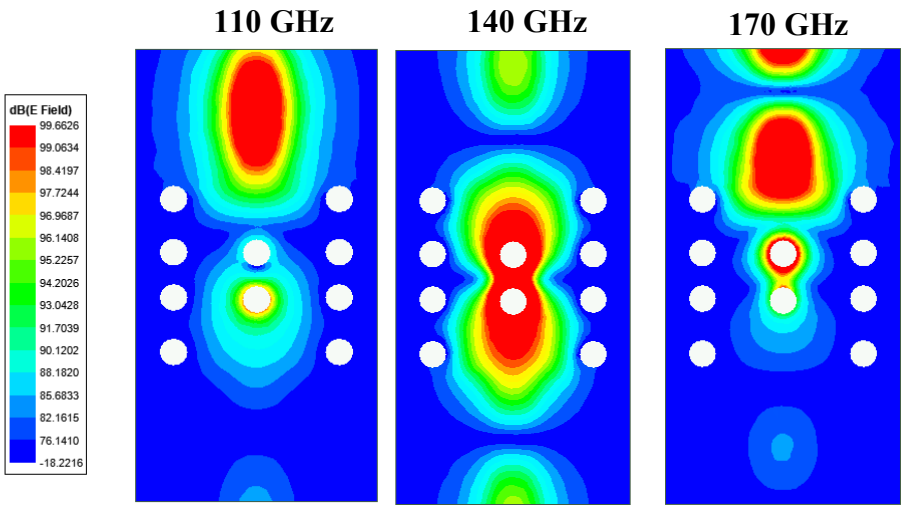

(b)

Figure 33 Blind Via Filter simulation (a) center frequency tuning using pitch (b) E-field at 110 GHz, 140 GHz, and 170 GHz

After designing the center frequency of the blind via filter, the physical parameters (length) and via placement (y) can be used to tune the rejection of the filter in lower and upper stop band respectively.

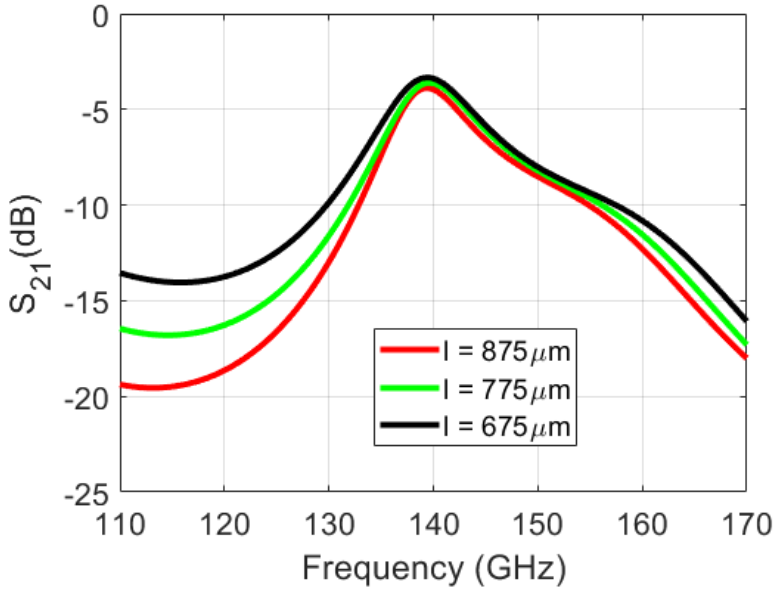

(a)

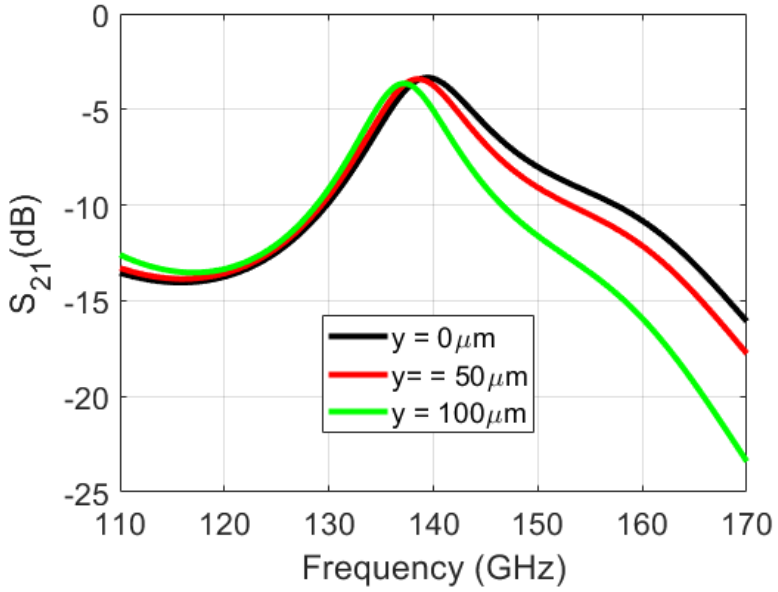

(b)

Figure 34 Response tuning of blind via filters (a) lower stop band (b) upper stop band

The responses of the filter order blind via filter operating at 140 GHz with different rejections in the stop band are given in Figure 34. By increasing the length (l) of the filter the rejection in the lower stop band can be increased and by increasing the distance of the blind via from the via side wall (y) rejection in the higher stop band can be increased. In both cases, increasing the rejection causes slight increase in the passband insertion loss which is typical band pass filters. These parameters can be used to design filters with different insertion loss and rejection requirements.

5.1.4 Higher Order filter designs

Once the parameters were identified to tune center frequency and out of band rejections, the first order structures were cascaded to design higher order filters. The blind via pairs were placed at a distance equal to the length (l) of the first order filter. The second and third

order blind via filters are given in Figure 35a and Figure 35b respectively. The frequency response (S_{21}) for the first, second and third order filters is given in Figure 35c.

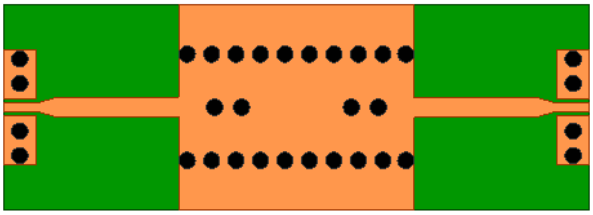

(a)

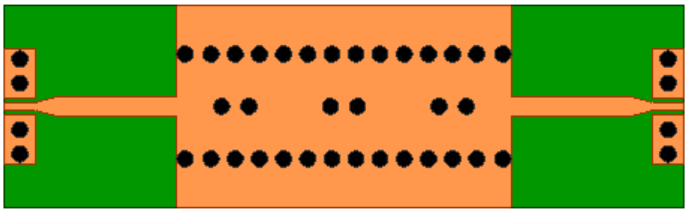

(b)

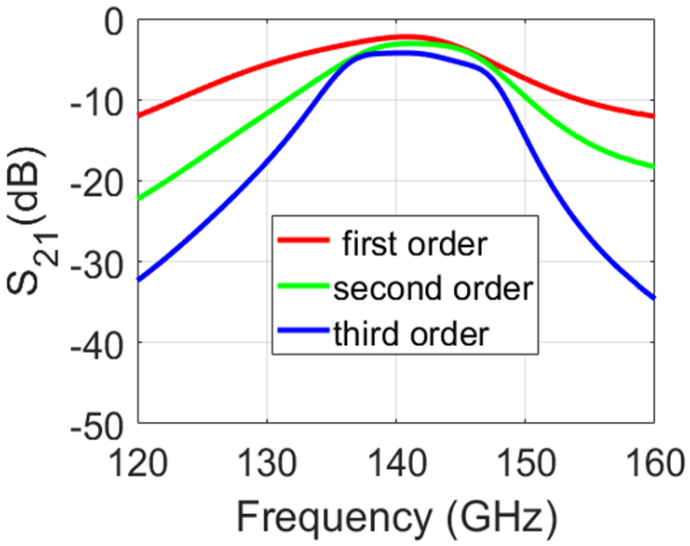

(c)

Figure 35 Higher order blind via filters (a) second order (b) third order (c) S21 (dB) for first, second and third order blind via filters

5.1.5 Response and Size Comparison with traditional SIW resonators

The physical dimensions and frequency response of the blind via filter was compared with the first order square and rectangular traditional resonator filters presented in Chapter 4. The physical dimensions of the three different types of filters are given in Figure 36a. The blind via filter is ~27% and ~40% smaller as compared to square and rectangular filters respectively. This implies that blind via filter design method is an interesting technique to design SIW filters which are significantly smaller as compared to traditional SIW resonators and they can be used to support mmWave modules.

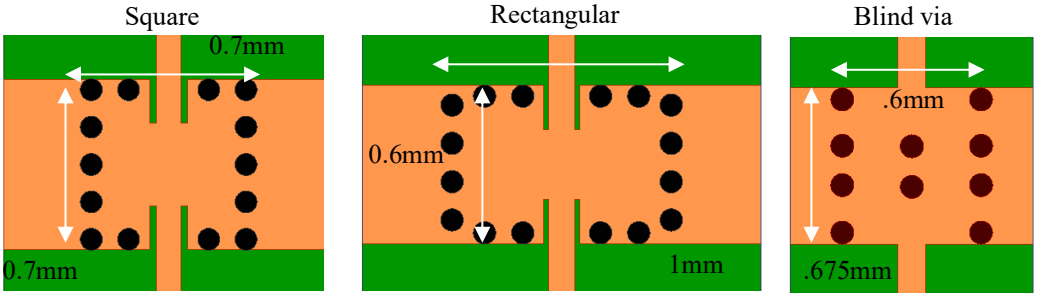

(a)

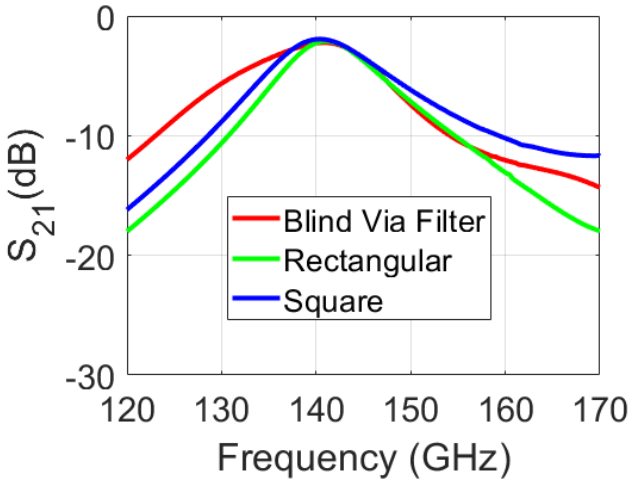

(b)

Figure 36 Size and response Comparison (a) size (b) S_{21} (dB)

5.1.6 Fabrication and Process Development

The process flow used to fabricate the blind via filters is given in Figure 37. The fabrication started by the drilling TGVs in a bare glass panel. This process was carried out by Asahi Glass Company. Then the panels were treated with silane for 20 minutes at 70°C to promote adhesion of glass with the polymer film. Then, 15 µm thick dry polymer films ABF GL102 were laminated on glass panels at 100 C using Meiki Vacuum Laminator. The lamination fills the TGVs with the polymer as shown in the 3rd step of the process flow.

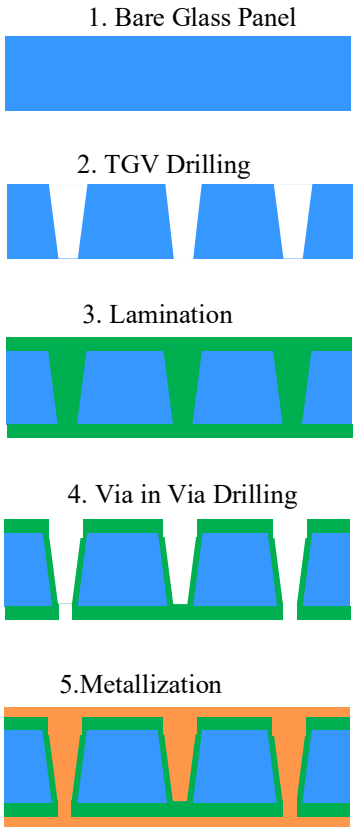

Figure 37 Process flow for fabricating blind via filters

The next step was to drill the polymer in the TGVs using CornerStone Laser machine. This was critical because two types of vias namely thru vias for SIW side walls and blind vias for the filters. To control the depth of the drill in the polymer, two process parameters namely pulse power and number of repetitions were swept in CornerStone Laser machine. Power was varied from 1.5W to 2.0W and number of repetitions were changed from 3 to 8. The test vehicle used for the process development for drilling blind vias is shown in Figure 38.

The drilled test the panel was examined in Zeta Optical Profiler from the bottom side. Thru vias were created with 1.9W of power and 8 repetitions. The required blind vias were created by power of 1.5W and 1.6W and 5 repetitions. To have a different samples three power levels (1.4W,1.5W and 1.6W) on 5 repetitions were chosen as blind via parameters. Using the derived parameters, the blind via test vehicle was fabricated. The fabricated samples are given in Figure 39.

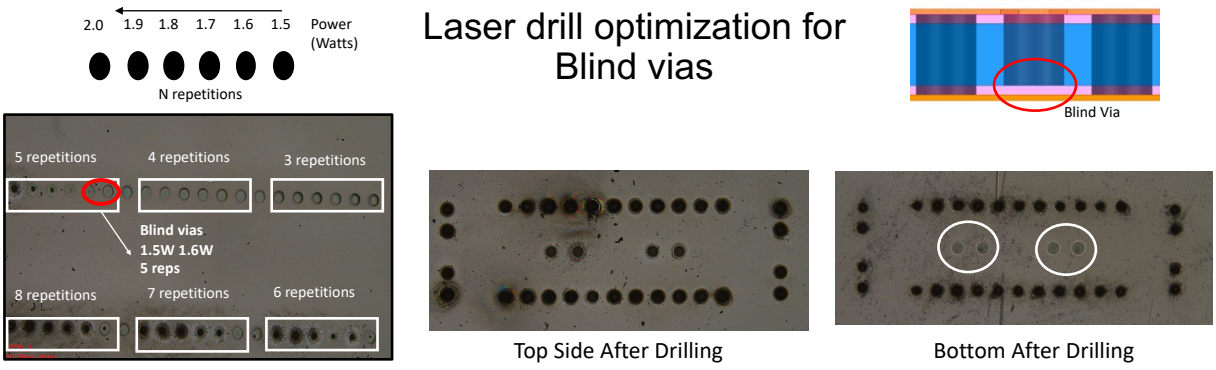

Figure 38 Process flow for drilling blind vias

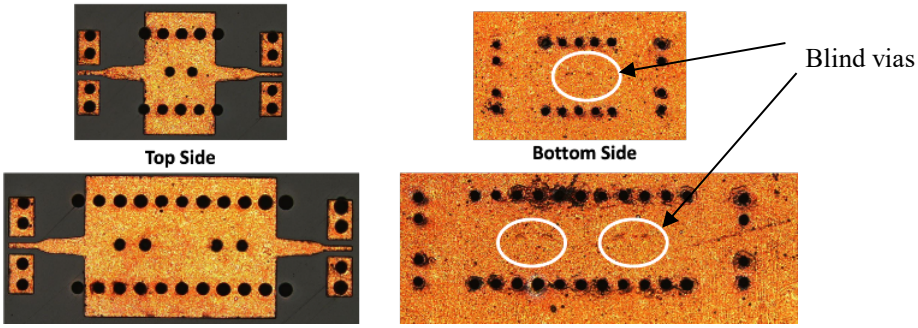

Figure 39 fabricated blind via filters

5.1.7 Measurements and discussion

The blind via filters were measured using D-band measurement set up. The measured results were not in agreement with the simulations. The fabricated SIW blind via filters were examined to find the reason for the discrepancy. It was observed that the depth of the blind vias in polymer was not consistent. It was difficult to precisely control the depth of drill in polymer. To study the effect of variation in blind via depth on the filter response, simulations were performed in Ansys HFSS. Blind via filter with via depth from 100 µm to 125µm were simulated.

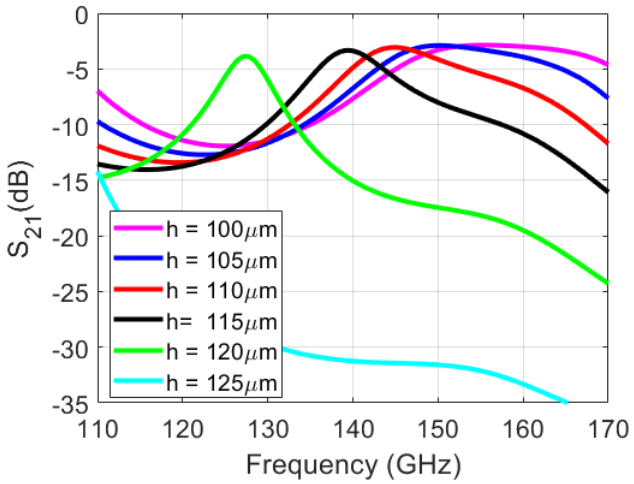

(a)

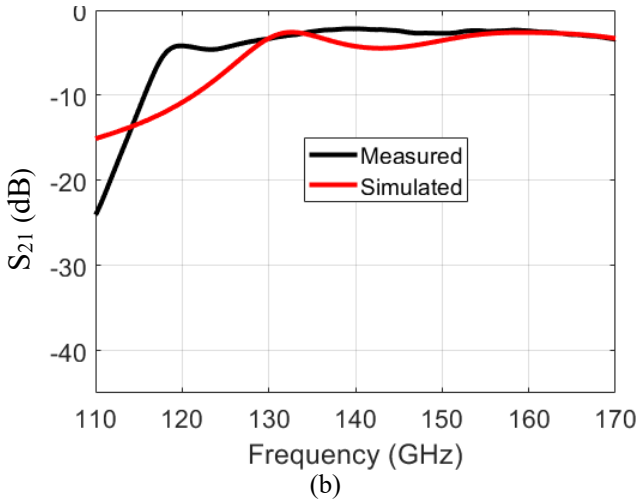

(b)

Figure 40 Post fabrication simulations for blind via filters
(a) study with different via depths (b) correlation with measured response

The simulated S_{21} (dB) for different cases are given in Figure 40a. The study showed that the response of the blind vias was extremely sensitive to the blind via depth and inability to precisely maintain 115µm via depth for blind vias was the reason for disagreement in simulation and measurement result. When the measured depth of the blind vias was modelled in the simulation it correlated well with the measurement. The post fabrication simulation model and measurement for the first order blind via filter is given in Figure 40b.

5.1.8 Lessons learnt

From the first build of blind via filters, it was concluded that with the tools and conditions available, it was very hard to control the depth of the drill in the polymer and since the response of the blind vias was sensitive to this parameter, we decided to change the material stack up.

5.2 New Material Stack up

The main challenge in the previous build was to control the depth of the drill in the polymer. It was difficult to precisely control the parameters of the laser tool and therefore even a slight change in the laser parameters or material dimension resulted in an inaccurate via drill because polymer materials get ablated very quickly. The via drilling is generally less challenging if a via stop layer (metal) is present at the end because it allows for any variations in the laser parameters and ensures an accurate via depth each time. Previously, a two-metal layer stack up was used to fabricate the blind via filters and in a two-metal layer system, we couldn't have a via stop layer for drilling blind vias. To address this, the new material stack-up had three metal layers namely M1, M2 and M3. The metal layers M1 and M3 served as top and bottom metal layer respectively and M2 was used as a via stop layer for blind vias. The three metal layers were supported on 200 µm thick AGC ENA glass by dry film polymer layers ABF GL102. 15µm thick ABF GL102 was laminated on glass core to support the first metal layer M1. Then 15µm layer was used to between the M1 and M2 metal layers and 72.5µm thick polymer layer was used between M2 and M3. The material stack up is given in Figure 41.

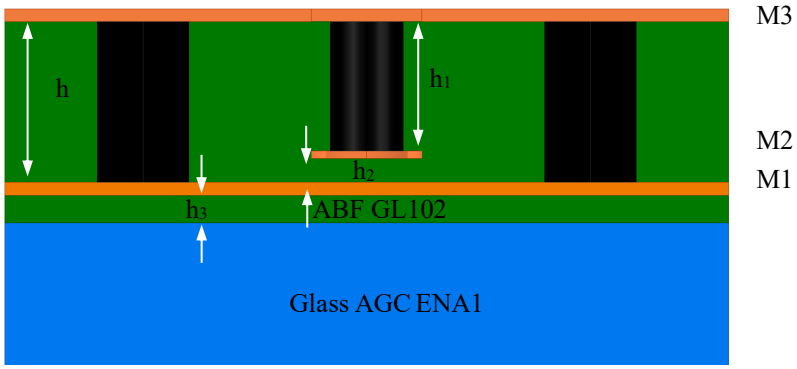

Figure 41 New material stack up for blind via filters

5.3 Design Details

5.3.1 Structure

The first order blind via filter was designed by placing a blind via (landed on a copper pad) in center of the SIW section. When a blind via is introduced in the center of an SIW section, capacitance is formed between the copper pad in M2 metal layer and the ground in M1 metal. In addition, due to this elongation of current path the equivalent inductance along the propagation direction is increased [76]. Therefore, an SIW with a blind via in the center acts as a resonant structure and it can be used to design filters. The structure of the first order blind via filter is given in Figure 42. The capacitance and inductance introduced by the blind via, and copper pad can be changed by changing various physical parameters like blind via depth (h_1), blind via diameter (d_1) and copper pad diameter (d_2). These parameters can be varied to tune the center frequency of the filter. A parametric study was done in Ansys HFSS to study the response of first order filter by changing the physical parameters.

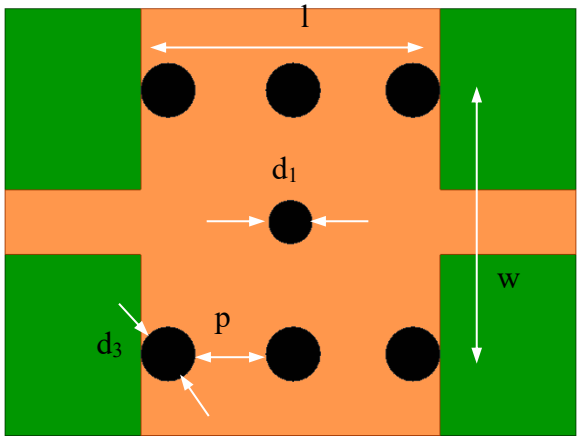

(a)

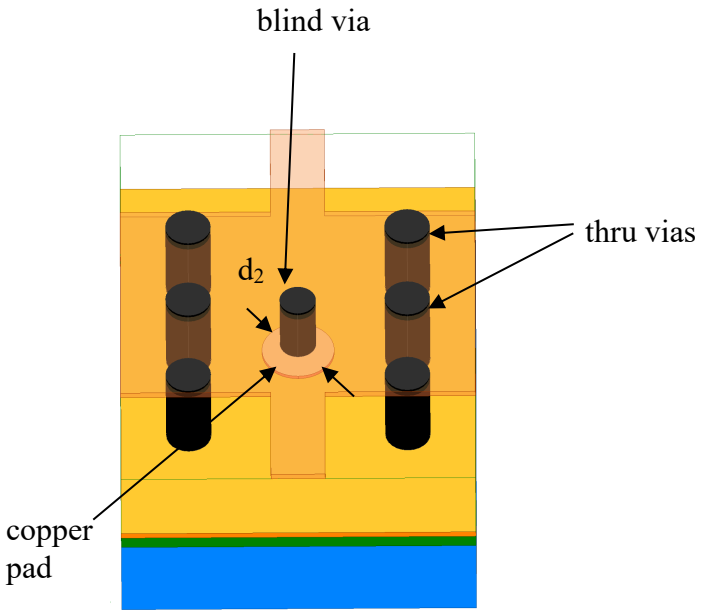

(b)

Figure 42 First order blind via filter
(a) top view (b) 3D view

5.3.2 Center Frequency Tuning

As a starting point, an SIW section with w=485 µm and l=400 µm was simulated with no blind via (h_1=0 µm). This structure behaves an SIW interconnect with cut off frequency around 200 GHz. Then three cases with different blind via depths (h_1=30um, 50um and 70um) were simulated. Introducing a blind via and copper pad in the SIW section changes the response and the structure starts behaving as a filter due to the capacitance and inductance offered by the blind via and the copper pad. The simulated S_{21} (dB) for different cases is given in Figure 43. The center frequency of the filter decreases by increasing the depth of the blind via (h_1).

This can be explained based on increase in the capacitance and inductance due to increasing the blind via depth. A deeper blind via results in smaller distance (h_2) between the copper pad and ground metal layer which increases the capacitance. In addition, a deeper blind via also introduces a larger inductance because it provides a longer current path. Both factors contribute to lower the center frequency by increasing the blind via depth.

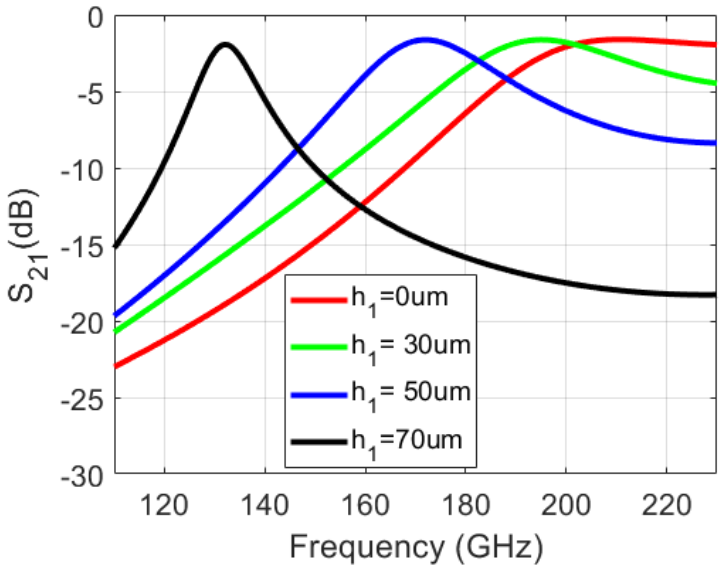

Figure 43 Simulated S_{21} (dB) for first order blind via filter with different blind via depths

Once the effect of blind via depth was studied, the next important parameter was the diameter of the blind via (d_1). The effect of changing the diameter of the blind via was studied. For this case, the depth of the blind via (h_1) and copper pad diameter (d_2) were 70 µm and 120 µm respectively. Different cases with 40 µm, 60 µm, 80µm and 100µm blind via diameters were simulated using Anys HFSS. The simulated responses (S_{21}) for different

cases are given in Figure 44. Increasing the diameter of the blind via (d_1) shifted the resonant frequency to the upper side.

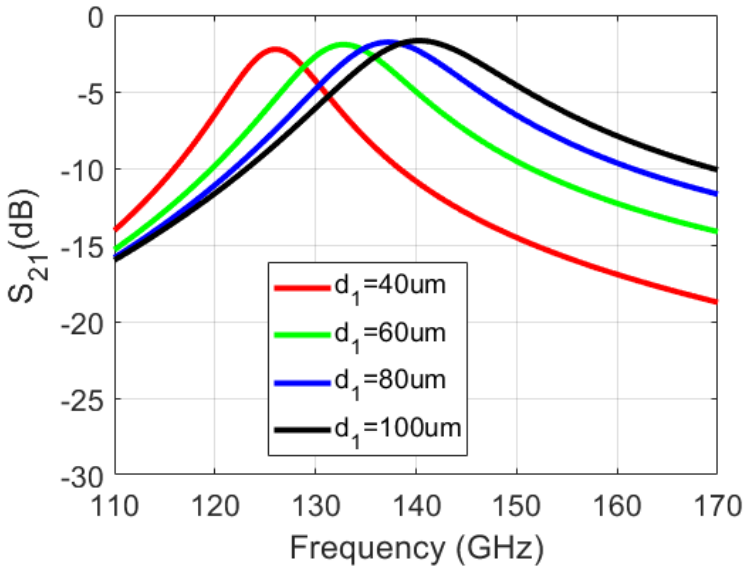

Figure 44 Simulated S_{21} (dB) for first order blind via filter with different blind via diameters

This can be explained based on the change in the inductance of blind via. As described in [76, 77] the diameter and inductance of a blind via are inversely related to each other because a thinner blind via provides a longer current path on the copper pad and hence adds more inductance. Therefore, by increasing the blind via diameter its inductance decreases and resonant frequency of the blind via filter increases.

Next, the effect of changing the diameter of the copper pad (d_2) was studies. In this study, the blind via depth (h_1) and blind via diameter (d_1) were fixed to 70um and 65um respectively. Four cases with 80 µm, 100 µm, 120 µm and 140 µm copper pad diameters (d_2) were simulated using Ansys HFSS. The simulated responses (S_{21}) are given in Figure 45. Increasing the diameter of the copper pad increases the capacitance and inductance

produced by the copper pad, which results in a decrease in the center frequency. A larger copper pad has increased capacitance because it provides more area to store electric field and increased capacitance because it provides lengthened path to current.

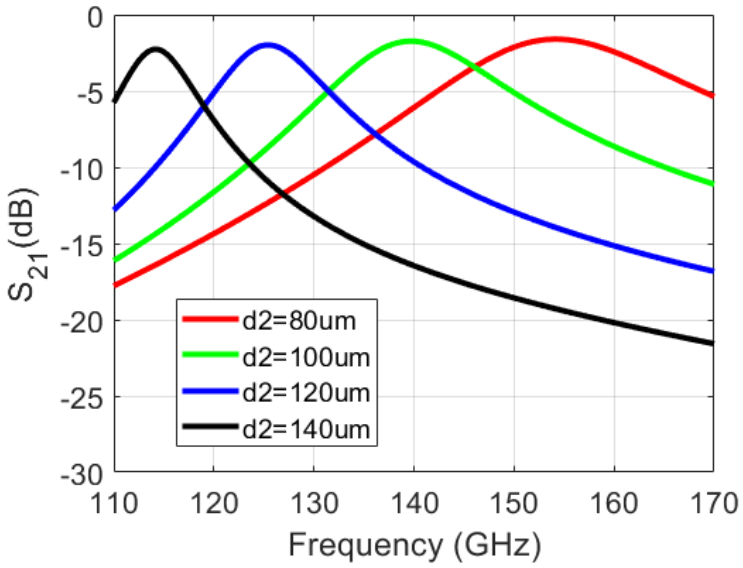

Figure 45 Simulated S_{21} (dB) for first order blind via filter with different copper pad diameter

Based on the above parametric study, three parameters (h_1, d_1, d_2) can be used to tune the center frequency of the filter.

5.3.3 Filter roll off tuning

Once the effect of blind via dimensions ((h_1, d_1, d_2) was studied, the next step was to study the effect changing the SIW dimensions (w and l) on the filter response. For this study, the blind via depth (h_1), blind via diameter (d_1) and copper pad diameter (d_2) values were 70 µm, 65 µm and 120 µm respectively. Three cases for 455 µm, 485µm and 515 µm SIW width (w) were simulated using Ansys HFSS. The length (l) of the blind via filter was

450um for this case. The simulated responses (S_{21}) for the different cases are given in Figure 46.

Reducing the width (w) of blind via filter increases the rejection of the filter in the lower stop band. This effect can be explained due to the increase in cut off frequency of the SIW structure due to decreasing width. The center frequency also slightly increases by decreasing the width of the SIW section in blind via filter.

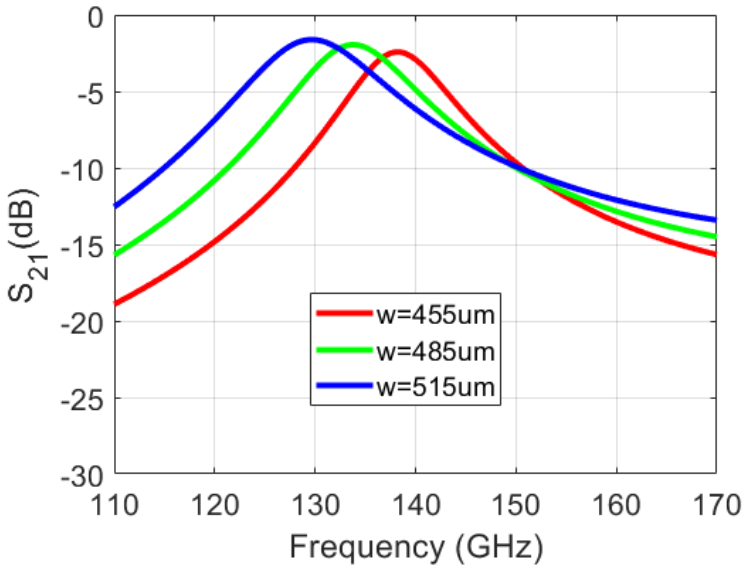

Figure 46 Simulated S_{21} (dB) for first order blind via filter with different widths for SIW section

To study the role of the length of SIW section three cases for 350 µm, 450 µm and 550 µm length of SIW (l) with the same blind via dimensions were simulated using Ansys HFSS. The width (w) of blind via filters in this case 485um. The simulated responses (S_{21}) for the different cases are given in Figure 47.

The results show that increasing the length (l) improves the rejection of the filter in both stop bands at the expense of slightly increasing passband insertion loss. This effect can be

explained due to the high pass characteristic of the SIW section. Since the SIW section with 485 µm width has a cut of frequency around 200 GHz it rejects frequencies in the stop band.

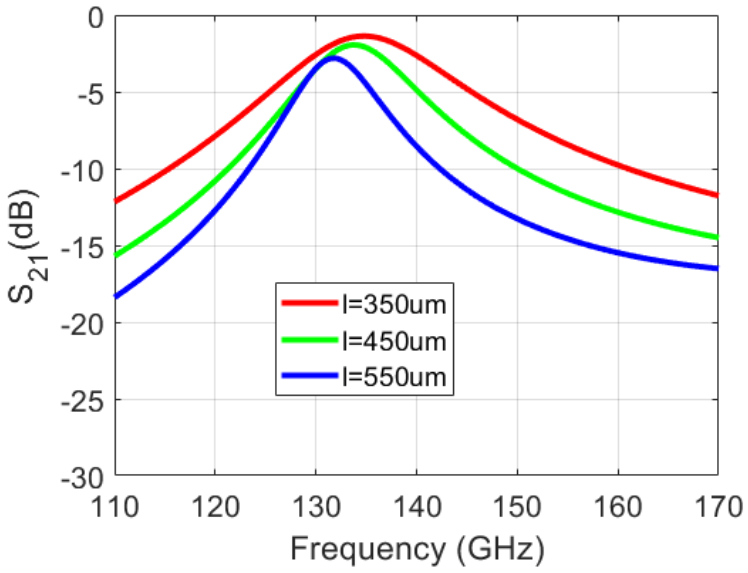

Figure 47 Simulated S21 (dB) for first order blind via filter with different lengths of SIW section

5.3.4 Higher Order Filters

Once the first order blind via filter is designed, higher ordered filters can be designed by cascading first order filters. While cascading the filters, the first blind via is placed at a distance l/2 from the edge of the SIW and the two adjacent blind vias are placed at distance of l, where l is the length of the first order SIW filter. The second and third order blind via filters are given in Figure 48a and Figure 48b respectively. The simulated responses S_{21}

(dB) of the first, second and third order blind via filter operating ~125 GHz are given in the figure below.

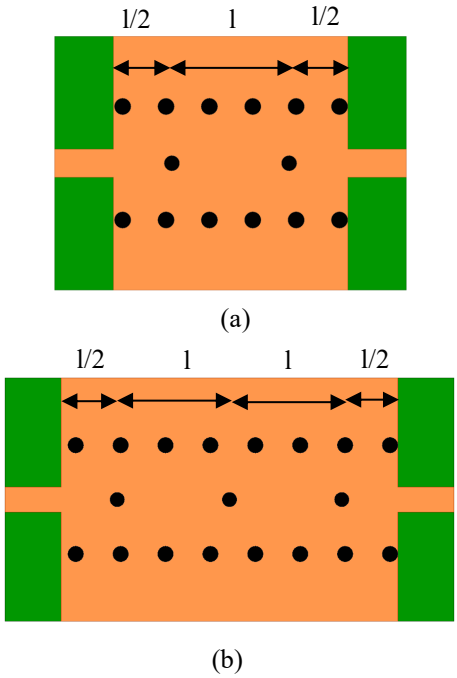

Figure 48 Higher order blind via filters (a) second order (b) third order

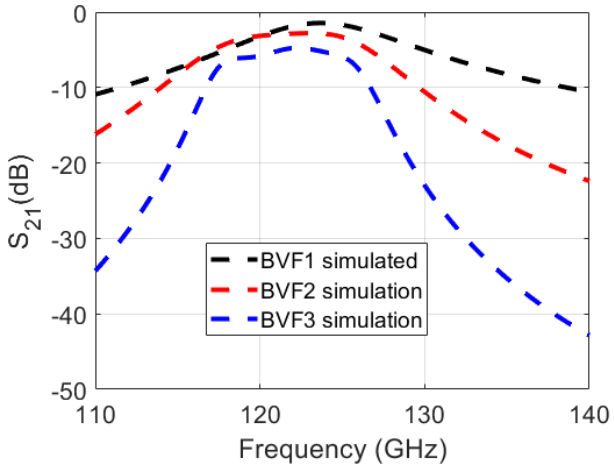

Figure 49 Simulated S_{21} (dB) of first, second and third order blind via filter (BVF)

5.3.5 Microstrip feed and CBCPW transition design

The designed filters were fed by using microstrip lines. Since the designed structures were to be measured using RF GSG probes, CBCPW to microstrip transitions were added. The transitions were designed as discussed in Chapter 2. To remove the loss from CBCPW probe pads and CBCPW to microstrip transitions, TRL structures were designed. The reference plane after TRL calibration is shown in Figure 50.

After TRL calibration, the measured results will have effect of feed lines and blind via filter

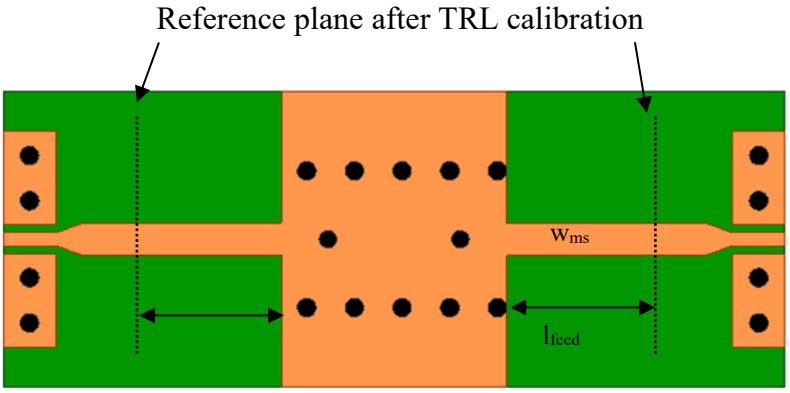

Figure 50 Blind via filter with CBCPW probe pads, transitions, and feed lines

5.4 EM fields in blind via filters

The dimensions of the blind via filters are smaller compared to traditional SIW cavity resonators. To understand this, electric and magnetic fields were plotted in a blind via filter. The electric and magnetic fields are given in Figure 51. Due to the presence of blind via and copper pad most of the electric field remains confined between the copper pad and the ground layer whereas the magnetic field is present throughout the structure. This physical separation between the electric and magnetic fields is a well-known attribute of slow wave propagation as reported in [69],[76]. This confirms that due to the slow wave phenomena

at the center frequency blind via filters will have smaller size as compared to the traditional SIW cavity-based resonators. This size comparison will be discussed in detail in Section V of this paper.

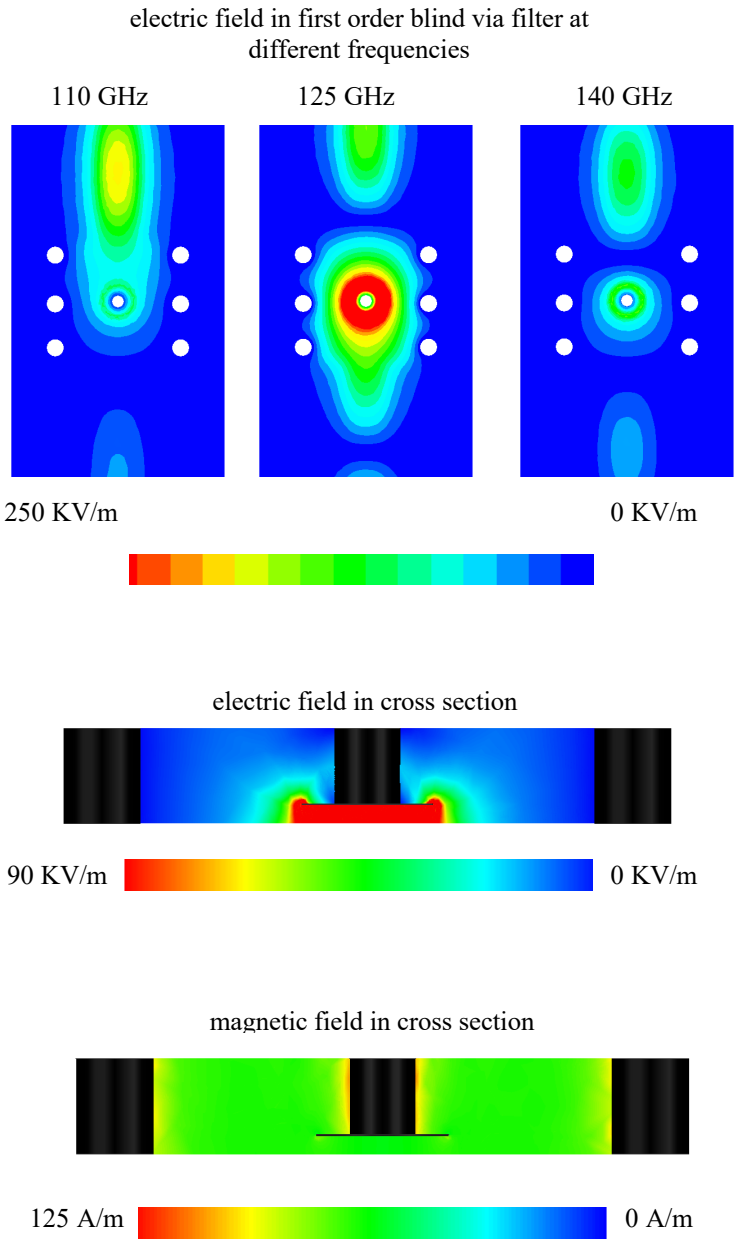

Figure 51 EM fields in a blind via filter

5.5 Fabrication

The process flow used to fabricate the blind via filters is given in Figure 52. The 200 µm thick AGC ENA1 glass panel was treated with silane for 20 mins at 70º C followed by Oxygen plasma treatment for 5 mins. Then 15 µm thick ABF GL102 was vacuum laminated on glass panel at 100º C using Meiki Vacuum Laminator. Next, the dry films were cured at high temperatures. Then, electroless seed layer was deposited on the dry film using desmear based electroless copper deposition process. The target thickness for seed layer was 300 nm. Then, M1 metal layer was plated up to 7µm by using electroplating. Since M1 metal layer was going to be used as a ground plane, it was not patterned. Then, M1 metal layer was treated by NovaBond process to improve adhesion between the metal-polymer interface, and then 15 µm thick ABF dry film was vacuum laminated to build the next metal layer. The laminated dry films were cured at higher temperatures. Then copper seed layer was deposited using electroless copper deposition. Then, dry film photoresist was laminated, and the seed layer was patterned using photolithography using Tamarac Mask Aligner. M2 metal layer was plated up to 7 µm by electroplating and then seed layer removal by differential etching. Next, M2 metal layer was then treated by the NovaBond process for adhesion promotion. Then, 72.5 µm thick ABF GL102 was vacuum laminated on the M2 metal layer. The laminated dry film was cured at high temperatures. Then, blind, and thru vias were drilled using Optec Femtosecond Laser Drilling System. The fabricated samples of blind via filters are given in Figure 53.

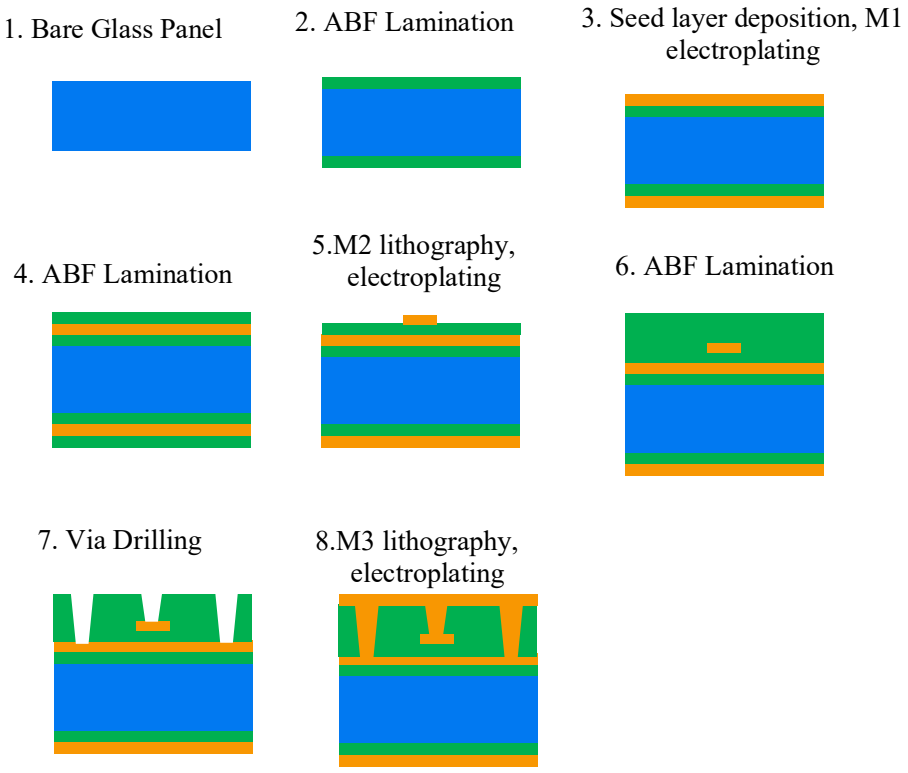

Figure 52 Process flow for fabricating blind via filters

The via drilling process parameters were separately optimized for thru and blind vias. Since we were using panel scale mode (IFOV) in Optec Femtosecond Laser system, alignment between the copper pads and blind vias was critical as IFOV mode exhibit alignment drift in a six-inch panel. After various trials, acceptable alignment (<10 µm) was achieved in IFOV mode and panels were accurately drilled. Then M3 metal layer was patterned on seed layer using photolithography, followed by electroplating and seed layer removal by differential etching.

Table 8 Physical Dimensions for blind via filter test vehicle

Parameter	Symbol	Designed (µm)	Fabricated (µm)
width	w	515	509.3
length	l	450	447.5
blind via depth	h_1	70	67.5
blind via diameter	d_1	65	63.2
pad diameter	d_2	120	116.6
thru via diameter	d_3	70	68.5
thru via pitch	p	130	133.5
microstrip width	w_{ms}	127	121.5
feed line length	l_{feed}	500	503.8

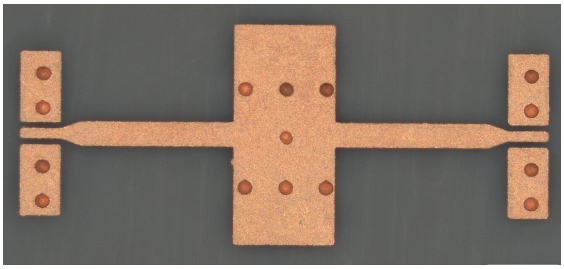

(a)

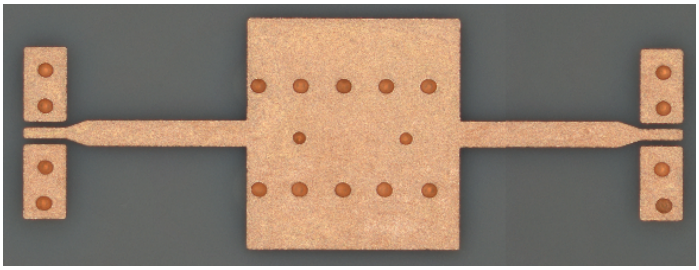

(b)

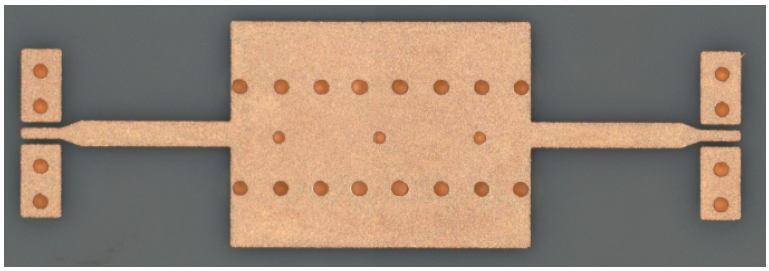

(c)

Figure 53 Fabricated samples of blind via filters (a) first order (b) second order (c) third order

5.6 Measurements

The designed blind via filters were measured using Keysight vector network analyzer (E8361C) along with frequency extenders (V06VNA2) and mmWave controller. The scattering parameters were measured from 110 GHz to 140 GHz. The samples were probed using Cascade Infinity probes 170-S-GSG-75-BT (75 μm). Since the designed filters included CBCPW to microstrip transitions for probing, two tier calibration was used to de-

embed the response of the filters. First, LRRM calibration was performed using Cascade Wincal and calibration substrate to move the reference plane to the edge of the probes. These measurements included the effects of CBCPW to microstrip transitions. Then using the measured S-parameters of thru, reflect and line structures, TRL calibration was performed to eliminate the effect of CBCPW probe pads and transitions. The measured scattering parameters for the blind via filters are given in Figure 54. The measured center frequency for first, second and third order blind via filter was 125.2 GHz, 123.2 GHz, and 120.9 GHz respectively. The measured insertion loss values at the center frequencies were 2.31 dB, 3.8 dB and 5.2 dB respectively. The measured bandwidth was 7.85%, 6.5% and 7.8% respectively. Except for a few minor deviations which can be attributed to slight changes in fabricated dimensions and measurement uncertainties, the simulated and measured results have decent agreement.

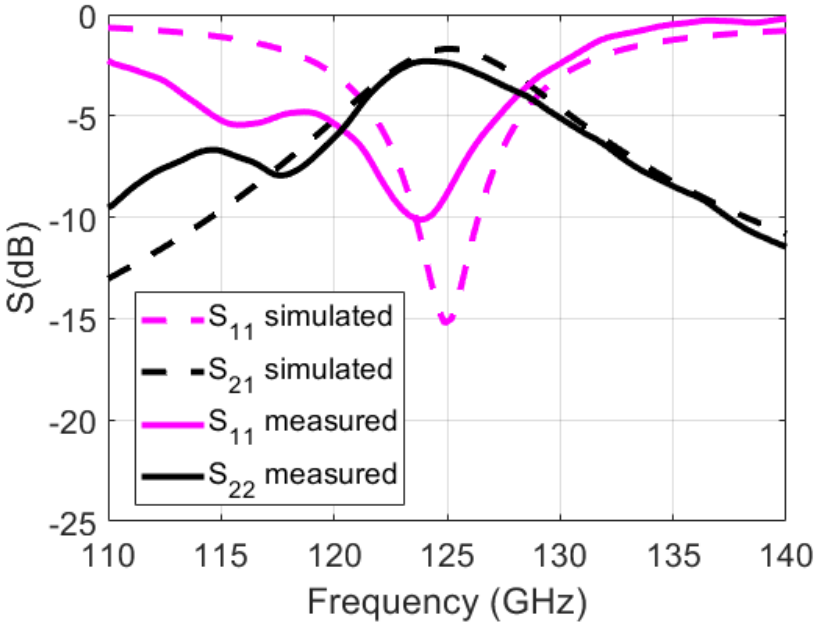

(a)

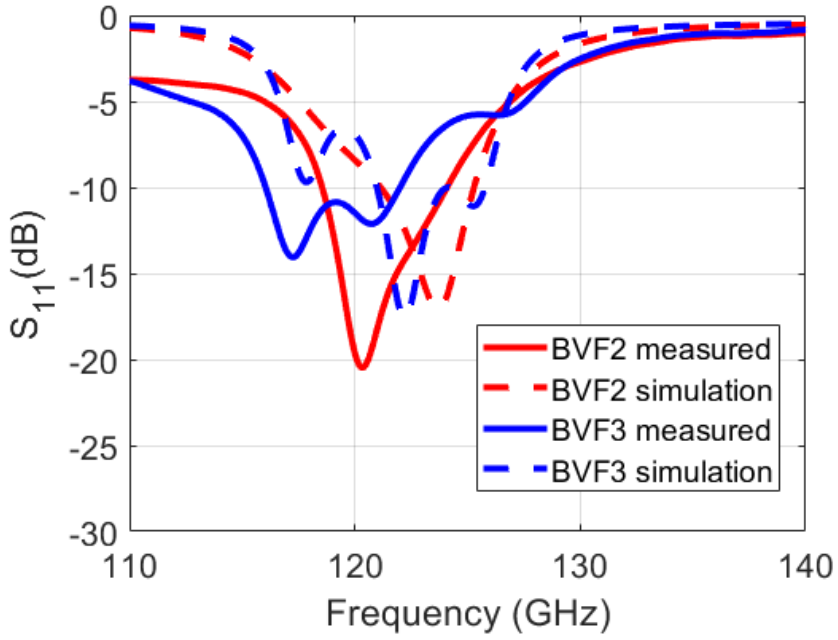

(b)

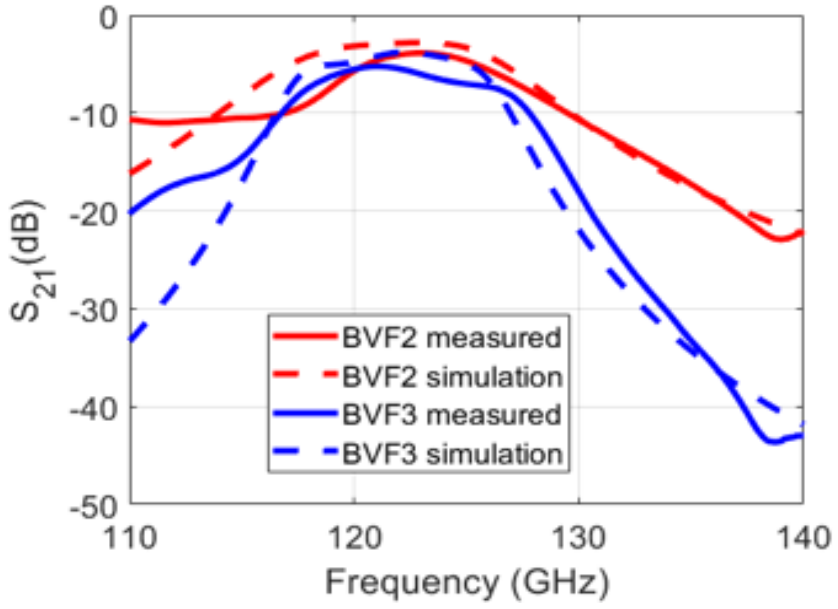

(c)

Figure 54 Measured scattering parameters (dB) for the designed blind via filters (a) S11 and S21 for first order filter (BVF1) (b) S11 for second (BVF2) and third (BVF3) order (c) S21 for BVF2 and BVF3

5.7 Traditional SIW Resonators

To compare the size and electrical performance of the designed blind via filters, traditional SIW cavity-based filters were also designed and fabricated using the same material stack up. Since traditional SIW resonators didn't need blind vias, the M2 metal layer was not used in designing them. Rest of the material stack up was same. The diameter and pitch of the via side wall were 80 µm and 90 µm respectively. The target center frequency was 125 GHz so the response and size can be compared with the blind via filters.

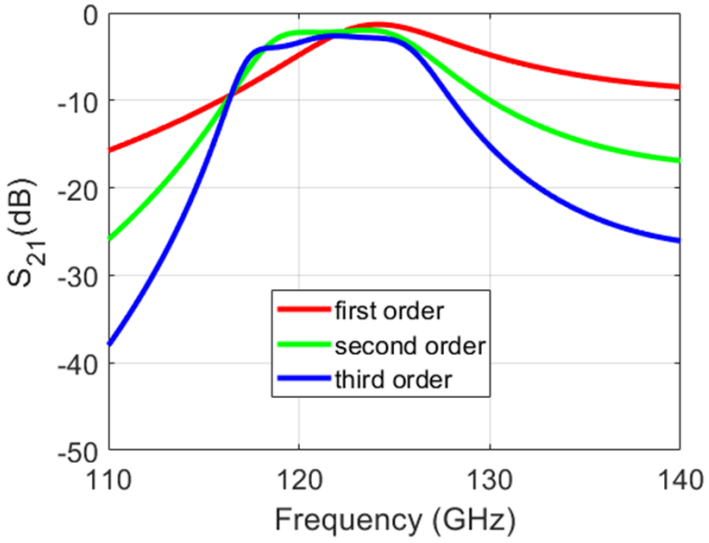

Figure 55 Simulated (S_{21}) for SIW cavity filters in ABF

Simulation models were built using Ansys HFSS. First, second and third order filters were designed. The simulated scattering parameters (S_{21}) for the designed filters are given in Figure 55 . Center coupled microstrip line was used to feed the SIW cavities. The coupling slot was designed by using the procedure described in Chapter 4. CBCPW to microstrip transitions were added to probe the filters using RF GSG probes. To de-embed the response of the design SIW resonators, TRL structures were included in the test vehicle.

The fabrication procedure was the same as described in Section 5.4 of this chapter. The fabricated samples are given in Figure 56.

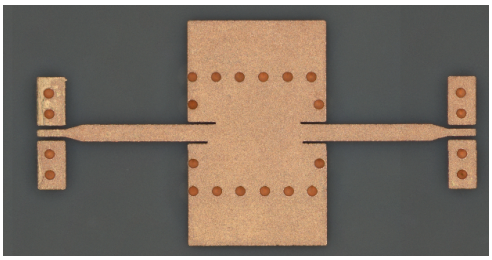

(a)

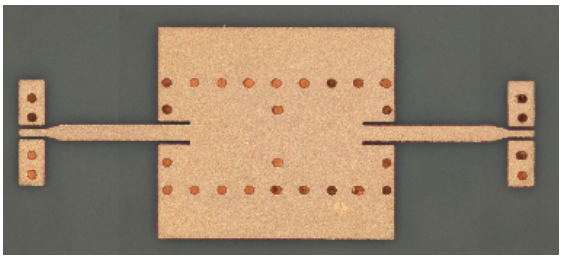

(b)

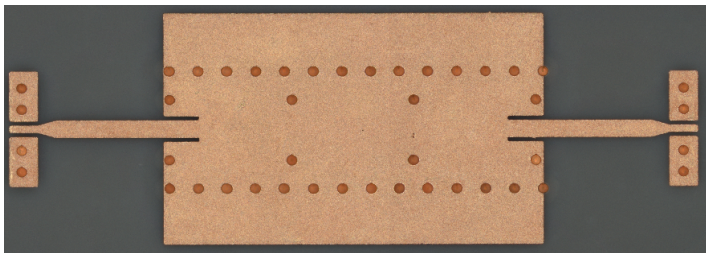

(c)

Figure 56 Fabricated samples of SIW resonators on ABF (a) first order (b) second order (c) third order

The measured scattering parameters of the SIW cavity filters are given in **Figure 57**. The center frequencies in the measured responses were shifted by ~4 to ~6 GHz. This shift can be explained based on change in fabricated dimensions like SIW cavity size and via diameters as explained in Chapter 4. Post fabrication simulation models were built

by measuring the fabricated dimensions using Keyence Optical Profiler. The post fabrication simulations are in good agreement with the measured results.

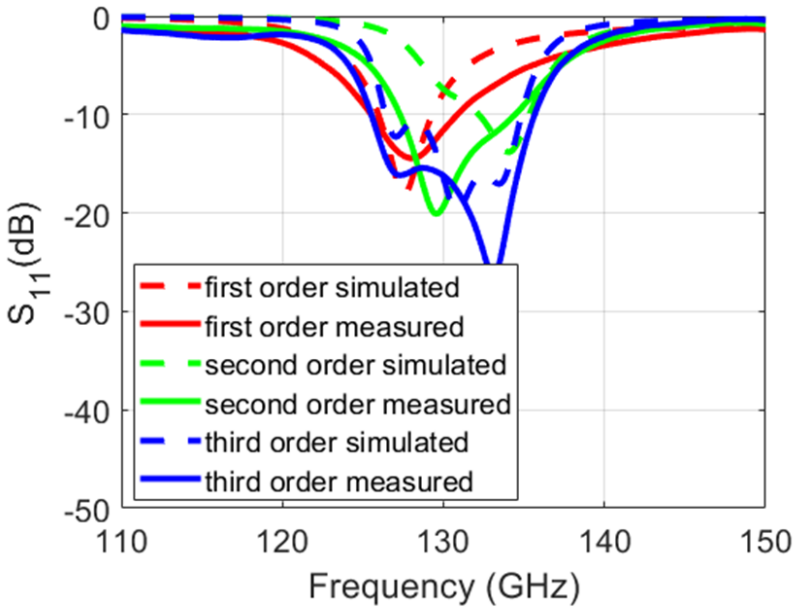

(a)

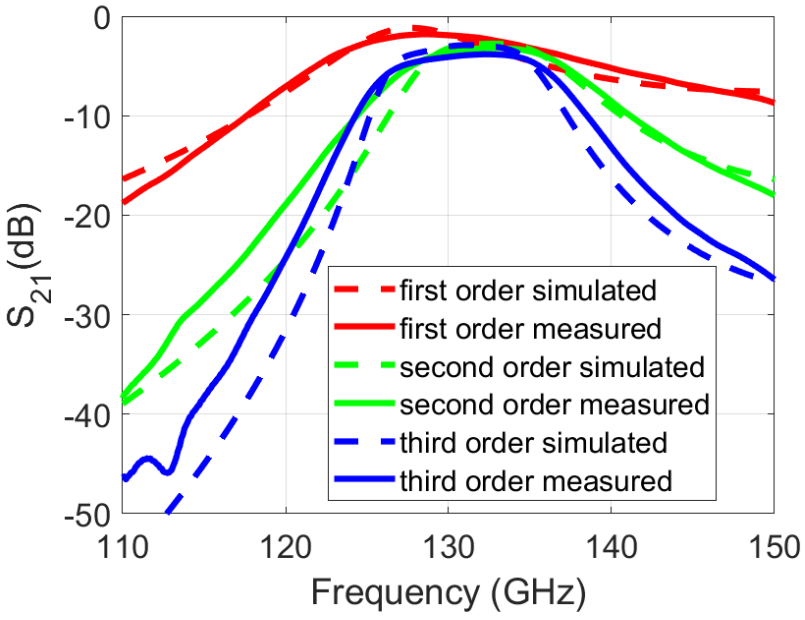

(b)

Figure 57 Simulated and measured scattering parameters of SIW cavity filters on ABF (a) S_{11}(dB) (b) S_{21}(dB)

5.8 Size and Response Comparison

The size and frequency response of a third order blind via filter and SIW cavity filter were compared. Since the measured center frequencies for the were slightly different, the frequency axis was normalized with respect to the center frequencies of the filters. The center frequencies for third order blind via filter and SIW cavity filter were 120.9 and 130.7 respectively. The measured response (S_{21}) is compared in Figure 58.

SIW cavity filter and blind via filter have comparable response in passband. SIW cavity filter has a sharp roll off in the lower stop band frequencies due to SIW cut off characteristics but the rejection for higher stop band frequencies is slightly inferior due to the propagation of higher order modes. On the other hand, blind via filter is superior in rejecting the upper stop band but the lower stop band has inferior rejection. The rejection in the lower stop band for a blind via filter can be improved by changing the length and width of the SIW section as described in the design procedure. The comparison shows that both filter types have distinct performance advantages which makes SIW technology promising for supporting mmWave modules.

The response comparison is given in Figure 58. The size comparison for blind via filters and traditional SIW cavity based filters is given in Table 9.

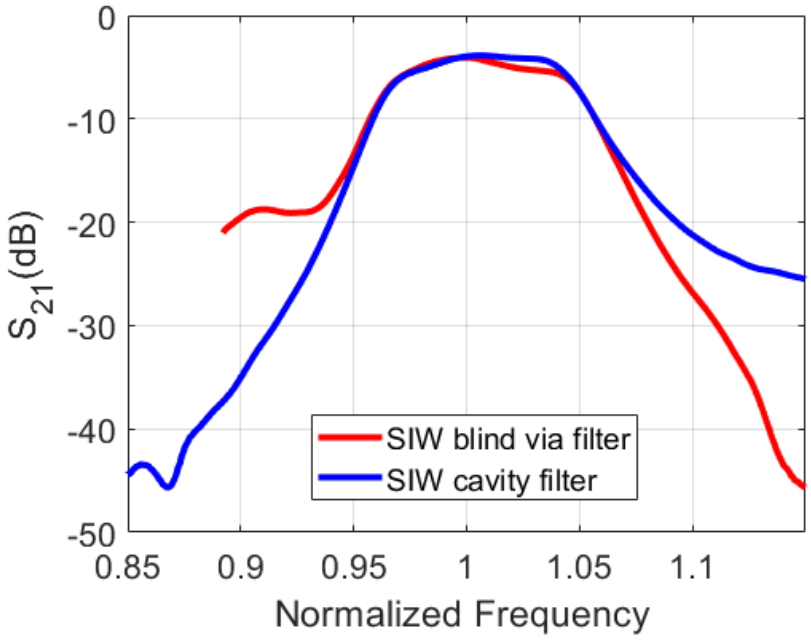

Figure 58 Response comparison

Table 9 Size Comparison for SIW cavity and blind via filters

Filter Type	Order	IL (dB)	Center Frequency	Size (wxl) mm x mm	Size factor (blind via/ SIW cavity)
SIW Cavity	1	1.7	128.5	.84 x 1.08	
	2	3.4	131.8	.84 x 1.95	
	3	4.0	130.7	.84 x 2.8	
Blind via filters	1	2.3	124.8	.515 x .45	0.25
	2	3.8	123.2	.515 x .90	0.28
	3	5.2	120.9	.515 x .135	0.29

Once the response of the filters was compared, the next step was to compare the physical dimensions of the filters because one of the most promising features of SIW blind via filter design method is miniaturization. Fabricated samples of a third order SIW cavity filter and third order blind via filters are given in Figure 59. The waveguide section of the traditional SIW cavity filter is 840 µm wide and 2.8 mm long whereas the blind via filter is 515 µm wide and 450 µm long. The blind via filter is only ~30% of the size as compared to the traditional SIW cavity filter. The size comparison of different orders of SIW cavity filters and blind via filters is given in Table 9. For all the orders, blind via filters are less than a third of the size of the traditional SIW cavity filters. It is important to note that in the demonstrated example the center frequency of SIW cavity filter is ~10 GHz higher compared to the blind via filter. An SIW cavity filter with the same center frequency (~120 GHz) will be even larger.

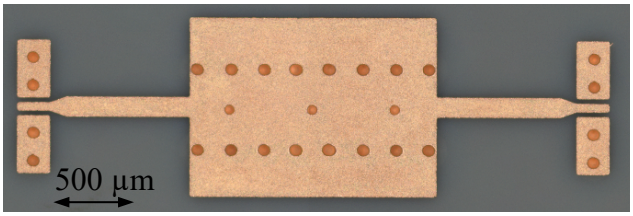

(a)

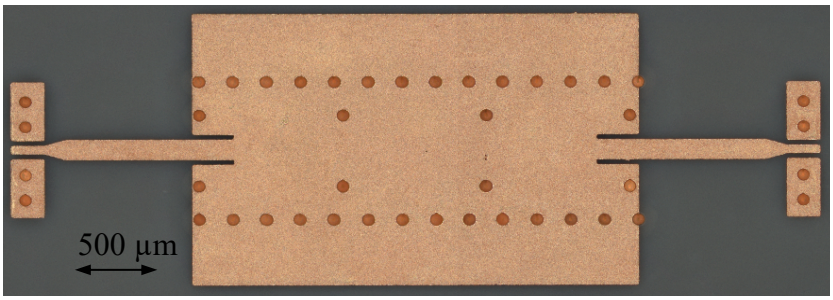

(b)

Figure 59 Size comparison (a) blind via filter (b) SIW cavity filter

The insertion loss, bandwidth and size of the designed filters is compared with other state of the published work in Table 10. The filters given in Table 10 have different substrate heights and feeding methods a direct comparison of the insertion loss is difficult. The electrical performance and size reduction show that SIW blind via filter design method has great potential for realizing miniaturized SIW filters with good electrical performance.

Table 10 Performance and size comparison with other published work

Material	**Order**	**IL (dB)**	**Freq (GHz) f_0**	**BW (%)**	**size (λ_0 x λ_0) $\lambda_0=c/f_0$**
LCP [58]	2	2.6	94	8	.63 x .57
HR Si [59]	4	3.9	140	10	Not Reported
LTCC [60]	3	1.913	140	13.0	.38 x .57
Thick Film [61]	4	3.33	94	7.3	.28 x .8
	4	3.86	150	8	Not Reported
BCB [62] (sim.)	3	1.5	159.7	12.5	.45 x 1.2
ABF SIW Resonators	1	1.7	128.5	7.5	.35 x .43
	2	3.4	131.8	7.5	.36 x .84
	3	4.0	130.7	8	.36 x 1.2
ABF SIW Blind Via Filters	1	2.3	124.8	7.8	.21 x .19
	2	3.8	123.2	6.5	.21 x .38
	3	5.2	120.9	7.8	.21 x .57

CHAPTER 6. MICROSTRIP LINES AND SIW ON ABF

The performance of interconnects like microstrip lines, CPWs and SIWs was benchmarked on the ABF/glass/ABF material stack up in Chapter 2 and Chapter 3 because this material stack-up serves as a basic building block for making passives and interconnects in a glass interposer. The glass interposer technology usually uses 2-metal layer system on ABF/glass/ABF material stack up. To design different RF interconnects and passives, more metal layers are required and therefore more polymer layers are laminated on top the ABF/glass/ABF stack up. For the same reason, new material stack up was used to design blind via filters because a 2-metal layer stack up had limitations.

The microstrip lines and SIWs designed in Chapter 2 and Chapter 3 respectively, use ABF/glass/ABF stack up. This chapter will demonstrate the electrical properties of these interconnects on 87.5 µm thick ABF supported on ABF/glass/ABF material stack up.

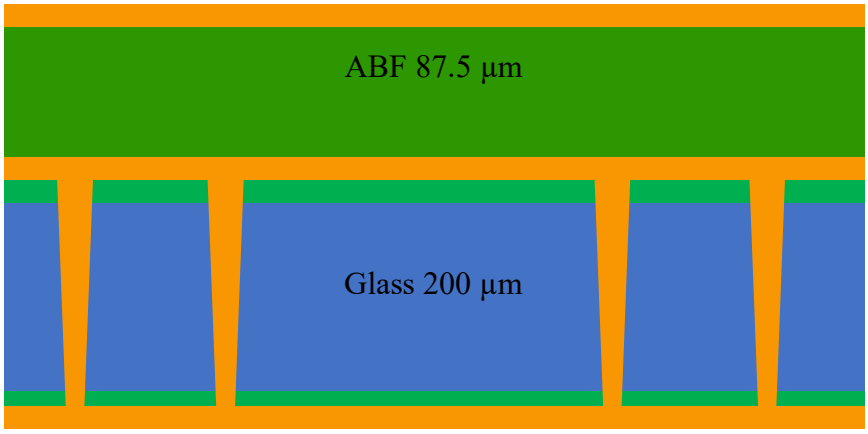

Figure 60 Material stack-up

6.1 Design

The design method for both type of interconnects is described below.

6.1.1 Microstrip lines

Microstrip lines were designed on 87.5 µm thick ABF material. The dielectric constant of ABF was modelled as 3.3 The width for 70Ω microstrip line was calculated using Linecalc utility in Keysight ADS [36]. The simulation model was built using Ansys HFSS [37]. CBCPW to microstrip transitions were added to probe the designed microstrip line using GSG RF probes. TRL structures were included in the test vehicle to de-embed the response of the microstrip line. The designed 3.3mm long microstrip line with CBCPW to microstrip transitions is given in Figure 61a.

6.1.2 SIWs

SIWs were designed using Ansys HFSS. The width of the SIW was designed to be 1mm to keep cut off frequency below 90 GHz. The pitch and diameter for the via side wall were designed to 90 µm and 80 µm respectively. These values obey the design rules presented in [48] for negligible radiation loss. The SIWs were fed using microstrip taper transitions. These transitions have good broadband performance. The transitions were designed using Ansys HFSS. CBCPW to microstrip transitions were added to probe the designed SIWs. TRL structures were included in the test vehicle to de-embed the response of the SIW section. The designed 5mm long SIW with CBCPW to microstrip transitions and microstrip taper feed is given in Figure 61b.

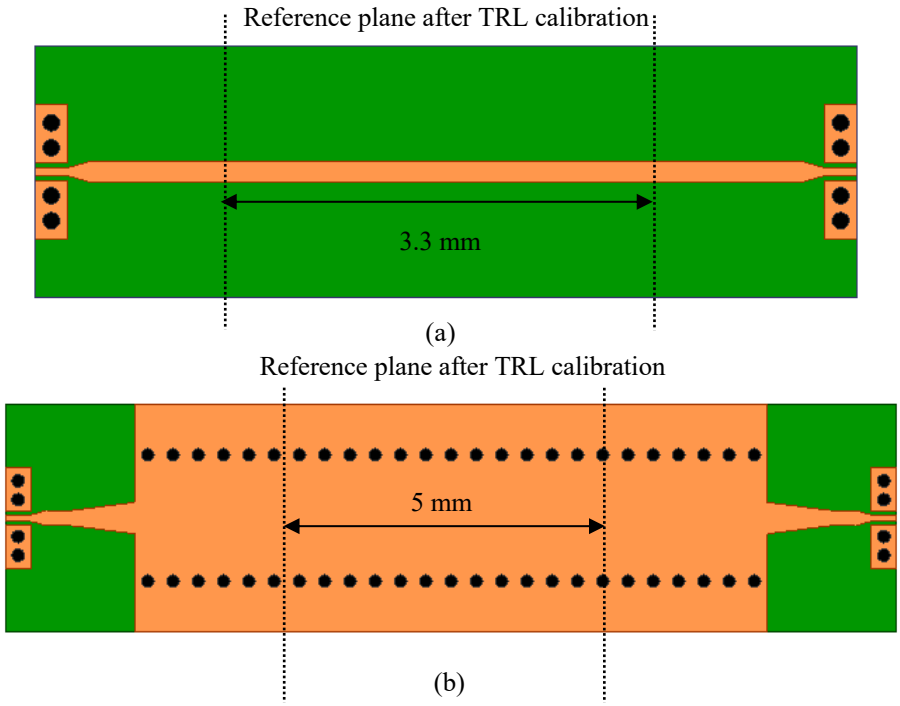

Figure 61 Designed structures (a) microstrip line (b) SIW

6.2 Fabrication

The process flow used to fabricate the designed test vehicle is given in Figure 62. The fabrication started with plasma and silane treatment of 200 µm thick AGC ENA1 bare glass. Then 15 µm thick ABF GL102 dry films were vacuum laminated on both sides of the glass panel using Meiki Vacuum Laminator. The lamination was done at 100º C and after lamination the stack-up was cured at 130º C for 30 mins and then at 170º C for 30 mins. Then Copper seed layer was deposited using electroless Copper deposition and then it was plated up to 7 µm using electrolytic plating. Then the stack up was treated with NovaBond process and then 15 µm ABF dry film was laminated. Next, 72.5 µm thick ABF GL102 film was laminated. Then the stack up was cured again at high temperatures. Then

vias for the CBCPW probe pads and SIW via side walls were drilled using Optec Femtosecond Laser Tool. Then copper seed layer was deposited for M2 metal layer. Next, 15 µm thick dry film photoresist was vacuum laminated at 80º C using Meiki Vacuum Laminator. Seed layer was patterned using photolithography and then photoresist was developed. Then, the copper was plated up to 7 µm and seed layer was removed using differential etching.

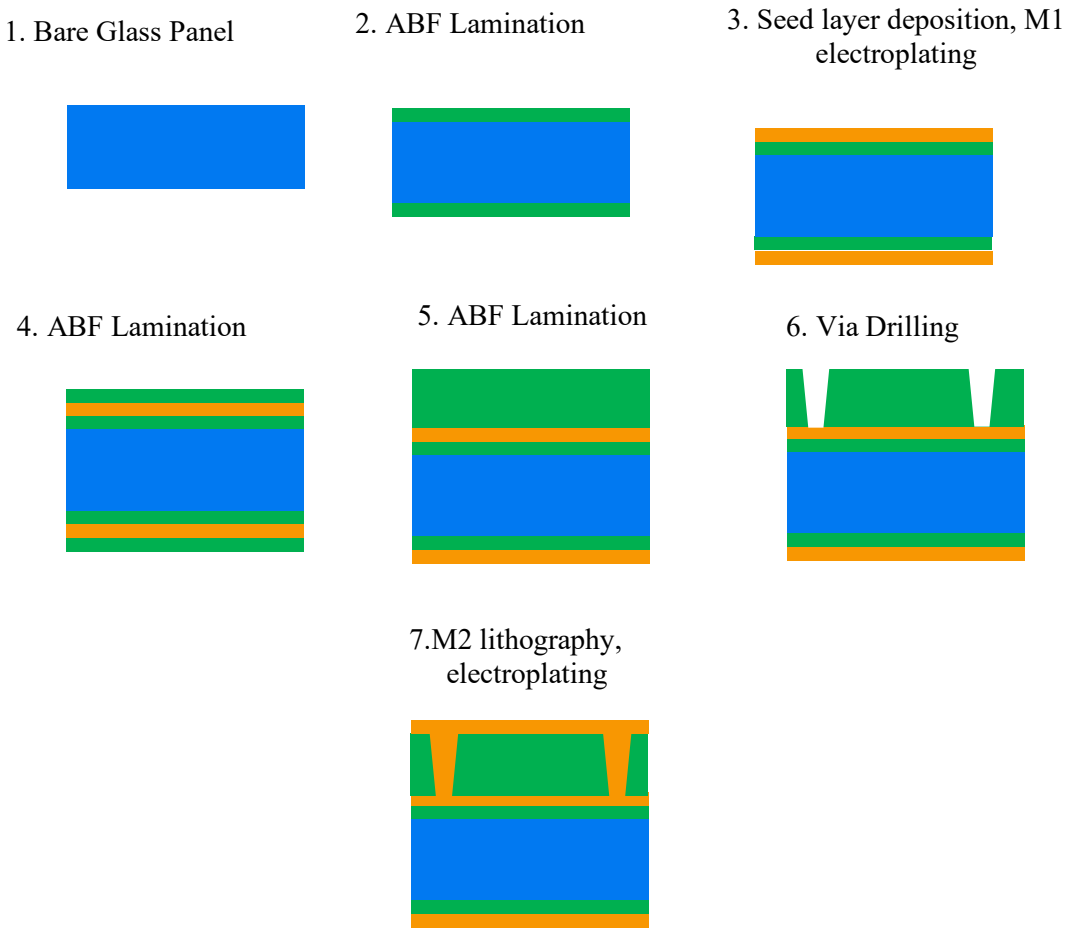

Figure 62 Process flow for fabrication

The fabricated sample and TRL structures for the microstrip line are given in Figure 63. TRL calibration will be used to move the reference plane so the effects of CBCPW probe pads, transitions and feed lines can be removed and response of 3.3mm long microstrip line can be de-embedded. The reference plane after TRL calibration is given in Figure 63.

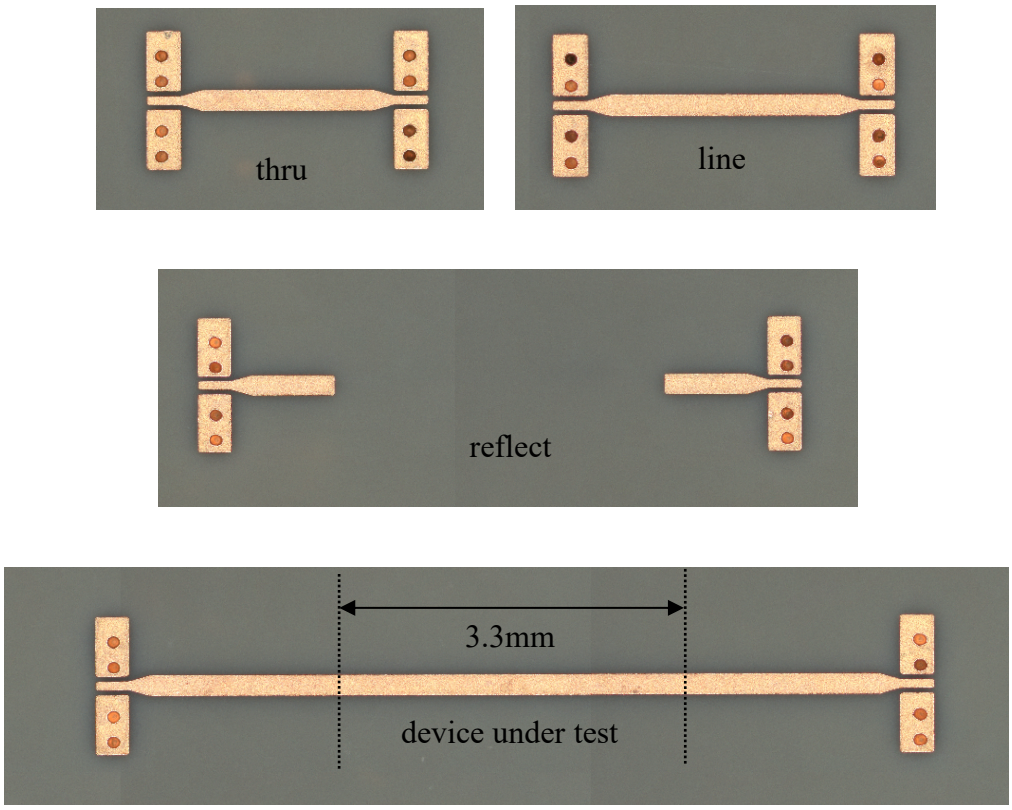

Figure 63 Fabricated sample and TRLs for microstrip line

The fabricated samples for SIWs are given in Figure 64. TRL calibration will be used to remove the effects of CBCPW probe pads, transitions, feed lines and microstrip taper and measure the response of 5mm long SIW section. The reference plane after TRL calibration is shown in Figure 64.

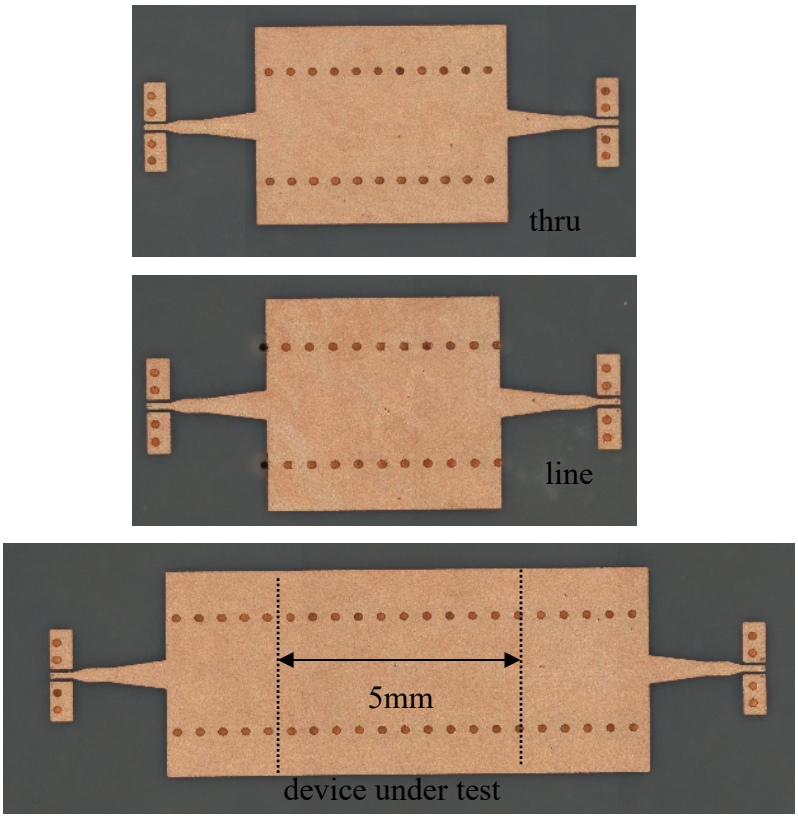

Figure 64 Fabricated sample of SIW and thru and line standard

6.3 Measurements

The designed samples were measured in D-band using Keysight VNA along with the D-band extenders and mmWave module. The samples were probed using Cascade Infinity probes. The sample on the probe station is shown in Figure 65. First, LRRM calibration was performed by using the calibration substrate and Wincal software provided by Cascade. Then the scattering parameters of microstrip and SIW samples were measured.

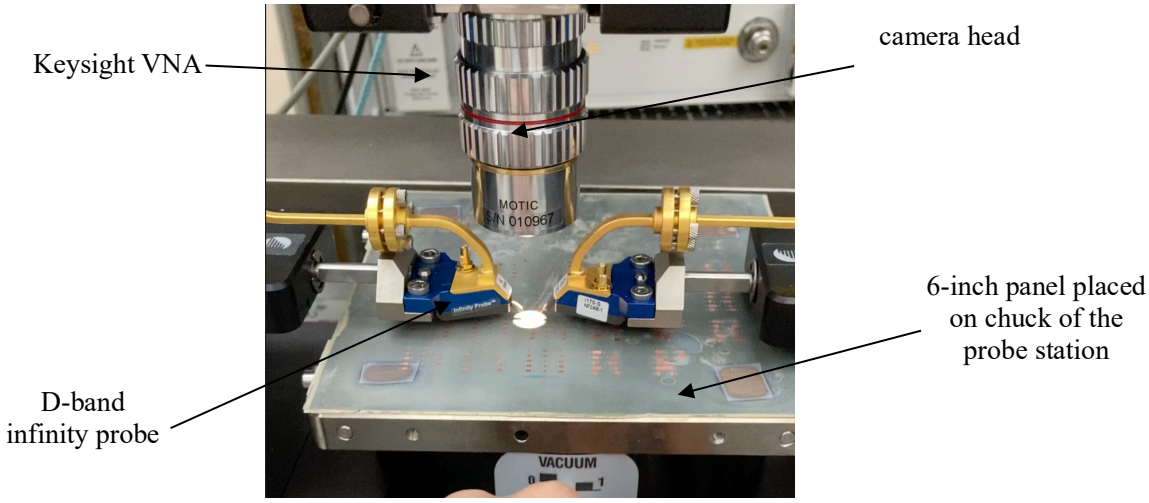

Figure 65 Sample on probe station for measurement

6.3.1 Microstrip lines

The measured scattering parameters, S_{11} (dB) and S_{21} (dB) for microstrip line and TRL structures are given in Figure 66a and Figure 66b respectively. These measurements were done after LRRM calibration, so they have the effects of CBCPW probe pads and transitions. The scattering parameter S_{11} (dB) for all the structures is approximately below -10 dB which implies good impedance matching and the scattering parameter S_{21} (dB) shows the effect of length in thru, line and device under test structure (3.3mm microstrip line) measurements. TRL calibration was performed using the measurements of thru, reflect and line standards.

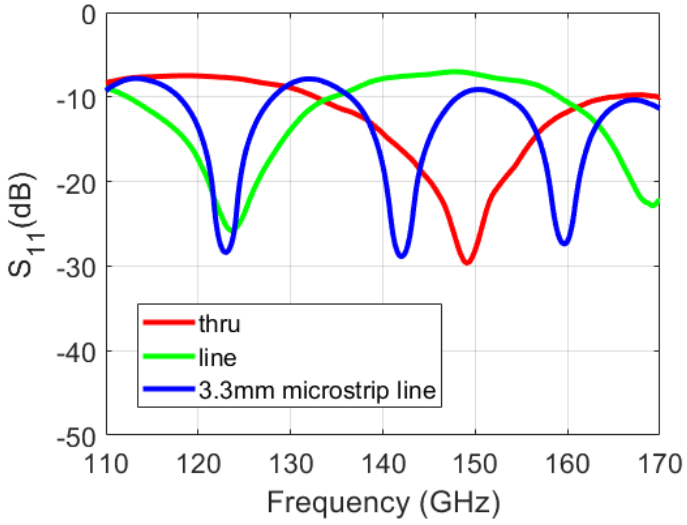

(a)

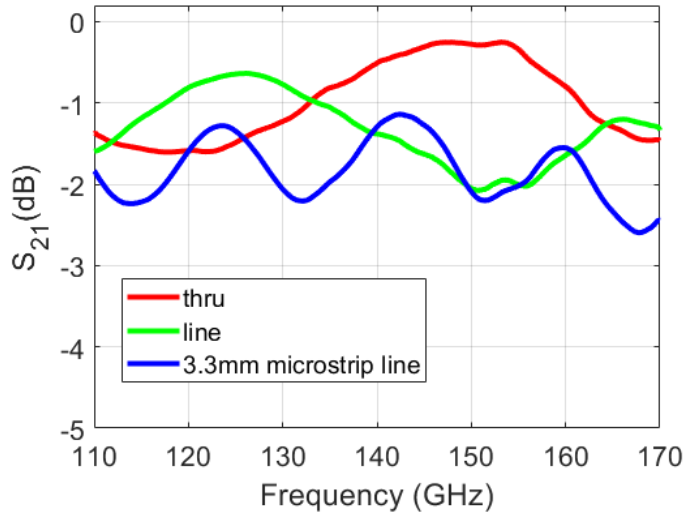

(b)

Figure 66 Measurements for microstrip line under LRRM calibration (a) S_{11} (b) S_{21}

The simulated and measured scattering parameters after TRL calibration are given in Figure 67. The measurement of thru structure after TRL calibration is given in Figure 67b. The thru standard is very close to 0 dB for the entire D-band (110 GHz to 170 GHz) which implies that the TRL calibration is accurate. After TRL calibration, the measured S_{11} (dB)

is below -20 dB for entire D-band and measured S_{21} (dB) varies from -0.55 dB to 1.1 dB from 110 GHz to 170 GHz. The average measured insertion loss in D-band is 0.825 dB. The measured results were compared with the simulations. The simulated and measured results are in excellent agreement.

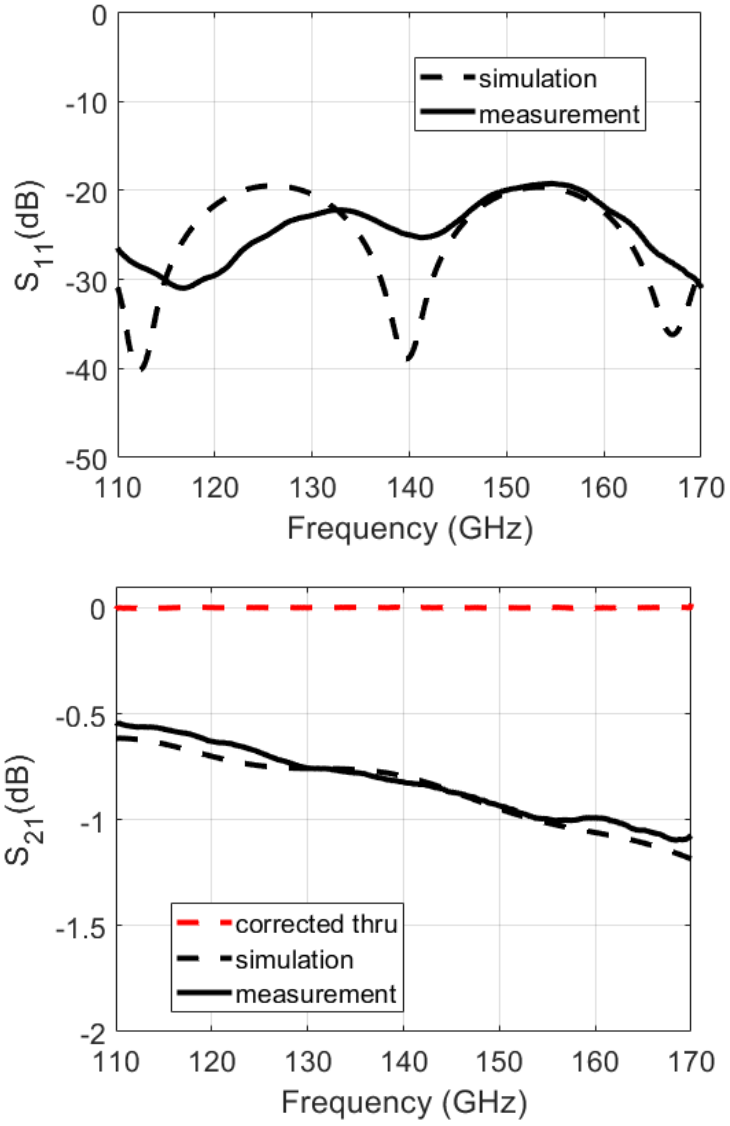

Figure 67 Measurements for microstrip line after TRL calibration (a) S11 (b) S21

6.3.2 SIWs

The measured scattering parameters of SIW thru, line and device under test structures are given in Figure 68. The scattering parameter S_{11} (dB) for all the structures is approximately below -10 dB which implies good impedance matching and the scattering parameter S_{21} (dB) shows the effect of length in thru, line and device under test structure (3mm long SIW) measurements.

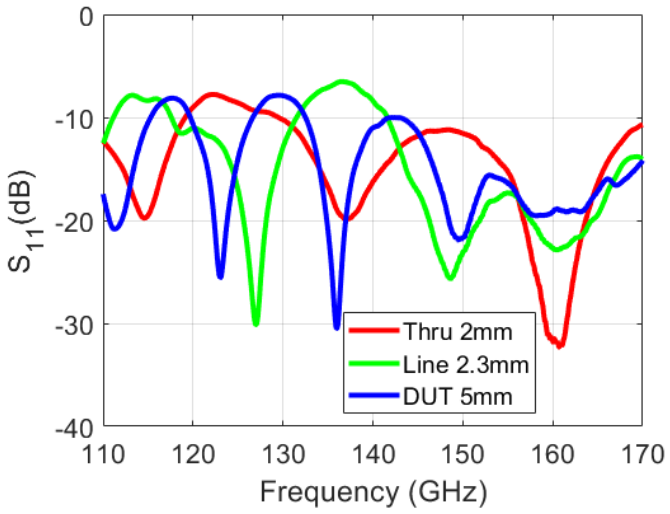

(a)

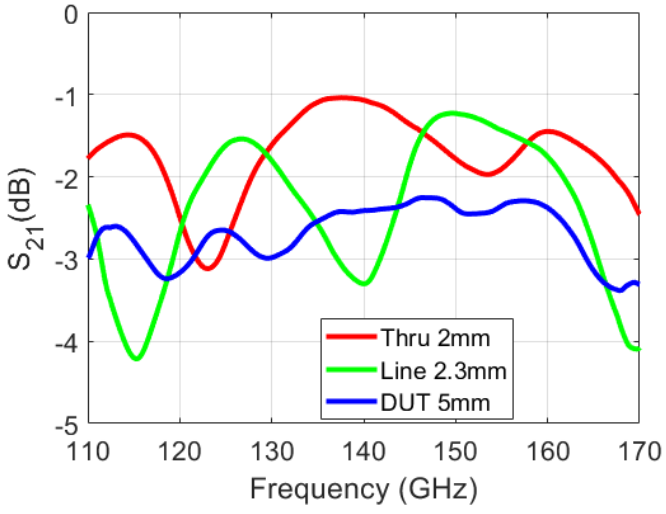

(b)

Figure 68 Measurements for SIWs under LRRM calibration (a) S11 (b) S21

TRL calibration was performed to move the reference plane as shown in Figure 64. The measured scattering parameters after TRL calibration are given in Figure 69. The measured S21 (dB) for thru standard after TRL calibration is given in Figure 69b. The average S21 (dB) for thru standard in D-band is 0.0097 dB which implies that the TRL calibration was accurate.

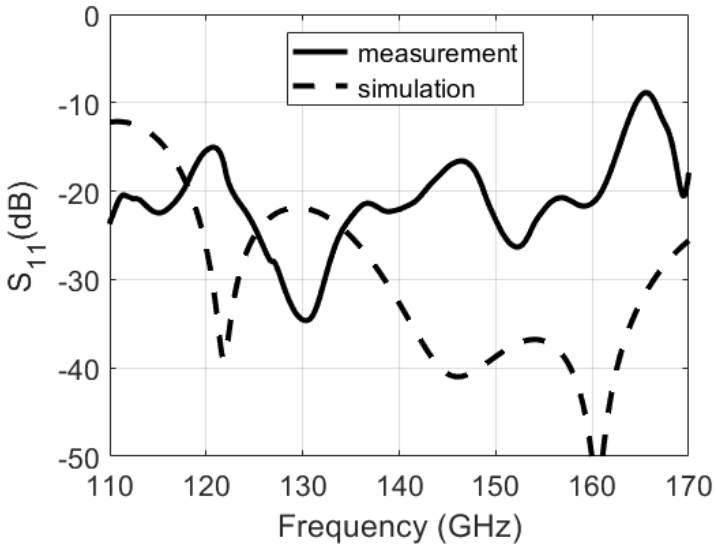

(a)

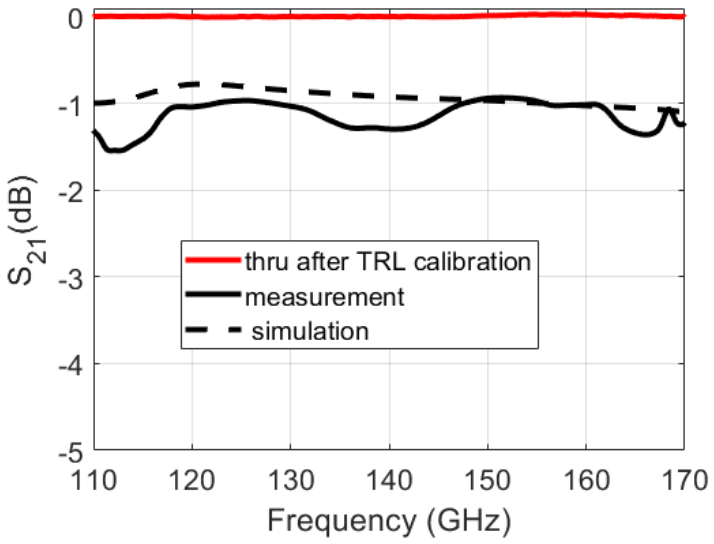

(b)

Figure 69 Measurements for SIWs after TRL calibration
(a) S_{11} (b) S_{21}

6.4 Performance Comparison

The performance of the designed microstrip line and SIW was compared with other interconnects designed on other state of the art materials. The performance of microstrip line was compared with LCP and ABF/glass/ABF material stack up (Chapter 2). The performance comparison is given in Figure 70. The measured insertion loss of ABF based microstrip line varies from .17 dB/mm to 0.33 dB/mm from 110 GHz to 170 GHz.

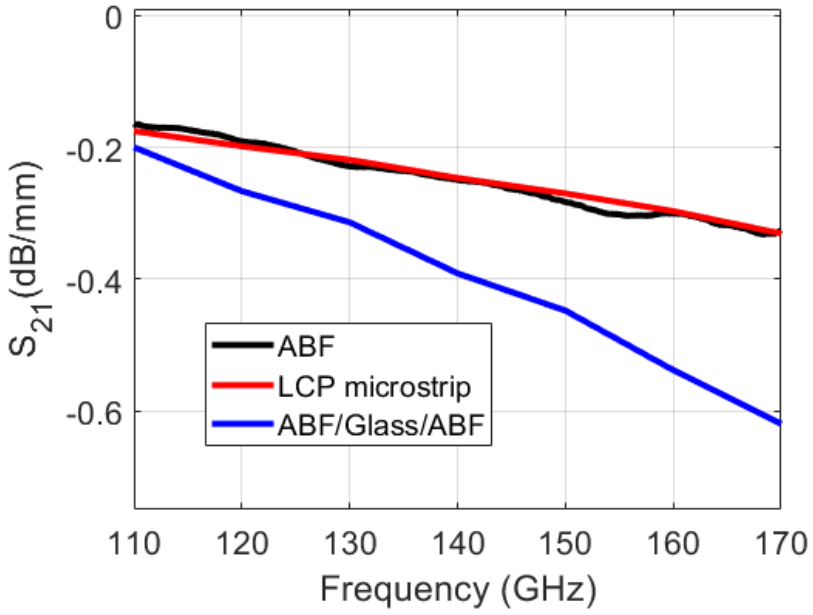

Figure 70 Performance of microstrip lines in D-band

The average insertion loss in D-band is 0.25 dB/mm. The performance is very close to LCP based microstrip line. The performance is significantly better as compared to ABF/glass/ABF based microstrip line. At 170 GHz, ABF based microstrip line has ~0.5x insertion loss (0.33 dB/mm) compared to ABF/glass/ABF (0.61 dB/mm). These results show loss budgets for making microstrip lines in glass interposer technologies using

different available layers. The performance of SIWs was compared with SIWs designed on LCP, high resistivity Silicon and ABF/glass/ABF material stack up. The performance comparison is given in Figure 71. The measured insertion loss for ABF based SIWs varies from 0.31 dB/mm to 0.51 dB/mm. The average insertion loss in D-band is 0.38 dB/mm. ABF based SIWs perform better than other candidates.

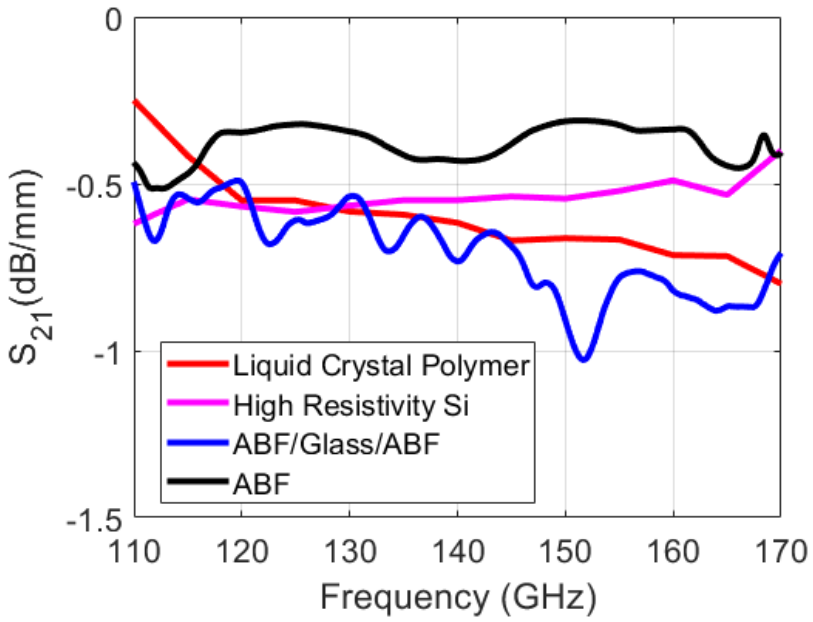

Figure 71 Performance comparison for SIWs in D-band

It is important to note that although LCP and ABF based SIWs show similar insertion loss in microstrip line, the insertion loss of ABF based SIW is less as compared to LCP based SIWs. This can be explained based on the role of surface roughness in the insertion loss of SIW. ABF based SIWs show ~0.5x insertion loss compared (0.38 dB/mm) to ABF/glass/ABF material stack up (0.72 dB/mm). These results show loss budgets for making SIWs in glass interposer technologies using different available layers.

CHAPTER 7. AIR FILLED SIWS IN D-BAND

The merits of SIW technology and its relevance for the development of sub-THz modules and the performance of SIW technology in glass interposers for D-band (110 GHz to 170 GHz) is described in Chapter 3. The insertion loss of the designed glass based SIWs was compared with other state of the art alternatives like Liquid Crystal Polymer (LCP)[24] and high resistivity Silicon [50]. These materials are used in three main interposer technologies namely Organic Interposer (LCP), Silicon Interposer (high resistivity Silicon) and Glass Interposer (ABF/glass/ABF). All these candidates exhibit moderate average insertion loss (>0.5 dB/mm) which motivates the development of ultra-low loss SIW technology. In this chapter, the Air Filled SIW technology will be presented which uses air cavities in a multi-layer laminate-based stack up to reduce the dielectric losses in SIW.

7.1 Loss mechanisms in SIWs

Before proceeding to the design of the ultra-low loss SIW technology it is important to understand the loss mechanism in SIW. There are three loss mechanisms in SIW namely radiation loss, ohmic loss and dielectric loss. Radiation loss occurs when the fields leak from the via side walls. Wave mechanisms and design considerations of SIW technology is described in detail in [48]. If the vias in the side wall are tightly placed according to the design rules, radiation loss is negligible. Ohmic loss is attributed to the finite conductivity of the metal. In addition to the bulk conductivity of the metal, surface roughness plays a critical role at frequencies above 100 GHz due to sub-micron skin depth. A surface roughness model for SIWs in D-band is presented in [78]. It has been reported in [24] that

an average 0.35dB/mm improvement can be done in the insertion loss of LCP based SIWs by polishing the root mean squared (rms) surface roughness from 0.35 μm to 0.17μm.

The dielectric loss in SIWs is attributed to the loss tangent of the material used. The material selection is challenging for high frequency applications because there are only a few candidates available and often low loss materials are expensive and they require sophisticated fabrication process.

7.2 Using Air Cavities

To reduce the dielectric loss in SIWs, air cavities in the material stack up can be used. Air, a lossless dielectric, replaces some of the lossy dielectric in the SIW which reduces the insertion loss. This approach is promising because by using ultra-low loss SIW technology can be developed using available laminate materials and existing fabrication processes. Air filled SIWs operating till 60 GHz using Rogers 5880 and Rogers 6002 materials were presented in [79] and compared to traditional dielectric SIWs, significant insertion loss reduction was achieved. The same technology was used to develop other SIW based passive components like filters, directional couplers and phase shifters [80-82].

In addition to the reduction in dielectric loss, air filled SIWs exhibit higher average power handling capability (AHPC), which makes this technology well suited for high power mmWave applications. However, peak power handling capability of (PPHC) of air filled SIWs is lower as compared to the dielectric filled SIWs which implies that air filled SIW technology is not well suited to support components with pulsed or modulated signals.

Using air cavities in a multi-layer laminate stack up, this chapter will present first results for Air Filled D-band (110 GHz to 170 GHz) SIWs. The performance of air filled SIWs will be compared with solid SIWs in the same material stack up to demonstrate the advantage of the proposed approach. The design details are given in the following sub-section.

7.3 Design Details

This sub-section will describe the material stack up, cut off frequency for solid and air filled SIWs, and transition design for feeding air filled SIWs.

7.3.1 Material stack-up

The material stack-up consisted of two 63.5 µm thick Isola Astra [83] laminate layers (named as layer #1 and layer #2) laminated together before 5 µm thick Ajinomoto Build up Film (ABF) GL102. The air cavities were drilled in Astra layer #2 whereas top copper layer was patterned on Astra layer #1. Bottom copper was supported on a 200 µm thick laminated glass (laminated with 15 µm thick ABF GL102). The material stack-up is given in Figure 72.

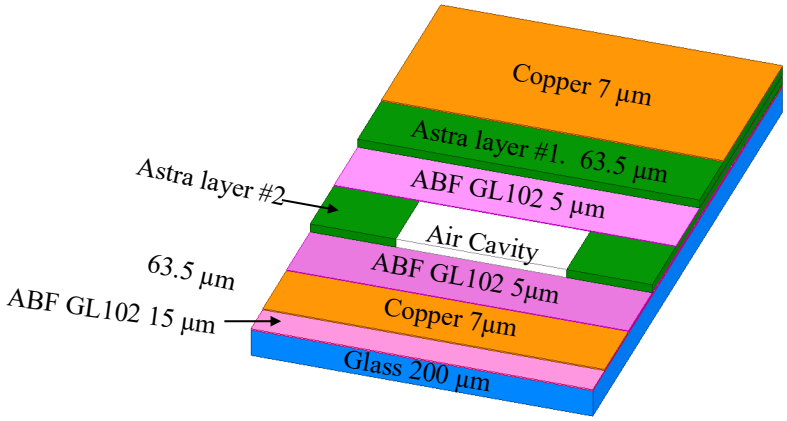

Figure 72 Material stack-up for air filled SIWs

7.3.2 SIW width design

Cut off frequency (f_c) of the fundamental mode (TE_{10}) in a typical SIW is determined by using following equation:

$$f_c = \frac{c}{2w\sqrt{\epsilon_r}}$$

where w is the width of SIW, ϵ_r is the dielectric constant of the substrate and c is the speed of light.

The above equation was used to estimate the width of SIWs and then simulation models were built using Ansys HFSS to tune the width for 90 GHz cut off frequency. Simulations were done to determine the widths for solid and air filled SIWs. Dielectric constant (ϵ_r) of Astra and ABF was modelled as 3.0 and 3.3 respectively. For ~90 GHz cut off frequency, the width of solid and air filled SIWs was 1.4 mm and 2.0 mm respectively. The diameter (d) and pitch (p) of the via side wall were designed to be 170 µm and 340 µm respectively.

7.3.3 Transition design

To feed the designed air filled SIW, solid-to-air SIW transition was designed. This transition had low insertion loss and good broadband performance. The transition from solid-to-air SIW was designed based on the basic for designing transition from high-to-low dielectric constant SIWs described in [84]. Due to presence of air cavity, the air filled SIW (2 mm) was wider than the solid SIW (1.4 mm). To make the transition both SIWs were connected and the via side wall was tapered from 2mm to 1.4mm width over a length of 1mm. This length was chosen to maintain the via diameter and pitch in the tapered

transition. Then the shape of the air cavity was also tapered in the transition region between the solid and the air filled SIW. The transition was simulated with different cavity taper lengths from 0 µm to 1000 µm to choose the best design. The simulated structure consists of two 1 mm long transitions and 1 mm air filled SIW section (total 3mm). The cavity with different taper lengths and simulated scattering parameters are given in the figure below.

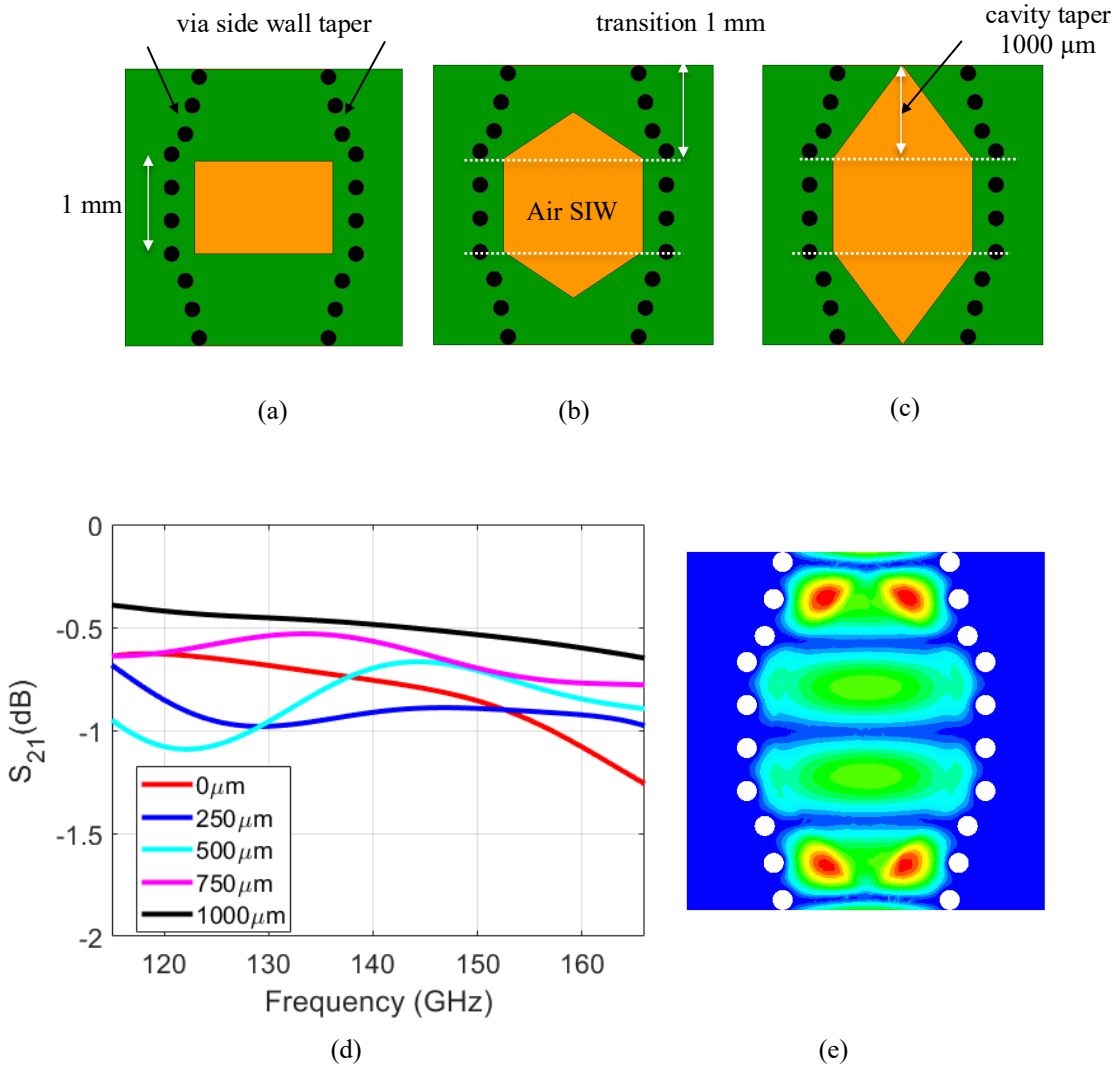

Figure 73 Solid-to-Air SIW transition design (a) no taper in air cavity (b) 500 µm taper air cavity (c) 1000 µm taper air cavity (d) S_{21} vs Freq for 3mm long section with different cavity tapers (e) E-field in transition

The transition with 1000 µm long cavity taper was selected due to its low insertion loss and stable performance across entire D-band.

7.3.4 GCPW to SIW transitions

To probe the designed samples, Grounded Coplanar Waveguide (GCPW) to SIW transitions were designed with tapered coupling slots. The tapered coupling slots were chosen due to achieve wideband impedance match between arbitrary impedance of SIW and the impedance of GCPW [85]. The designed GCPW to SIW transition is given in Figure 74a. The GCPW probe pads were designed to be consistent with 75µm pitch of Cascade infinity probes. The GCPW probe pad is shown in Figure 74b. To de-embed the response of the SIW section, TRLs were designed for both solid and air filled SIWs.

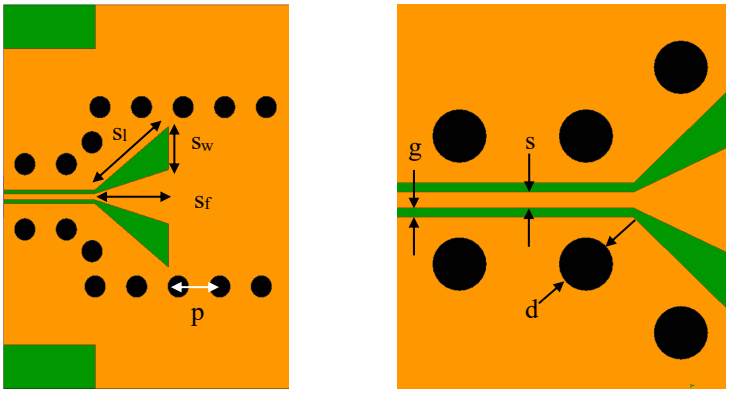

(a) (b)

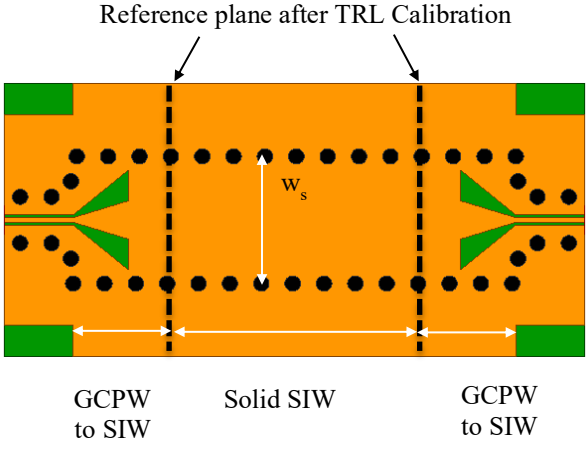

(c)

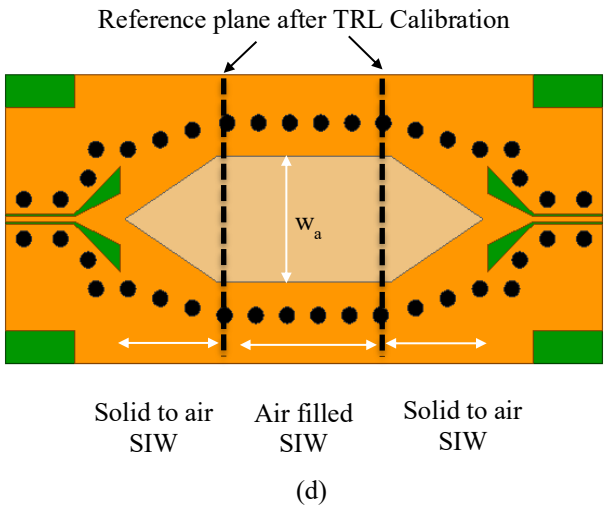

Figure 74 Design of test vehicle (a) GCPW to SIW transition (b) GCPW probe pad (c) solid SIW with GCPW feed (d) air filled SIW with transitions and GCPW feed

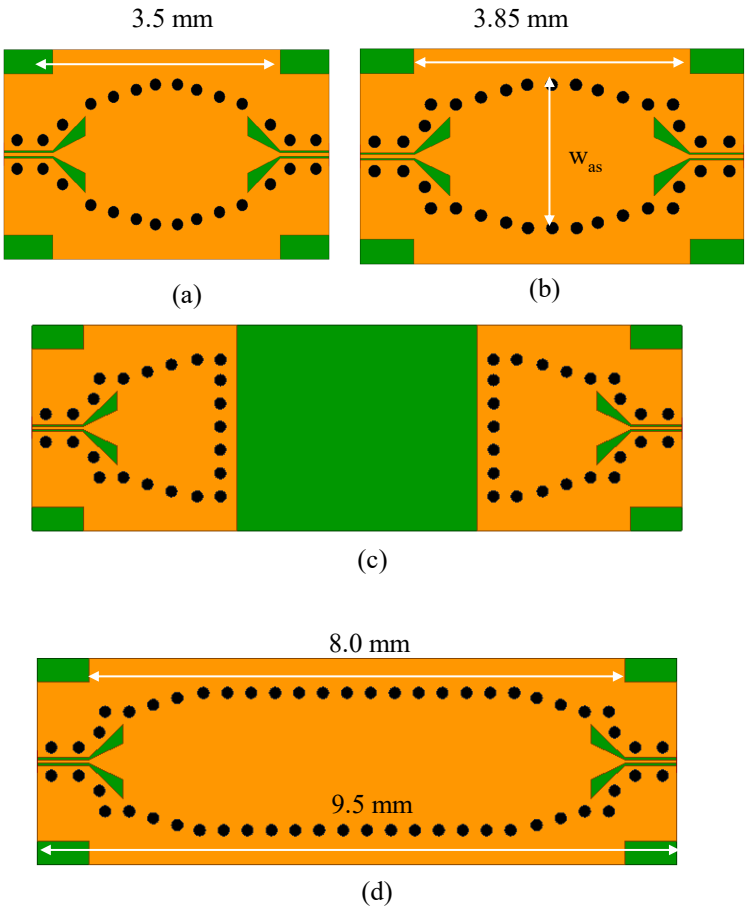

Figure 75 TRL kit for Air Filled SIWs (a) thru (b) line (c) reflect (d) device under test (DUT)

Table 11 Physical parameters of the air filled SIW test vehicle (µm)

Structure	Parameter	Designed	Measured	Change %
Solid SIW	w_s	1400	1403	0.21
	l_s	4500	4509	0.2
Air SIW	w_a	1300	1312	0.92
	w_{as}	2000	1992.8	0.36
	l_{as}	4000	4008	0.2
GCPW to SIW transition	s_w	283	287	1.41
	sf	500	511	2.2
	sl	703.5	707.4	0.55
GCPW probe pad	s	50	45.2	9.6
	g	30	34.6	15.3
All	d	170	172.3	1.35
	p	340	345.7	1.67

7.4 Fabrication

In the first step cavities were drilled in Astra panel using Optec Femtosecond laser tool. Next, 5 µm thick ABF GL102 film was vacuum laminated on both sides of the panel at 70° C using Meiki Vacuum Laminator. The recommended temperature for ABG GL102 lamination was 100° C but it was observed in process development that laminating the ABF

thin films at 100° C in step1 resulted in poor adhesion with the top Astra layer in the step 6. Delamination due to the use of 100°C in the step 1 is shown in Figure 76a. To solve this problem, lower temperature was used in the first lamination and the polymer film was not cured after this step. The protective film was peeled off and air gun was used to remove the polymer from both sides of the cavity as shown in the 4th step of the process flow. This step was done to ensure that the air cavity remains vacant because otherwise the polymer from the top can flow inside during curing stages as shown in Figure 76b.

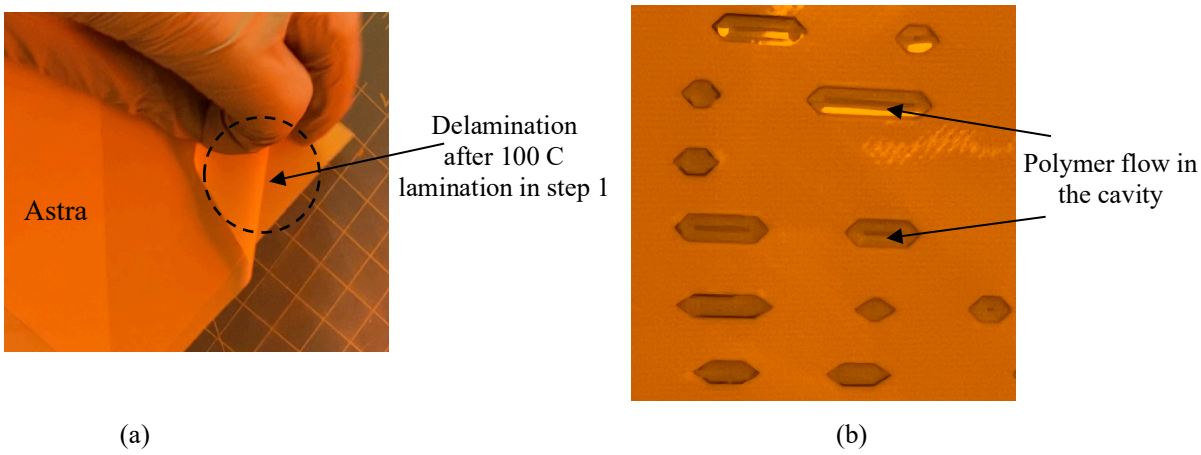

Figure 76 Challenges in fabrication (a) delamination (b)polymer flow

To support the whole stack up, 200 µm thick glass was used. 15 µm thick ABF GL102 was vacuum laminated on the glass core. Then 7 µm thick bottom copper layer was deposited on the laminated glass core by electroless copper deposition followed by electroplating. Then three parts 1) Astra top 2) laminated Astra with drilled cavities and 3) bottom copper on laminated glass, were laminated together as shown in the 6th step of the process flow. Then the material stack up was cured at 130°C for 30 mins and then at 170°C for 30 mins.

Then vias were drilled in the stack up using Optec Femtosecond Laser Tool. The via drilling was challenging because of the use of different materials in the polymer stack up. Test drills were performed varying different parameters like laser power, laser speed, jump speed and frequency and the profiles of the test vias were observed using Keyence Optical Profiler. The recipe with 27% laser power, 2 repetitions, 150 mm/sec jump speed and 8µm vertical drill step gave the best results. The optical scans and profiles of the test vias are given in Figure 77.

Next, 0.4 µm thick copper seed layer was deposited using electroless copper deposition. Next, 15 µm thick dry film photoresist (Hitachi RY5115) was vacuum laminated on the seed layer using Meiki Vacuum Laminator at 80° C. Then the photoresist was exposed using Heidelberg Maskless Aligner. After exposure, the panel was processed through photoresist developer. Then, copper was deposited to 7 µm by electroplating and then the photoresist was stripped. Then the panels were kept in a nitrogen oven for 60 mins at 170° C to anneal the electroplated copper. In the last step, seed layer was etched using differential etching. The fabrication process is given in Figure 78.

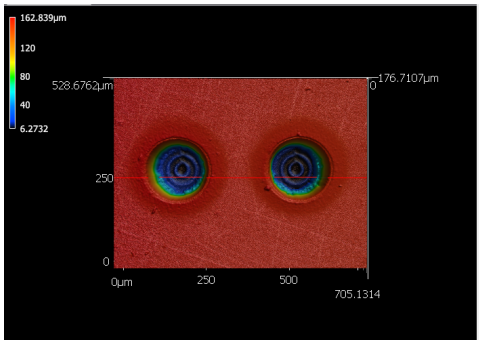

(a)

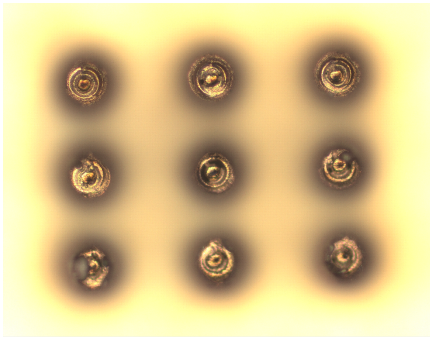

(b)

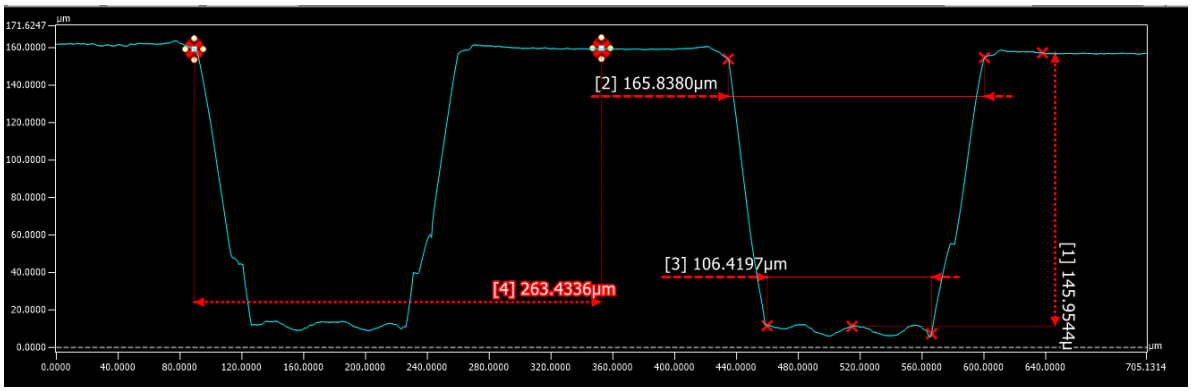

(c)

Figure 77 Via drilling
(a) depth scan (b) bottom copper (c) taper scans

The fabricated samples were examined using Keyence Optical Profiler and physical dimensions of the fabricated structures were measured. There was ~5 to 6 µm reduction in the fabricated line widths. This can be attributed to various factors like exposure time, development rate and etching rate in the differential etcher which are difficult to precisely control. 50µm wide signal line in the GCPW was reduced to 45.2 µm and 30µm gap increased to 34.6 µm. The fabricated dimensions were included in the simulation models to account for any changes in the response. Since the effects of GCPW to SIW transitions were to be eliminated after TRL calibration, this change in fabricated dimensions was not a cause of concern. The fabricated widths of solid and air SIWs were very close to the designed values. The rms surface roughness was measured on different samples. The measured rms surface roughness varied from 150 nm to 220 nm with most of the readings closer to 200 nm. The fabricated samples are given in Figure 79.

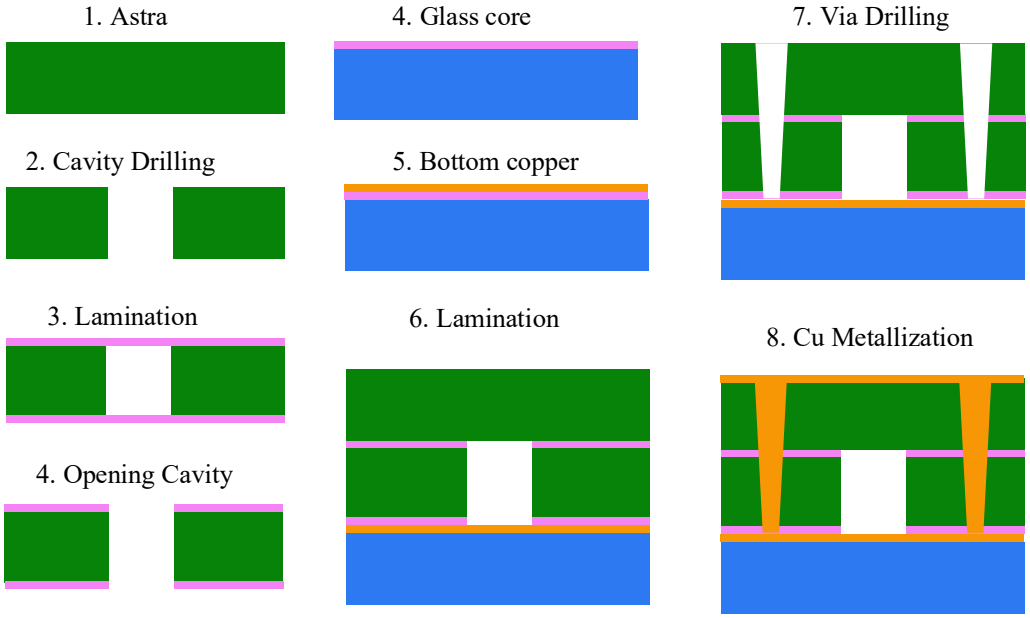

Figure 78 Process flow for fabrication

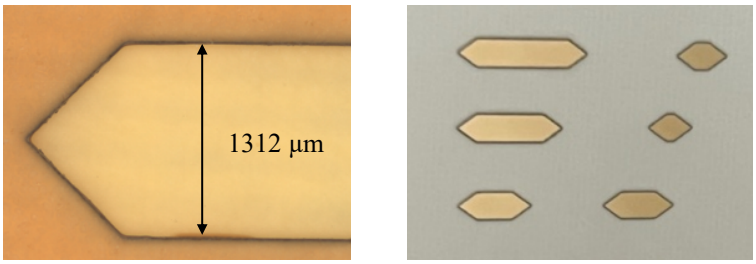

(a)

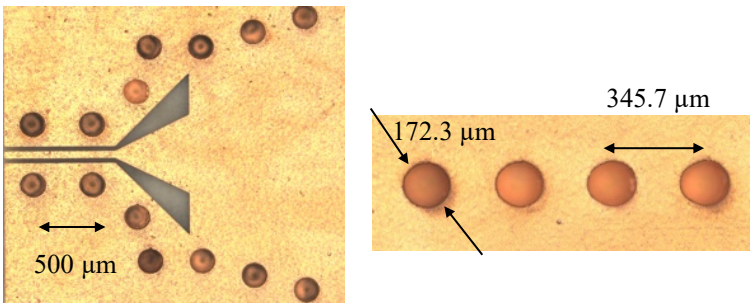

(b) (c)

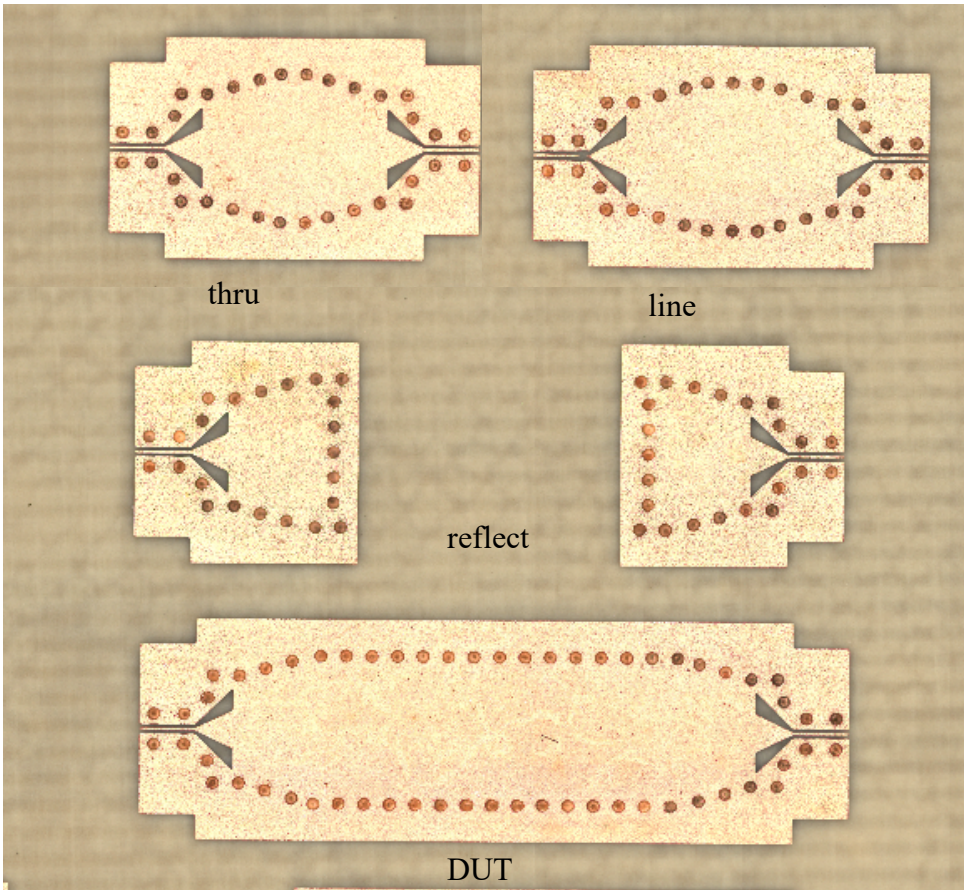

(d)

Reference plane after
TRL Calibration

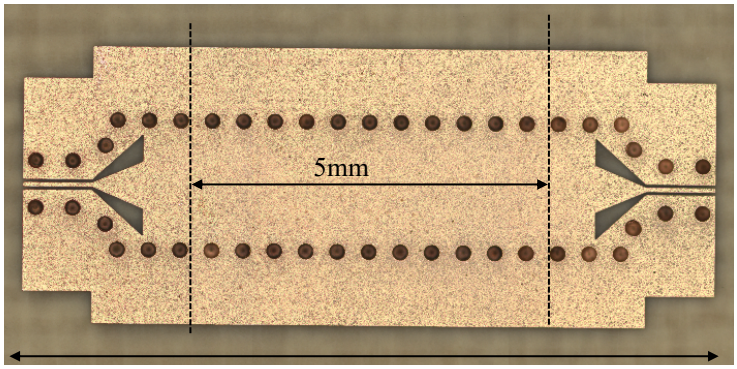

9.5mm

(e)

Reference plane after TRL Calibration

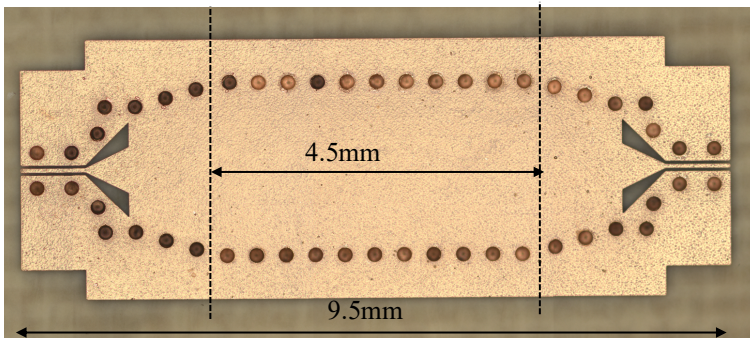

(f)

Figure 79 Fabricated Samples (a) drilled air cavities in Astra (b) CBCPW to SIW transition (c) SIW via side wall (d) coupon containing air filled SIWs with TRL (e) solid SIW (f) air filled SIW

7.5 Measurements

The S-parameters of the solid and air filled SIWs were measured in D-band (110 GHz to 170 GHz) using Keysight Vector Network Analyzer (E8361C) along with mmWave module and D-band frequency extenders (V06VNA2). The samples were probed using Cascade Infinity Probes (170-S-GSG-75-BT). The pitch of the RF probes was 75 µm. Two tier calibration was used to measure the scattering parameters of solid and air filled SIWs. In the first step, LRRM calibration was performed using Wincal software and calibration substrate by Cascade. LRRM calibration moves the reference plane to the edge of the probe tips. The measurements under LRRM calibration are given in Figure 80. The measured scattering parameters S_{11} (dB) and S_{21} (dB) for solid SIWs are given in Figure 80a and Figure 80b respectively. These measurements have the effects of GCPW to SIW transitions.

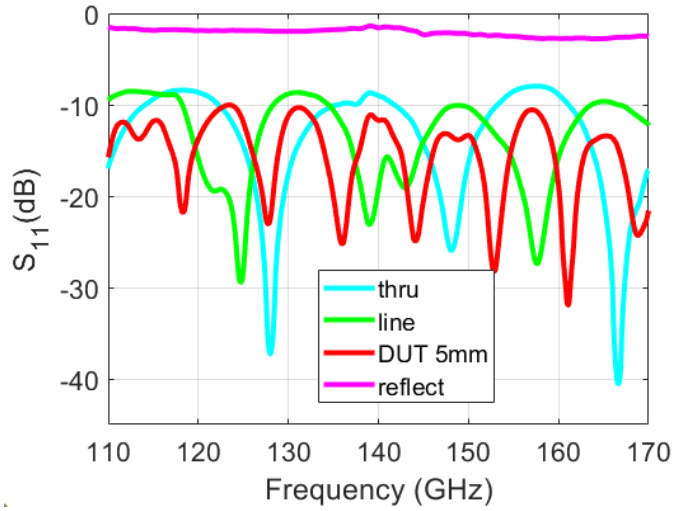
0
-10
-20
-30
-40
S_{11}(dB)
110
120
130
140
150
160
170
Frequency (GHz)
thru
line
DUT 5mm
reflect

(a)

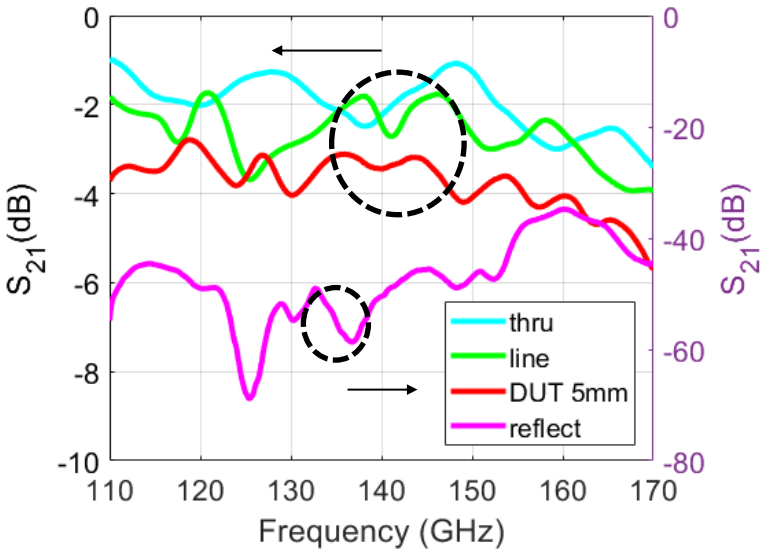
0
-2
-4
-6
-8
-10
S_{21}(dB)
0
-20
-40
-60
-80
S_{21}(dB)
110
120
130
140
150
160
170
Frequency (GHz)
thru
line
DUT 5mm
reflect

(b)

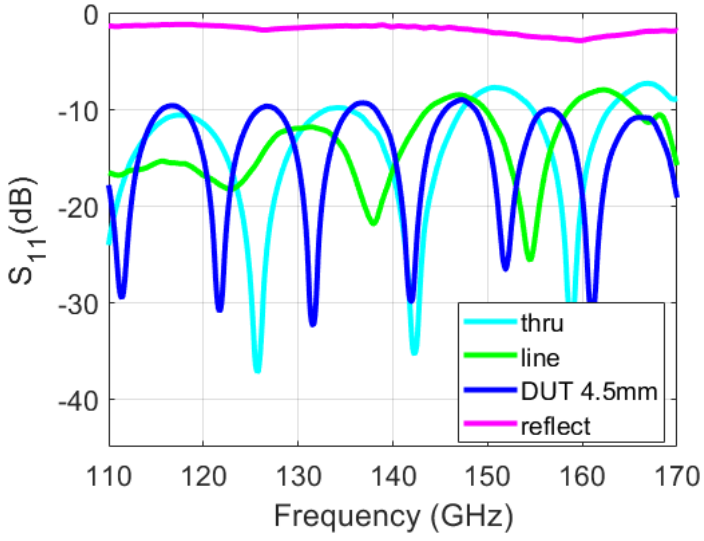
0
-10
-20
-30
-40
S_{11}(dB)
110
120
130
140
150
160
170
Frequency (GHz)
thru
line
DUT 4.5mm
reflect

(c)

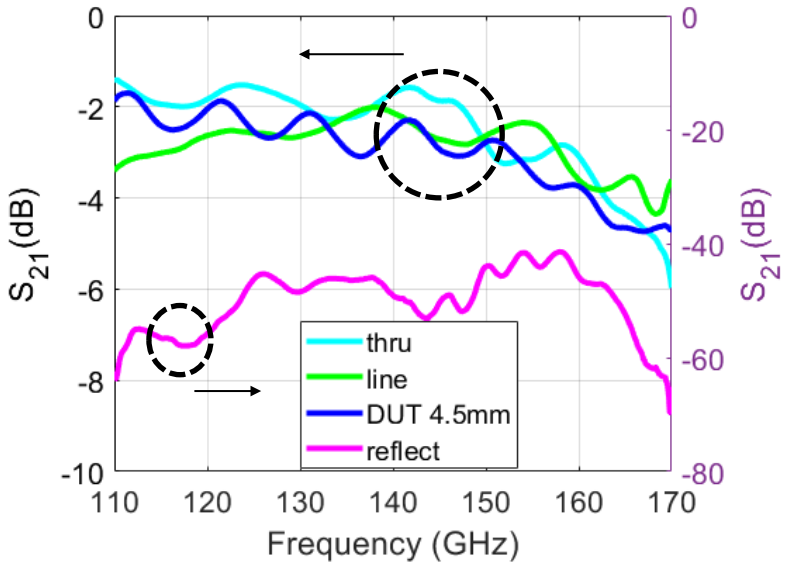

(d)

Figure 80 Scattering Parameters for the TRL structures for the designed SIWs after LRRM calibration (a) S_{11} for solid SIWs (b) S_{21} for solid SIWs (c) S_{11} for air filled SIWs (d) S_{21} for air filled SIWs

The measure responses of thru, line and reflect structures will be used perform TRL calibration to de-embed the response of 5mm long solid SIW section. The reference plane after TRL calibration for solid SIW is shown in Figure 79e.The measured scattering parameters S_{11} (dB) and S_{21} (dB) for air filled SIWs are given in Figure 80c and Figure 80d respectively. These measurements have the effects of GCPW to SIW transitions and solid-to-air SIW transitions. The measurements of thru, line and reflect structures will be used to perform TRL calibration to de-embed the response of 4.5mm long air filled SIW section. The reference plane for air filled SIWs after TRL calibration is shown in Figure 79f. Before proceeding to TRL calibration, the simulated and measured scattering parameters of 9.5mm long solid and air filled SIWs (including transitions) were compared. The 9.5mm long solid and air filled SIWs are shown in Figure 79e and Figure 79f respectively. The simulated and measured scattering parameters are given in Figure 81. The measurements have decent

agreement with the simulated results. S11 (dB) is less than -10 dB for almost entire D-band (110 GHz to 170 GHz). For 9.5mm long solid SIW (with transitions) the measured insertion loss varies from 2.81 dB to 5.67 dB with an average insertion loss of 3.74 dB in D-band. For 9.5mm long air filled SIW (with transitions) the measured insertion loss varies from 1.7dB to 4.7 dB with an average measured insertion 2.96 dB for D-band. For a 9.5mm long interconnect (including transitions), air filled structures exhibit ~21% less loss. It is important to note that this comparison is for the entire structure including the effect of transitions.

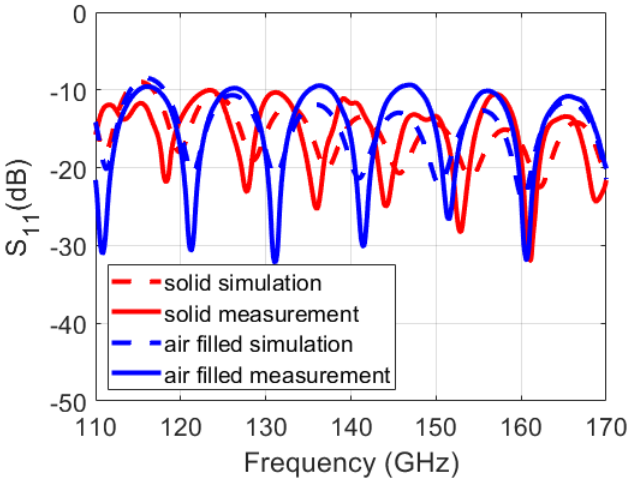

(a)

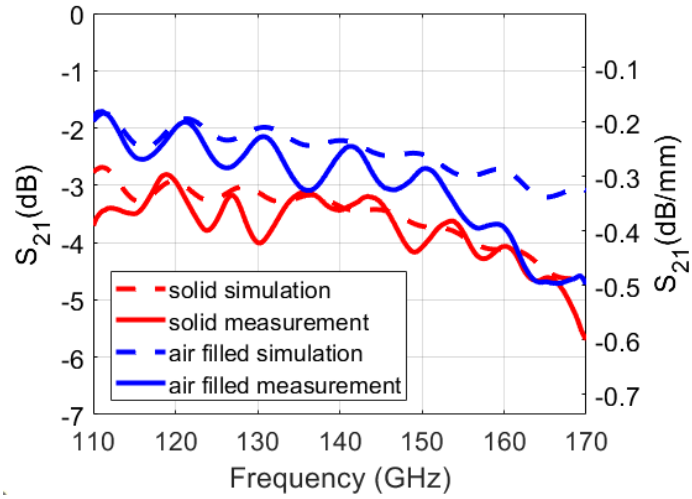

(b)

Figure 81 Measured and simulated S-parameters after LRRM calibration (a) S_{11} (dB) (b) S_{21} (dB)

The per unit insertion loss (dB/mm) for solid and air filled SIWs (including transitions) is given in Figure 81b. The solid and air filled SIWs show insertion loss of 0.37 dB/mm and 0.3 dB/mm respectively.

To remove the effects of transitions, TRL calibration was performed on both solid and air filled SIWs. The reference planes after TRL calibration are given in Figure 79e and Figure 79f. After doing TRL calibration, thru structures were measured for both solid and air filled SIWs. The measured scattering parameters (S_{21}) for thru structures after TRL calibration are given in Figure 82a. For most of the frequency region, the insertion loss varies between -0.05 dB to 0.05 dB shows that the TRL calibration was accurate as it removed the effects of transitions. At the edges of D-band (around 110 GHz and 170 GHz), the error was slightly above 0.05 dB. Due this slightly higher error at the edges of D-band, the results after TRL calibration were reported from 113 GHz to 168 GHz. The simulated and measured scattering parameters for 5mm long solid and 4.5 mm long air filled SIW section are given in Figure 82b and Figure 82c respectively. The simulated results are in good agreement with the measurements. After TRL calibration, S11 (dB) is well below -10 dB for the entire frequency region which shows good matching. 4.5 mm long solid SIW varies from 1 dB to 2.5 dB with an average of 1.7 dB. The measured insertion loss for 5mm long solid SIW varies from 1 dB to 2.5 dB with an average of 1.7 dB. The measured insertion for 4.5mm long air filled SIW varies from 0.17 dB to 0.98 dB with an average of 0.6 dB. The simulated and measured per unit S_{21} (dB/mm) for solid and air filled SIW is given in Figure 82d.

The solid SIW shows an average insertion loss of 0.36 dB/mm whereas air filled SIW shows an average insertion loss of 0.16 dB/mm. Using air cavities in the material stack up results in 0.2 dB/mm insertion loss improvement. This significant (~56%) reduction in insertion loss shows the potential of multilayer laminated based air filled SIW technology for making ultra-low loss interconnects for supporting sub-THz modules.

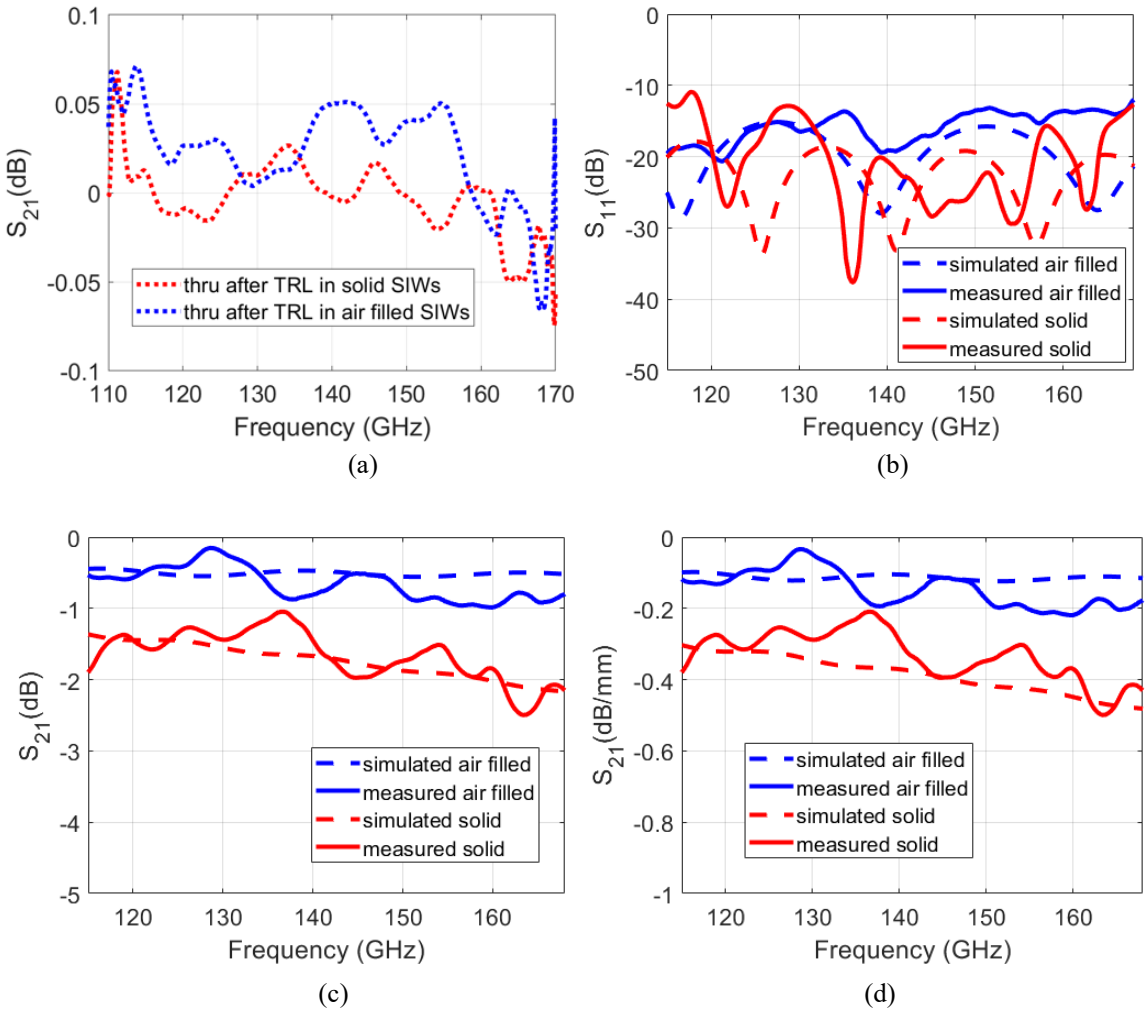

Figure 82 Simulated and measured S-parameters after TRL calibration (a) measured thru structures (b) S_{11} (dB) (c) S_{21} (dB) (d) S_{21} (dB/mm)

7.6 Performance Comparison

The performance of the solid and air filled SIWs was compared with the other SIWs operating above 100 GHz reported in literature. The other candidates have been fabricated using Liquid Crystal Polymer (LCP), High Resistivity Silicon, Silicon Carbide (SiC) and air filled SIWs using photo-imageable glass. The performance will also be compared with SIWs in glass interposer technology presented in Chapter 3. The per unit S21 (dB/mm) is given in Figure 83. The proposed multilayer Astra based air filled SIWs perform better than solid SIWs made in other materials. The air filled SIWs fabricated using photo-imageable glass [86] show slightly better insertion loss (0.12 dB/mm) than the proposed Astra based air filled SIWs (0.16 dB/mm). This slight difference in insertion loss is due to different materials and sophisticated fabrication process. In multilayer Astra based air filled SIW, the air is introduced in only one of the two laminate layers because the top layer is required to support the top metal layer. Therefore, the entire SIW is not air filled with air. The use of photo-imageable glass allows to completely etch the glass within the SIW after the metal deposition. This results in a completely air filled SIW which can achieve lower insertion loss. The average insertion loss (dB/mm) for the Astra based solid and air filled SIWs are compared with the other candidates in Table 12. It is important to note that the substrate height is different for the SIWs enlisted in Table 12 which makes insertion loss comparison difficult. Multilayer Astra based solid SIWs show average insertion loss of 0.36 dB/mm in D-band which is better than SIWs fabricated using LCP, high resistivity Silicon and ABF/glass/ABF stack up. This shows the low loss performance of Astra and its suitability for mmWave and sub-THz applications. The ~56% reduction is insertion loss was achieved by using air cavities in the material stack-up.

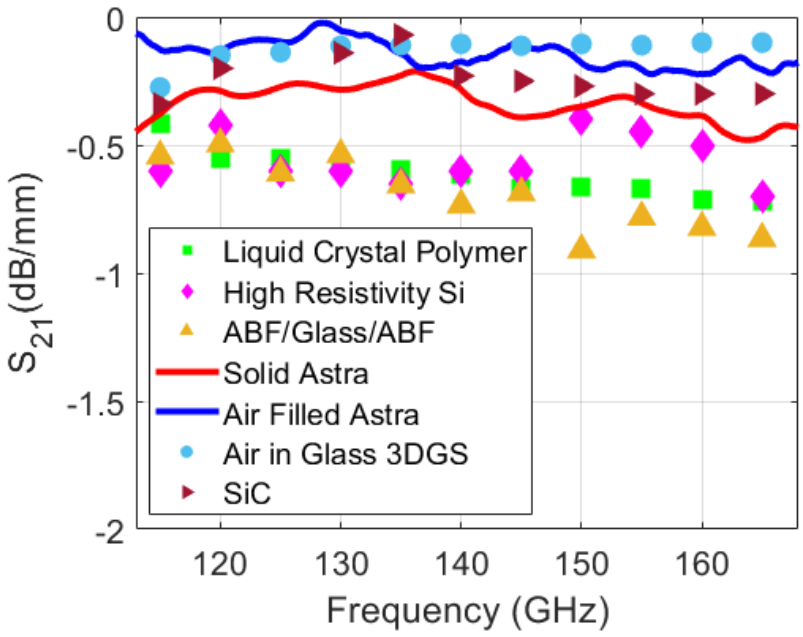

Figure 83 Per unit insertion loss (dB/mm) for D-band SIWs

Table 12 Per unit insertion loss for state-of-the-art SIWs in D-band

Ref	Material	Substrate height (μm)	Average IL (dB/mm)
[24]	Liquid Crystal Polymer	50.8	0.68
[50]	High Resistivity Silicon	70	0.55
[28]	ABF/glass/ABF	130	0.7
[51]	Silicon Carbide (6H-SiC)	100	0.22
[86]	Air (photo imageable glass)	NA	0.12
This Chapter	Astra (multilayer)	137	0.36
	Air Filled Astra (multilayer)	137	0.16

CHAPTER 8. SUMMARY AND FUTURE WORK

8.1 Dissertation Summary

This thesis contributes to the development of glass interposer technology for sub-THz frequency region by providing the first electrical characterization results for ABF/glass/ABF material stack up and by benchmarking the performance of RF interconnects (microstrip lines, CPWs and SIWs) in glass interposers. This thesis also presents the design and demonstration of Novel Blind Via Filter Technology for making miniaturized SIW filters for mmWave frequency region. We have also developed Air Filled SIW technology using multi-layer laminate stack up to design ultra-low loss SIWs in D-band (110 GHz to 170 GHz). The contributions of this thesis as presented in each chapter are given below

Chapter 1 presented the need of carrier frequencies above 100 GHz to support the next generation wireless systems, gave a brief comparison of the existing packaging technologies and outlined their limitations for supporting next generation wireless modules. It highlighted the salient features of glass interposer technology and featured it as a possible candidate to support sub-THz modules due to its unique ability to support ultra-fine pitches at low cost.

Chapter 2 presented the first electrical characterization results for ABF/glass/ABF material stack up from 20 GHz to 170 GHz using microstrip ring resonator (MRR) method. This chapter also presented design, fabrication, and measurements for microstrip lines and CPWs on the same material stack up for the same frequency region. The measured results

of interconnects (microstrip lines and CPWs) were used to validate the extracted material properties. The performance of interconnects was also compared with other state of the art candidates. This chapter also highlighted challenges related to design, fabrication, and measurements for D-band samples. It discussed and presented solutions for the limitations of via-less CBCPW to microstrip probe pads at low frequencies and sensitivity of D-band probes to the variation in height of RF probe pads due to electrolytic plating.

Chapter 3 highlighted the merits of SIW technology for mmWave frequencies and presented the first demonstration of SIW technology in glass interposers. SIWs in glass interposers show an average measured insertion loss of 0.72 dB/mm in entire D-band. It also compared the performance with SIWs fabricated on LCP and high resistivity Silicon.

Chapter 4 presented the first demonstration of SIW cavity filters in glass interposers and compared its performance with other state of the art filters. Two different shaped (square and rectangular) SIW cavities were used to design the SIW filters, and the response was compared. Rectangle shaped SIW cavity filters shown better rejection in the higher stop band compared to square shaped SIW cavity filters. However, for a same order, rectangular filters are 20% larger in size compared to square filters. This chapter also discussed the importance of precise control on via diameters (in SIW cavity side wall) in fabrication to achieve the desired center frequency and presented an example in which changing the via diameters in the side walls caused ~18 GHz shift in the measured center frequency.

Chapter 5 presented a new filter design type named Blind Via filters. This structure uses a blind via as a reactive load in the SIW section to create a filter response. This chapter has two parts. In the first part, blind via filters were designed using the same material stack-up

(ABF/glass/ABF) as in previous chapters but in the fabrication stage and after measuring the scattering parameters, it was concluded that drilling blind vias in polymer with precise depth control was very difficult and this limitation can be overcome by using a via stop layer. This was not possible in the old material stack up because it only provided two metal layers. This led to the use of a new three metal layer material stack up in the second part of this chapter. Blind Via Filters were designed and fabricated on the new stack up. To compare the performance with the traditional SIW filters, SIW cavity-based filters were also designed and fabricated using the new material stack up. For a similar passband performance, blind via filters were only a third of the size of the traditional SIW filters.

Chapter 6 presented the performance of microstrip lines and SIWs on the new material stack up introduced in the previous chapter. The aim of this activity was to evaluate the performance of these RF interconnects in different materials within the glass interposer technology. The measured insertion loss of ABF based microstrip line varied from .17 dB/mm to 0.33 dB/mm from 110 GHz to 170 GHz. The measured insertion loss for ABF based SIWs varied from 0.31 dB/mm to 0.51 dB/mm.

Chapter 7 presented Air Filled SIW technology for making ultra-low loss interconnects in D-band (110 GHz to 170 GHz). This chapter used a multi-layer Astra laminate stack up supported on a glass core to make low loss SIWs by introducing air cavities in the material stack up. To compare the performance, solid SIWs were also designed and fabricated using the same material stack up. The solid SIW shown an average measured insertion loss of 0.36 dB/mm whereas air filled SIW shown an average measured insertion loss of 0.16 dB/mm. Using air cavities in the material stack up resulted in 0.2 dB/mm insertion loss improvement. This significant (~56%) reduction in insertion loss shows the potential of

multilayer laminated based air filled SIW technology for making ultra-low loss interconnects for supporting sub-THz modules.

8.2 Publications

The work done in this thesis has resulted in the following publications

8.2.1 Journal Articles

1. **Mutee ur Rehman**, Lakshmi Narasimha Vijay Kumar, Serhat Erdogan and M. Swaminathan, "Air Filled SIWs in D-band for mmWave Applications," submitted in *IEEE* Transactions on Components, Packaging and Manufacturing Technology *(under review)*

2. **Mutee ur Rehman**, Lakshmi Narasimha Vijay Kumar and M. Swaminathan, "Novel Blind Via Filters for mmWave Applications" submitted in *IEEE* Transactions on Microwave Theory and Techniques *(under review)*

3. **Mutee ur Rehman**, Lakshmi Narasimha Vijay Kumar and M. Swaminathan, "Characterization on Transmission Lines and SIWs on ABF in Glass Interposer Technology for mmWave Applications " to be submitted in *IEEE* Transactions on Components, Packaging and Manufacturing *(under preparation)*

4. Nahid A. Amoli, **Mutee ur Rehman**, Lakshmi Narasimha Vijay Kumar, Arya Moradinia, Fuhan Liu, Madhavan Swaminathan, et.al “Ultralow-Loss Substrate-Integrated Waveguides in Alumina Ribbon Ceramic Substrates for 75 to 170 GHz Wireless Application,” submitted to IEEE Microwave and Wireless Component Letters (MWCL) (under major review)

5. **Mutee ur Rehman**, L. N. V. Kumar and M. Swaminathan, "Substrate Integrated Waveguide Filters in Glass Interposer for mmWave Applications," in *IEEE* Transactions on Components, Packaging and Manufacturing Technology*,* Oct 2022

6. N. Aslani-Amoli, **Mutee ur Rehman**, Fuhan Liu, Madhavan Swaminathan, et al., "Characterization of Alumina Ribbon Ceramic Substrates for 5G and mm-Wave Applications," in IEEE Transactions on Components, Packaging and Manufacturing Technology, vol. 12, no. 9, pp. 1432-1445, Sept. 2022,

7. **Mutee ur Rehman,** S. Ravichandran, A. O. Watanabe, S. Erdogan and M. Swaminathan, "Characterization of ABF/Glass/ABF Substrates for mmWave Applications," in IEEE Transactions on Components, Packaging and Manufacturing Technology, March 2021

8.2.2 Conference Articles

8. Mercy Daniel-Aguebor, **Mutee ur Rehman**, Serhat Erdogan, Nikita Ambasana, Saibul Mukhopadhya, Madhavan Swaminathan,et.a "Package Design and Measurements for Radar Emulator using Accelerators and Photonics," 2022 IEEE 72nd Electronic Components and Technology Conference (ECTC), San Diego, CA, USA, 2022

9. **Mutee ur Rehman**, A. Watanabe, S. Ravichandran and M. Swaminathan, "Substrate Integrated Waveguides in Glass Interposers for mm Wave Applications," 2021 IEEE MTT-S International Microwave Symposium (IMS), Atlanta, GA, USA, 2021.

10. Nahid Aslani-Amoli, **Mutee ur Rehman**, Sridhar Sivapurapu, Fuhan Liu, Madhavan Swaminathan et al., "Transmission Lines on Alumina Ribbon Ceramic Substrate Material for 30 to 170 GHz Wireless Applications," *2021 IEEE 71st Electronic Components and Technology Conference (ECTC)*, San Diego, CA, USA, 2021.

11. Sridhar Sivapurapu, Rui Chen, **Mutee ur Rehman**, et al., "Flexible and Ultra-Thin Glass Substrates for RF Applications," 2021 IEEE 71st Electronic Components and Technology Conference (ECTC), San Diego, CA, USA, 2021.

12. **Mutee-ur-Rehman** et al.," Glass Interposer Technology for 5G and beyond," (GOMACTECH 2020)

13. **Mutee ur Rehman,** S. Ravichandran, S. Erdogan and M. Swaminathan, "W-band and D-band Transmission Lines on Glass Based Substrates for Sub-THz Modules," 2020 IEEE 70th Electronic Components and Technology Conference (ECTC), Orlando, FL, USA, 2020.

14. H. Yu, H. M. Torun, **Mutee ur Rehman** and M. Swaminathan, "Design of SIW Filters in D-band Using Invertible Neural Nets," 2020 IEEE/MTT-S International Microwave Symposium (IMS), Los Angeles, CA, USA, 2020.

15. **Mutee ur Rehman**, Madhavan Swaminathan**,** "Novel Sub-THz SIW Filters in Glass Based Heterogeneous Integrated Substrates" **(Techcon2020)**

16. S. Ravichandran, Kai-Qi Huang, **Mutee ur Rehman** *et al*., "Packaging Approaches for mm Wave and Sub-THz Communication," *2019 IEEE MTT-S International Microwave Conference on Hardware and Systems for 5G and Beyond **(IMC-5G)***, 2019

8.3 Future Work

This work contributed to the development to glass interposer technology for frequencies up to 170 GHz. Continuous developments in design, fabrication and measurement procedures will be required to support mmWave modules in future as the demand for higher data rate will push the requirement wider physical bandwidths and higher carrier frequencies. Following are a few aspects in which this work can be extended in future.

1. This thesis presented all the measured results up to 170 GHz but in future, electrical characterization of the material stack-up and performance evaluation of the interconnects will be required for frequencies above 200 GHz.
2. A mmWave module requires various interconnects and passives. In this work, first demonstrations of interconnects and filters were done and then investigations were done to improve the traditional components in terms of form factor or insertion loss. Design and demonstration of other passives like couplers, power dividers in glass interposer technology can be done in future.
3. This work used Ajinomoto dry films (ABF GL102) with AGC ENA 1 glass for design and demonstration of different interconnects and passives. There work

should be extended by evaluating the feasibility and performance of other dielectric materials.

4. This work started with a use of two metal layer system supported on ABF/glass/ABF material stack-up. Later to design Blind Via Filters, a three-metal layer stack up was used and all the three metal layers were on one side of the glass so to balance the stack-up, six metal layers were fabricated (three on each side) but the designs utilized only three metal layers. As components and systems become complex, they will require more metal layers and hence the design and demonstration of RF interconnects and passives using six and eight metal layer stack-ups in glass interposer technology can be done.
5. This work developed Air Filled SIW technology using multi-layer laminate-based stack-up supported on a glass core and reported a measured insertion loss of 0.16 dB/mm in D-band. Other passive components like filters, couplers and power dividers can be designed using this low loss Air Filled SIW technology. During this work, air filled SIW filters were also simulated along with air filled SIW interconnects, but the fabrication of interconnects was prioritized as the fabrication process was new. Air Filled SIW filter design is given in figure below and this can work can be done in future.

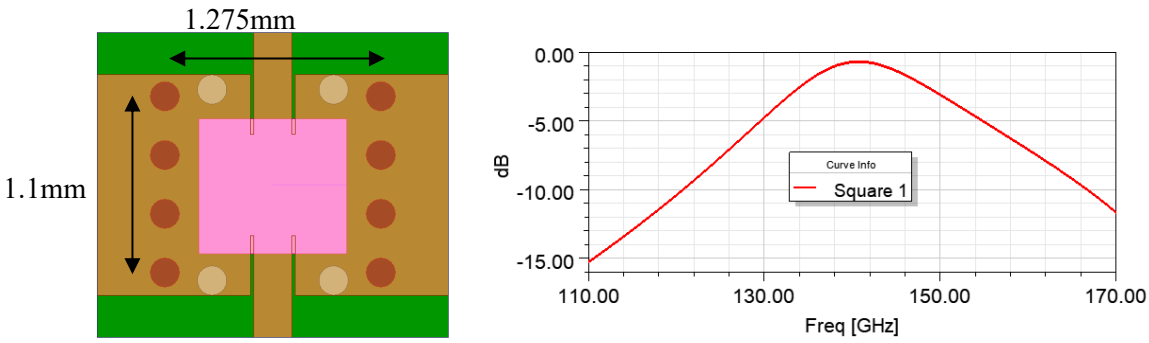
1.275mm
1.1mm
0.00
-5.00
-10.00
-15.00
dB
Curve Info
Square 1
110.00
130.00
150.00
170.00
Freq [GHz]

(a)

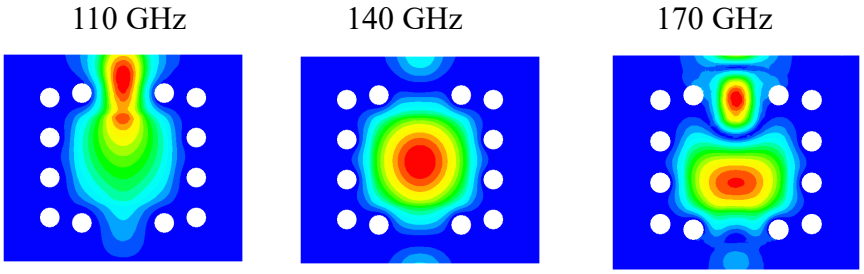
110 GHz
140 GHz
170 GHz

(b)

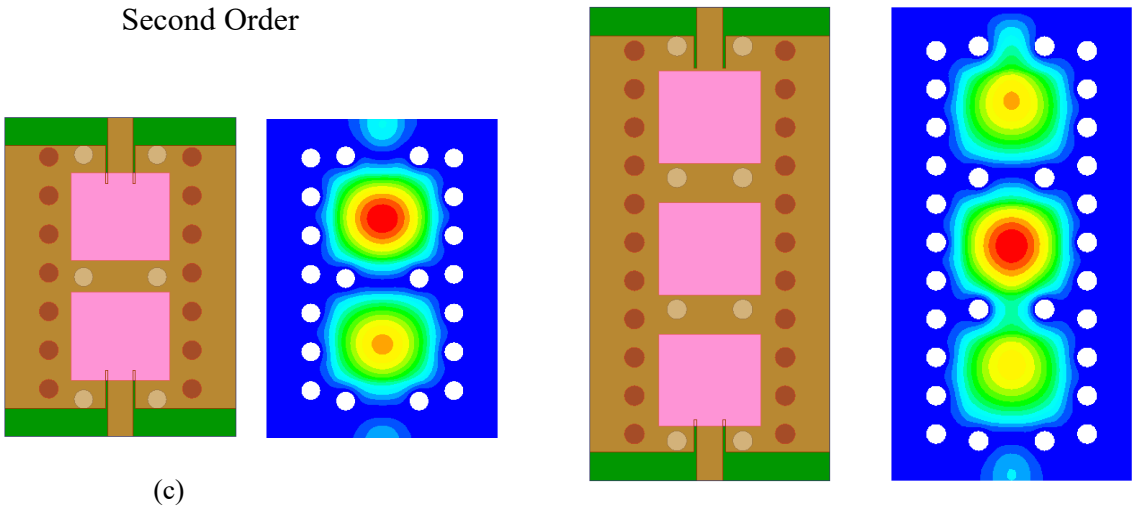
Second Order
Third Order

(c)

(d)

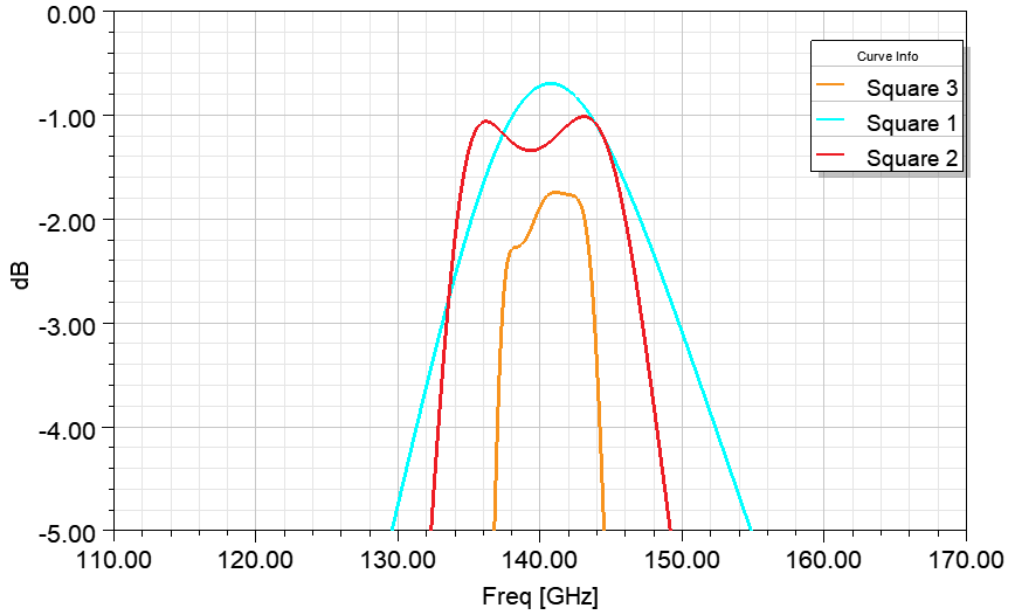

(e)

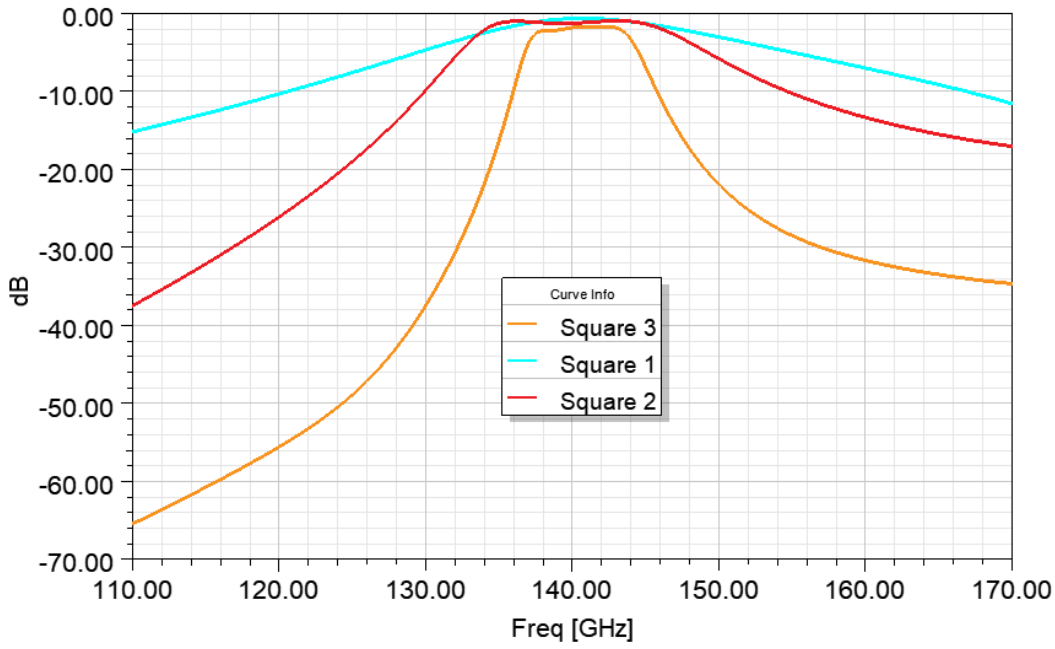

(f)

Figure 84 Air Filled SIW Filters (a) first order filter design and frequency response S21(dB) (b) electric field plots for first order filter (c) second order (d) third order (e) passband insertion loss (f) frequency response

6. Further development of Blind Via Filter Technology by doing design and demonstration of Blind Via Filters at different center frequencies for supporting mmWave modules.
7. Develop drilling techniques and tools to realize better alignment to facilitate precise control over the position and diameter of the drilled vias for accurately fabricating SIW components on a panel scale.
8. Investigate the feasibility and fabrication methods to use glass-to-glass bonding for making Air Filled SIW technology within glass interposers instead of a multi-layer laminate stack-up.
9. Perform reliability testing and investigate the changes in the electrical performance of materials and interconnects.

8.4 References

[1] T. S. Rappaport *et al.*, "Millimeter Wave Mobile Communications for 5G Cellular: It Will Work!," (in English), *Ieee Access,* vol. 1, pp. 335-349, 2013, doi: 10.1109/Access.2013.2260813.

[2] S. Chinchali *et al.*, "Network Offloading Policies for Cloud Robotics: a Learning-based Approach," (in English), *Robotics: Science and Systems Xv,* 2019. [Online]. Available: <Go to ISI>://WOS:000570976800062.

[3] M. Chen, Y. W. Tian, G. Fortino, J. Zhang, and I. Humar, "Cognitive Internet of Vehicles," (in English), *Comput Commun,* vol. 120, pp. 58-70, May 2018, doi: 10.1016/j.comcom.2018.02.006.

[4] H. Aggrawal, P. Chen, M. M. Assefzadeh, B. Jamali, and A. Babakhani, "Gone in a Picosecond," (in English), *Ieee Microw Mag,* vol. 17, no. 12, pp. 24-38, Dec 2016, doi: 10.1109/Mmm.2016.2608764.

[5] D. M. Mittleman, R. H. Jacobsen, R. Neelamani, R. G. Baraniuk, and M. C. Nuss, "Gas sensing using terahertz time-domain spectroscopy," (in English), *Appl Phys B-Lasers O,* vol. 67, no. 3, pp. 379-390, Sep 1998, doi: DOI 10.1007/s003400050520.

[6] M. Tonouchi, "Cutting-edge terahertz technology," (in English), *Nat Photonics,* vol. 1, no. 2, pp. 97-105, Feb 2007, doi: 10.1038/nphoton.2007.3.

[7] M. Aladsani, A. Alkhateeb, and G. C. Trichopoulos, "Leveraging Mmwave Imaging and Communications for Simultaneous Localization and Mapping," (in English), *Int Conf Acoust Spee,* pp. 4539-4543, 2019. [Online]. Available: <Go to ISI>://WOS:000482554004155.

[8] M. J. W. Rodwell *et al.*, "100-340GHz Systems: Transistors and Applications," (in English), *Int El Devices Meet,* 2018. [Online]. Available: <Go to ISI>://WOS:000459882300058.

[9] D. M. Mittleman, "Twenty years of terahertz imaging [Invited]," (in English), *Opt Express,* vol. 26, no. 8, pp. 9417-9431, Apr 16 2018, doi: 10.1364/Oe.26.009417.

[10] V. Petrov, D. Moltchanov, and Y. Koucheryavy, "Applicability assessment of terahertz information showers for next-generation wireless networks," (in English), *Ieee Icc,* 2016, doi: 10.1109/Icc.2016.7511129.

[11] V. Petrov, A. Pyattaev, D. Moltchanov, and Y. Koucheryavy, "Terahertz Band Communications: Applications, Research Challenges, and Standardization

Activities," (in English), *Int C Ultra Mod Tele,* pp. 183-190, 2016. [Online]. Available: <Go to ISI>://WOS:000392263300032.

[12] S. Koenig *et al.*, "Wireless sub-THz communication system with high data rate," (in English), *Nat Photonics,* vol. 7, no. 12, pp. 977-981, Dec 2013, doi: 10.1038/Nphoton.2013.275.

[13] O. Kanhere and T. S. Rappaport, "Position Locationing for Millimeter Wave Systems," (in English), *Ieee Glob Comm Conf,* 2018. [Online]. Available: <Go to ISI>://WOS:000465774305039.

[14] T. S. Rappaport *et al.*, "Wireless Communications and Applications Above 100 GHz: Opportunities and Challenges for 6G and Beyond," (in English), *Ieee Access,* vol. 7, pp. 78729-78757, 2019, doi: 10.1109/Access.2019.2921522.

[15] P. H. Siegel, "Terahertz technology," (in English), *Ieee T Microw Theory,* vol. 50, no. 3, pp. 910-928, Mar 2002, doi: Pii S0018-9480(02)01958-0

Doi 10.1109/22.989974.

[16] S. Ravichandran *et al.*, "Packaging Approaches for mmWave and Sub-THz Communication," (in English), *2019 Ieee Mtt-S International Microwave Conference on Hardware and Systems for 5g and Beyond (Imc-5g),* 2019. [Online]. Available: <Go to ISI>://WOS:000674715500025.

[17] M. Swaminathan, V. Sundaram, J. Papapolymerou, and P. M. Raj, "Polymers for RF Apps," (in English), *Ieee Microw Mag,* vol. 12, no. 7, pp. 62-77, Dec 2011, doi: 10.1109/Mmm.2011.942701.

[18] W. Y. Song, D. Y. Kim, J. H. Park, J. G. Park, and S. H. Son, "Measurement of dielectric and mechanical properties of LTCC for MMW-Band application," (in English), *Apmc: 2009 Asia Pacific Microwave Conference, Vols 1-5,* pp. 536-+, 2009. [Online]. Available: <Go to ISI>://WOS:000279924300136.

[19] H. J. Song, "Packages for Terahertz Electronics," (in English), *P Ieee,* vol. 105, no. 6, pp. 1121-1138, Jun 2017, doi: 10.1109/Jproc.2016.2633547.

[20] W. T. Khan, C. A. D. Morcillo, A. C. Ulusoy, and J. Papapolymerou, "Characterization of Liquid Crystal Polymer from 110 GHz to 170 GHz," (in English), *Ieee Radio Wireless,* pp. 157-159, 2014. [Online]. Available: <Go to ISI>://WOS:000356869200051.

[21] D. C. Thompson, O. Tantot, H. Jallageas, G. E. Ponchak, M. M. Tentzeris, and J. Papapolymerou, "Characterization of liquid crystal polymer (LCP) material and transmission lines on LCP substrates from 30 to 110 GHz," (in English), *Ieee T Microw Theory,* vol. 52, no. 4, pp. 1343-1352, Apr 2004, doi: 10.1109/Tmtt.2004.825738.

[22] W. T. Khan, A. C. Ulusoy, and J. Papapolymerou, "D- Band Characterization of Co-Planar Wave Guide and Microstrip Transmission Lines on Liquid Crystal Polymer," (in English), *2013 Ieee 63rd Electronic Components and Technology Conference (Ectc),* pp. 2304-2309, 2013. [Online]. Available: <Go to ISI>://WOS:000332764900363.

[23] W. T. Khan, A. L. V. Lopez, A. C. Ulusoy, and J. Papapolymerou, "Packaging a W -Band Integrated Module With an Optimized Flip-Chip Interconnect on an Organic Substrate," (in English), *Ieee T Microw Theory,* vol. 62, no. 1, pp. 64-72, Jan 2014, doi: 10.1109/Tmtt.2013.2292832.

[24] S. S. Li, M. Yi, S. Pavlidis, H. Yu, M. Swaminathan, and J. Papapolymerou, "Investigation of Surface Roughness Effects for D-band SIW Transmission Lines on LCP Substrate," (in English), *2017 Ieee Radio and Wireless Symposium (Rws),* pp. 121-124, 2017. [Online]. Available: <Go to ISI>://WOS:000403613800036.

[25] C. F. Tseng, C. S. Liu, C. H. Wu, and D. Yu, "InFO (Wafer Level Integrated Fan-Out) Technology," (in English), *Elec Comp C,* pp. 1-6, 2016, doi: 10.1109/Ectc.2016.65.

[26] S. Ravichandran *et al.*, "2.5D Glass Panel Embedded (GPE) Packages with Better I/O Density, Performance, Cost and Reliability than Current Silicon Interposers and High-Density Fan-Out Packages," (in English), *2018 Ieee 68th Electronic Components and Technology Conference (Ectc 2018),* pp. 625-630, 2018, doi: 10.1109/Ectc.2018.00099.

[27] V. Sukumaran, T. Bandyopadhyay, V. Sundaram, and R. Tummala, "Low-Cost Thin Glass Interposers as a Superior Alternative to Silicon and Organic Interposers for Packaging of 3-D ICs," (in English), *Ieee T Comp Pack Man,* vol. 2, no. 9, pp. 1426-1433, Sep 2012, doi: 10.1109/Tcpmt.2012.2204392.

[28] M. U. Rehman, S. Ravichandran, A. O. Watanabe, S. Erdogan, and M. Swaminathan, "Characterization of ABF/Glass/ABF Substrates for mmWave Applications," (in English), *Ieee T Comp Pack Man,* vol. 11, no. 3, pp. 384-394, Mar 2021, doi: 10.1109/Tcpmt.2021.3061485.

[29] L. S. Rocha, C. C. Junqueira, E. Gambin, A. N. Vicente, A. E. Culhaoglu, and E. Kemptner, "A Free Space Measurement Approach for Dielectric Material Characterization," (in English), *2013 Sbmo/Ieee Mtt-S International Microwave & Optoelectronics Conference (Imoc),* 2013. [Online]. Available: <Go to ISI>://WOS:000359376200070.

[30] B. G. Duixia Liu, Ullrich Pfieffer, Janusz, *Advance Mm-Wave Technologies : Antennas, Packaging and Circuits*. John Wiley and Sons Publications Limited 2009.

[31] G. Kent, "Nondestructive permittivity measurement of substrates," (in English), *Ieee T Instrum Meas,* vol. 45, no. 1, pp. 102-106, Feb 1996, doi: Doi 10.1109/19.481319.

[32] P. A. Bernard and J. M. Gautray, "Measurement of Dielectric-Constant Using a Microstrip Ring Resonator," (in English), *Ieee T Microw Theory,* vol. 39, no. 3, pp. 592-595, Mar 1991, doi: Doi 10.1109/22.75310.

[33] G. Z. Zheng, J. Papapolymerou, and M. A. Tentzeris, "Wideband coplanar waveguide RF probe pad to microstrip transitions without via holes," (in English), *Ieee Microw Wirel Co,* vol. 13, no. 12, pp. 544-546, Dec 2003, doi: 10.1109/Lmwc.2003.820638.

[34] C. C. Tien, C. K. C. Tzuang, S. T. Peng, and C. C. Chang, "Transmission Characteristics of Finite-Width Conductor-Backed Coplanar Wave-Guide," (in English), *Ieee T Microw Theory,* vol. 41, no. 9, pp. 1616-1624, Sep 1993, doi: Doi 10.1109/22.245687.

[35] R. B. Marks, "A Multiline Method of Network Analyzer Calibration," (in English), *Ieee T Microw Theory,* vol. 39, no. 7, pp. 1205-1215, Jul 1991, doi: Doi 10.1109/22.85388.

[36] "Pathwave Advanced Design System." https://www.keysight.com/us/en/products/software/pathwave-design-software/pathwave-advanced-design-system.html (accessed.

[37] "Ansys High Frequency Structure Simulation " https://www.ansys.com/products/electronics/ansys-hfss (accessed.

[38] I. Wolff and N. Knoppik, "Microstrip Ring Resonator and Dispersion Measurement on Microstrip Lines," (in English), *Electron Lett,* vol. 7, no. 26, pp. 779-&, 1971, doi: DOI 10.1049/el:19710532.

[39] H. Akahoshi *et al.*, "Fine Line Circuit Manufacturing Technology with Electroless Copper Plating," (in English), *Ieee T Compon Pack A,* vol. 18, no. 1, pp. 127-135, Mar 1995, doi: Doi 10.1109/95.370746.

[40] I. J. Bahl and R. Garg, "Simple and Accurate Formulas for a Microstrip with Finite Strip Thickness," (in English), *P Ieee,* vol. 65, no. 11, pp. 1611-1612, 1977, doi: Doi 10.1109/Proc.1977.10783.

[41] M. Kirschning and R. H. Jansen, "Accurate Model for Effective Dielectric-Constant of Microstrip with Validity up to Millimetre-Wave Frequencies," (in English), *Electron Lett,* vol. 18, no. 6, pp. 272-273, 1982, doi: DOI 10.1049/el:19820186.

[42] S. Takahashi, Y. Sato, K. Horiuchi, and M. Ono, "Development of High Frequency Device using Glass or Fused Silica with 3D Integration," (in English), *2017 Ieee*

67th Electronic Components and Technology Conference (Ectc 2017), pp. 758-763, 2017, doi: 10.1109/Ectc.2017.124.

[43] M. V. Schneider, "Microstrip Lines for Microwave Integrated Circuits," (in English), *Bell Syst Tech J,* vol. 48, no. 5, pp. 1421-+, 1969, doi: DOI 10.1002/j.1538-7305.1969.tb04274.x.

[44] D. Thompson, P. Kirby, J. Papapolymerou, and M. M. Tentzeris, "W-band characterization of finite ground coplanar transmission lines on liquid crystal polymer (LCP) substrates," (in English), *53rd Electronic Components & Technology Conference, 2003 Proceedings,* pp. 1652-1655, 2003, doi: Doi 10.1109/Ectc.2003.1216522.

[45] F. Fesharaki, T. Djerafi, M. Chaker, and K. Wu, "Guided-Wave Properties of Mode-Selective Transmission Line," (in English), *Ieee Access,* vol. 6, pp. 5379-5392, 2018, doi: 10.1109/Access.2017.2697867.

[46] Y. C. Xing and T. S. Rappaport, "Propagation Measurement System and Approach at 140 GHz-Moving to 6G and Above 100 GHz," (in English), *Ieee Glob Comm Conf,* 2018. [Online]. Available: <Go to ISI>://WOS:000465774304137.

[47] D. Deslandes and K. Wu, "Integrated microstrip and rectangular waveguide in planar form," (in English), *Ieee Microw Wirel Co,* vol. 11, no. 2, pp. 68-70, Feb 2001, doi: Doi 10.1109/7260.914305.

[48] D. Deslandes and K. Wu, "Accurate modeling, wave mechanisms, and design considerations of a substrate integrated waveguide," (in English), *Ieee T Microw Theory,* vol. 54, no. 6, pp. 2516-2526, Jun 2006, doi: 10.1109/Tmtt.2006.875807.

[49] Y. J. Cheng, K. Wu, and W. Hong, "Power Handling Capability of Substrate Integrated Waveguide Interconnects and Related Transmission Line Systems," (in English), *Ieee T Adv Packaging,* vol. 31, no. 4, pp. 900-909, Nov 2008, doi: 10.1109/Tadvp.2008.927814.

[50] M. Bertrand *et al.*, "Substrate Integrated Waveguides for mm-wave Functionalized Silicon Interposer," (in English), *Ieee Mtt S Int Micr,* pp. 875-878, 2018. [Online]. Available: <Go to ISI>://WOS:000451173600233.

[51] M. J. Asadi *et al.*, "SiC Substrate-Integrated Waveguides for High-Power Monolithic Integrated Circuits Above 110 GHz," (in English), *2021 Ieee Mtt-S International Microwave Symposium (Ims),* pp. 669-672, 2021, doi: 10.1109/Ims19712.2021.9574845.

[52] M. U. Rehman, A. Watanabe, S. Ravichandran, and M. Swaminathan, "Substrate Integrated Waveguides in Glass Interposers for mmWave Applications," (in English), *2021 Ieee Mtt-S International Microwave Symposium (Ims),* pp. 339-341, 2021, doi: 10.1109/Ims19712.2021.9574832.

[53] X. P. Chen and K. Wu, "Substrate Integrated Waveguide Filters," (in English), *Ieee Microw Mag,* vol. 15, no. 7, pp. 75-83, Nov-Dec 2014, doi: 10.1109/Mmm.2014.2355751.

[54] X. P. Chen and K. Wu, "Substrate Integrated Waveguide Filters," (in English), *Ieee Microw Mag,* vol. 15, no. 6, pp. 121-133, Sep-Oct 2014, doi: 10.1109/Mmm.2014.2332886.

[55] X. P. Chen and K. Wu, "Substrate Integrated Waveguide Filter," (in English), *Ieee Microw Mag,* vol. 15, no. 5, pp. 108-116, Jul-Aug 2014, doi: 10.1109/Mmm.2014.2321263.

[56] M. U. Rehman, L. N. V. Kumar, and M. Swaminathan, "Substrate Integrated Waveguide Filters in Glass Interposer for mmWave Applications," (in English), *Ieee T Comp Pack Man,* vol. 12, no. 10, pp. 1719-1722, Oct 2022, doi: 10.1109/Tcpmt.2022.3210375.

[57] Y. Cassivi, L. Perregrini, P. Arcioni, M. Bressan, K. Wu, and G. Conciauro, "Dispersion characteristics of substrate integrated rectangular waveguide," (in English), *Ieee Microw Wirel Co,* vol. 12, no. 9, pp. 333-335, Sep 2002, doi: 10.1109/Lmwc.2002.803188.

[58] Y. F. Zhang, S. Y. Shi, R. D. Martin, and D. W. Prather, "Substrate integrated waveguide filter on LCP substrate at 94 GHz," (in English), *Microw Opt Techn Let,* vol. 58, no. 3, pp. 577-580, Mar 2016, doi: 10.1002/mop.29621.

[59] G. Prigent, A. L. Franc, M. Wietstruck, and M. Keynak, "Substrate Integrated Waveguide Bandpass Filters implemented on Silicon Interposer for Terahertz Applications," (in English), *Proceedings of the 2020 Ieee/Mtt-S International Microwave Symposium (Ims),* pp. 595-598, 2020. [Online]. Available: <Go to ISI>://WOS:000627746500489.

[60] S. W. Wong, K. Wang, Z. N. Chen, and Q. X. Chu, "Design of Millimeter-Wave Bandpass Filter Using Electric Coupling of Substrate Integrated Waveguide (SIW)," (in English), *Ieee Microw Wirel Co,* vol. 24, no. 1, pp. 26-28, Jan 2014, doi: 10.1109/Lmwc.2013.2288177.

[61] D. Stephens, P. R. Young, and I. D. Robertson, "Millimeter-wave substrate integrated waveguides and filters in photoimageable thick-film technology," (in English), *Ieee T Microw Theory,* vol. 53, no. 12, pp. 3832-3838, Dec 2005, doi: 10.1109/Tmtt.2005.859862.

[62] X. X. Liu, Z. M. Zhu, Y. Liu, Q. J. Lu, X. K. Yin, and Y. T. Yang, "Wideband Substrate Integrated Waveguide Bandpass Filter Based on 3-D ICs," (in English), *Ieee T Comp Pack Man,* vol. 9, no. 4, pp. 728-735, Apr 2019, doi: 10.1109/Tcpmt.2018.2878863.

[63] W. Hong *et al.*, "Half mode substrate integrated waveguide: A new guided wave structure for microwave and millimeter wave application," (in English), *Conference Digest of the 2006 Joint 31st International Conference on Infrared and Millimeter Waves and 14th International Conference on Terahertz Electronics,* pp. 219-219, 2006. [Online]. Available: <Go to ISI>://WOS:000246942200217.

[64] C. Jin, R. Li, A. Alphones, and X. Y. Bao, "Quarter-Mode Substrate Integrated Waveguide and Its Application to Antennas Design," (in English), *Ieee T Antenn Propag,* vol. 61, no. 6, pp. 2921-2928, Jun 2013, doi: 10.1109/Tap.2013.2250238.

[65] H. Hasegawa, M. Furukawa, and H. Yanai, "Properties of Microstrip Line on Si-Sio2 System," (in English), *Ieee T Microw Theory,* vol. Mt19, no. 11, pp. 869-+, 1971, doi: Doi 10.1109/Tmtt.1971.1127658.

[66] T. Masuda, N. Shiramizu, T. Nakamura, and K. Washlo, "Characterization and modeling of microstrip transmission lines with slow-wave effect," (in English), *2008 Ieee Topical Meeting on Silicon Monolithic Integrated Circuits in Rf Systems, Digest of Papers,* pp. 155-158, 2008. [Online]. Available: <Go to ISI>://WOS:000253709400039.

[67] T. S. D. Cheung *et al.*, "On-chip interconnect for mm-wave applications using an all-copper technolgy and wavelength reduction," (in English), *Isscc Dig Tech Pap I,* vol. 46, pp. 396-+, 2003. [Online]. Available: <Go to ISI>://WOS:000185583300169.

[68] A. L. Franc, E. Pistono, G. Meunier, D. Gloria, and P. Ferrari, "A Lossy Circuit Model Based on Physical Interpretation for Integrated Shielded Slow-Wave CMOS Coplanar Waveguide Structures," (in English), *Ieee T Microw Theory,* vol. 61, no. 2, pp. 754-763, Feb 2013, doi: 10.1109/Tmtt.2012.2231430.

[69] A. Niembro-Martin *et al.*, "Slow-Wave Substrate Integrated Waveguide," (in English), *Ieee T Microw Theory,* vol. 62, no. 8, pp. 1625-1633, Aug 2014, doi: 10.1109/Tmtt.2014.2328974.

[70] M. Bertrand, Z. H. Liu, E. Pistono, D. Kaddour, and P. Ferrari, "A Compact Slow-Wave Substrate Integrated Waveguide Cavity Filter," (in English), *2015 Ieee Mtt-S International Microwave Symposium (Ims),* 2015. [Online]. Available: <Go to ISI>://WOS:000370722900097.

[71] N. Marcuvitz, *Waveguide Handbook*. New York , NY, USA: McGraw-Hill, 1951.

[72] Y. Leviatan, P. G. Li, A. T. Adams, and J. Perini, "Single-Post Inductive Obstacle in Rectangular Waveguide," (in English), *Ieee T Microw Theory,* vol. 31, no. 10, pp. 806-812, 1983, doi: Doi 10.1109/Tmtt.1983.1131610.

[73] Y. Leviatan, P. G. Li, A. T. Adams, and J. Perini, "Comment on Single-Post Inductive Obstacle in Rectangular Wave-Guide - Reply," (in English), *Ieee T*

Microw Theory, vol. 33, no. 6, pp. 556-556, 1985, doi: Doi 10.1109/Tmtt.1985.1133120.

[74] C. Carceller, P. Soto, V. Boria, and M. Guglielmi, "Capacitive Obstacle Realizing Multiple Transmission Zeros for In-Line Rectangular Waveguide Filters," (in English), *Ieee Microw Wirel Co,* vol. 26, no. 10, pp. 795-797, Oct 2016, doi: 10.1109/Lmwc.2016.2605462.

[75] M. Nosrati and M. Daneshmand, "Substrate Integrated Waveguide L-Shaped Iris for Realization of Transmission Zero and Evanescent-Mode Pole," (in English), *Ieee T Microw Theory,* vol. 65, no. 7, pp. 2310-2320, Jul 2017, doi: 10.1109/Tmtt.2017.2679011.

[76] Y. Zhang *et al.*, "Slow Wave Substrate-Integrated Waveguide With Miniaturized Dimensions and Broadened Bandwidth," (in English), *Ieee T Microw Theory,* vol. 69, no. 8, pp. 3675-3683, Aug 2021, doi: 10.1109/Tmtt.2021.3074170.

[77] I. Savidis and E. G. Friedman, "Closed-Form Expressions of 3-D Via Resistance, Inductance, and Capacitance," (in English), *Ieee T Electron Dev,* vol. 56, no. 9, pp. 1873-1881, Sep 2009, doi: 10.1109/Ted.2009.2026200.

[78] M. Yi *et al.*, "Surface Roughness Modeling of Substrate Integrated Waveguide in D-Band," (in English), *Ieee T Microw Theory,* vol. 64, no. 4, pp. 1209-1216, Apr 2016, doi: 10.1109/Tmtt.2016.2535290.

[79] F. Parment, A. Ghiotto, T. P. Vuong, J. M. Duchamp, and K. Wu, "Air-Filled Substrate Integrated Waveguide for Low-Loss and High Power-Handling Millimeter-Wave Substrate Integrated Circuits," (in English), *Ieee T Microw Theory,* vol. 63, no. 4, pp. 1228-1238, Apr 2015, doi: 10.1109/Tmtt.2015.2408593.

[80] F. Parment, A. Ghiotto, T. P. Vuong, J. M. Duchamp, and K. Wu, "Air-Filled SIW Transmission Line and Phase Shifter For High-Performance and Low-Cost U-Band Integrated Circuits and Systems," (in English), *Glob Sym Millim Wave,* 2015. [Online]. Available: <Go to ISI>://WOS:000380569600019.

[81] F. Parment, A. Ghiotto, T. P. Vuong, J. M. Duchamp, and K. Wu, "Low-Loss Air-Filled Substrate Integrated Waveguide (SIW) Band-Pass Filter with Inductive Posts," (in English), *Eur Microw Conf,* pp. 761-764, 2015. [Online]. Available: <Go to ISI>://WOS:000377204600188.

[82] F. Parment, A. Ghiotto, T. P. Vuong, J. M. Duchamp, and K. Wu, "Air-to-Dielectric-Filled Two-Hole Substrate-Integrated Waveguide Directional Coupler," (in English), *Ieee Microw Wirel Co,* vol. 27, no. 7, pp. 621-623, Jul 2017, doi: 10.1109/Lmwc.2017.2711525.

[83] "Isola Astra MT77." https://www.isola-group.com/pcb-laminates-prepreg/astra-mt77-laminate-and-prepreg/ (accessed Jan 2023.

[84] N. Ghassemi, I. Boudreau, D. Deslandes, and K. Wu, "Millimeter-Wave Broadband Transition of Substrate Integrated Waveguide on High-to-Low Dielectric Constant Substrates," (in English), *Ieee T Comp Pack Man,* vol. 3, no. 10, pp. 1764-1770, Oct 2013, doi: 10.1109/Tcpmt.2013.2257929.

[85] Robab Kazemi , A. E. Fathy, S. Y. and, and R. A. Sadeghzadeh, "Development of an ultra wide band GCPW to SIW transition," presented at the IEEE Radio and Wireless Symposium, 2012.

[86] M. Elkhouly et al . "Fully Integrated 2D Scalable TX/RX Chipset for D-Band Phased-Array-on-Glass Modules," presented at the IEEE International Solid- State Circuits Conference (ISSCC), 2022.

APPENDIX A

TOOLS USED

The tools used for fabricating the designed test vehicles are enlisted below.

1. Meiki Vacuum Laminator – used for laminating dry film polymers and photoresist
2. Oxygen Plasma – for surface activation of bare glass panels and polymer surface before further processing
3. Nitrogen Oven – used for curing and annealing at different process stages
4. Silane Bath – for adhesion promotion on bare glass panels
5. Electroless Copper Deposition Line – used for depositing copper seed layer
6. Sputterer – used for depositing copper seed layer
7. Tamarac Mask Aligner – used for photolithography
8. Ushio Mask Aligner – used for photolithography
9. Heidelberg Maskless Aligner – used for photolithography
10. Photoresist Developer – used for developing photoresist after exposure
11. Electrolytic Plating Tank – used for plating copper
12. Differential Etcher – used for removing copper seed layer
13. NovaBond Process – used for promoting adhesion of copper with polymer
14. Cornerstone Laser – used for drilling via
15. Optec Femtosecond Laser – used for drilling vias and cavities
16. Keyence Optical Profiler – used for measuring fabricated dimensions and surface roughness
17. Zeta Optical Profiler – used for measuring fabricated dimensions

18. Tencor profilometer – used for measuring surface roughness

The tools used for measuring scattering parameters are enlisted below

19. Anritsu VNA (ME7808) – VNA used for 20 GHz to 110 GHz
20. Frequency extenders 3742A-EW – used with Anritsu VNA
21. Cascade ACP-110-GSG-200 - probes used for 20 GHz to 110 GHz
22. Cascade 101-190C – calibration substrate used for 20 GHz to 110 GHz
23. Keysight E8361C vector network analyzer – used for 110 GHz to 170 GHz
24. Frequency extenders V06VNA2 – used for 110 GHz to 170 GHz
25. Cascade infinity probes 170-S-GSG-75-BT- used for 110 GHz to 170 GHz
26. Cascade 138-356 – calibration substrate used for 110 GHz to 170 GHz